Quality Control and Wind Retrieval for SeaWinds

by

M. Portabella and A. Stoffelen

Final report of the EUMETSAT QuikSCAT fellowship

KNMI

Contents

Preface

This report contains a description of the EUMETSAT QuikSCAT fellowship work, which was carried out at the Royal Netherlands Meteorological Institute (KNMI) in De Bilt (The Netherlands), within the research group of the Research & Development Observations Division of the Observations and Modeling Department. The project started in February 1999 and had a duration of 3 years.

The main goals of the fellowship were to perform a Quality Control (QC) procedure, using the experience gained on previous scatterometer missions such as ERS and NSCAT, and to potentially contribute to improve wind retrieval in the regions of the QuikSCAT swath where the inversion skill decreases.

The American Ku-band scatterometer missions present a bridge to cover the gap between past and future European missions. On the one hand, ERS-2 scatterometer data stream was interrupted on January 2001 due to an attitude problem of the satellite and it is not clear yet whether the data stream will be reactivated or not. On the other hand, the next European scatterometer on board METOP satellite will be launched not before the end of 2005. Therefore, since 1999, EUMETSAT and KNMI are investing, through the NSCAT and QuikSCAT fellowships and more recently through the NWP-SAF, in gaining knowledge on Ku-band scatterometry. Important progress has been made in the interpretation and use of the data. KNMI has set up a preliminary processing stream, visible through a web interface (http://www.knmi.nl/scatterometer) and used for nowcasting purposes at several national meteorological services. Also, through a collaboration with ECMWF, the QuikSCAT data are used for operational assimilation purposes at ECMWF.

In view of the next American scatterometer mission, SeaWinds on ADEOS-2, more Research & Development activities are planned in the framework of the NWP-SAF. By doing so, the European involvement in spaceborne scatterometry and its applications is ensured for the benefit of the European meteorological community.

1   Introduction

The SeaWinds on QuikSCAT mission (from NASA) is a "quick recovery" mission to fill the gap created by the loss of data from the NASA Scatterometer (NSCAT), when the ADEOS-1 satellite lost power in June 1997. QuikSCAT was launched from Vandenberg Air Force Base (USA) in June 19, 1999. A similar version of the SeaWinds instrument will fly on the Japanese ADEOS-II satellite currently scheduled for launch in late 2002.

Instrument characteristics

The SeaWinds instrument is an active microwave radar designed to measure the electromagnetic backscatter from the wind roughened ocean surface. The instrument is a conically scanning pencil-beam scatterometer, which in comparison with the NSCAT fan-beam scatterometer has the following advantages: higher signal-to-noise ratio, smaller in size, and superior coverage. On the other hand, the new measurement geometry provides a variable mix of polarizations and azimuth looks that require renewed data characterisation efforts as employed in this fellowship.

The SeaWinds instrument uses a rotating 1-meter dish antenna with two spot beams, an H-pol beam and a V-pol beam at incidence angles of 46º and 54º respectively, that sweep in a circular pattern. The antenna radiates microwave pulses at a frequency of 13.4 GHz (Ku-Band) across a 1800-km-wide swath centered on the spacecraft's nadir subtrack, making approximately 1.1 million 25-km ocean surface wind vector measurements and covering 90% of the Earth's surface every day. These measurements will help to determine atmospheric forcing, ocean response and air-sea interaction mechanisms on various spatial and temporal scales.

The SeaWinds swath is divided into 76 equidistant across-track wind vector cells (WVC) numbered from left to right when looking along the satellite's propagation direction. The nominal WVC size is 25 km x 25 km, and all backscatter measurements centered in a WVC are used to derive the WVC wind solutions. Due to the conical scanning, a WVC is generally viewed when looking forward (fore) and a second time when looking aft. As such, up to four measurement classes (called "beam" here) emerge: H-pol fore, H-pol aft, V-pol fore, and V-pol aft, in each WVC. Due to the smaller swath (1400 km) viewed in H-pol at 46º degrees incidence, the outer swath WVCs have only V-pol fore and aft backscatter measurements. For more detailed information on the QuikSCAT instrument and data we refer to [*Spencer et al.* (1994), *JPL* (2001), *Leidner et al.* (2000)].

Instrument geometry

In contrast with NSCAT, QuikSCAT has an antenna geometry, which is dependent on WVC number or cross-track location due to its circular scans on the ocean. The skill of the wind retrieval algorithm depends very much on the number of measurements and their polarization and azimuth diversity, where "azimuth diversity" is defined as the spread of the azimuth looks among the measurements in the WVC. As we see in Figure 1, the QuikSCAT swath is subdivided in several regions, assigned to three different categories. The nadir region (category II) has fore and aft looks of both beams (H-pol and V-pol) nearly 180º apart (see beam azimuth separation of the area close to WVC numbers 38-39 in Figure 3a). At the outer regions (category III) there is no inner beam information. Moreover, at the edges of the swath, the outer V-pol beam fore and aft looks are nearly in the same direction (see azimuth beam separation of the areas close to WVC numbers 1 and 76 in Figure 3a). In both swath areas (II and III), the skill of the wind retrieval algorithm is expected to decrease with respect to the rest of the swath, the so-called sweet regions (category I), where there are four measurements (fore-inner, fore-outer, aft-inner and aft-outer) with enough azimuth diversity. The initially used WVC distribution over these three categories is the
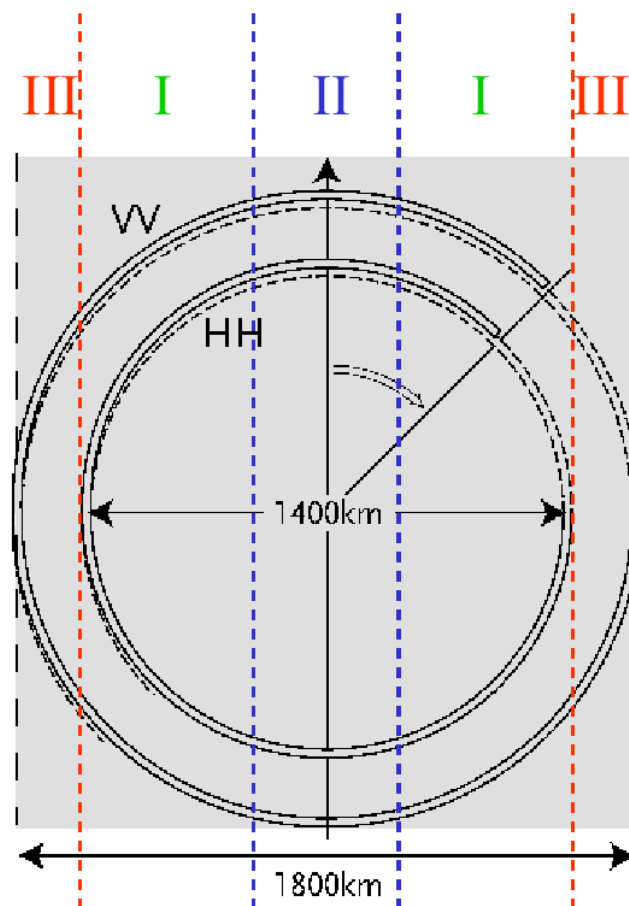

Figure 1 Schematic illustration of the QuikSCAT swath. The circles represent the two scanning rotating antennae with H-pol (HH) and V-pol (VV), and 54° and 46° incidence angles respectively. Areas I, II and III represent parts of the swath with different wind retrieval skill. Adopted from Stoffelen (1998).

following: WVC numbers 1-11 and 66-76 correspond to the outer swath, WVC numbers 12-28 and 49-65 to the sweet swath and WVC numbers 29-48 to the nadir swath.

Wind retrieval

The wind retrieval procedure on scatterometry is schematically illustrated in Figure 2. A set of radar backscatter measurements (observations) at each observation point (WVC) is inverted into a set of ambiguous wind solutions. The output form inversion is then used together with some additional information (typically from NWP models) to select one of the ambiguous wind solutions as the observed wind for every WVC. This is called ambiguity removal (AR), and in contrast with the inversion, which is performed in a WVC-by-WVC basis, the AR procedure is performed over many neighbouring WVCs at once.
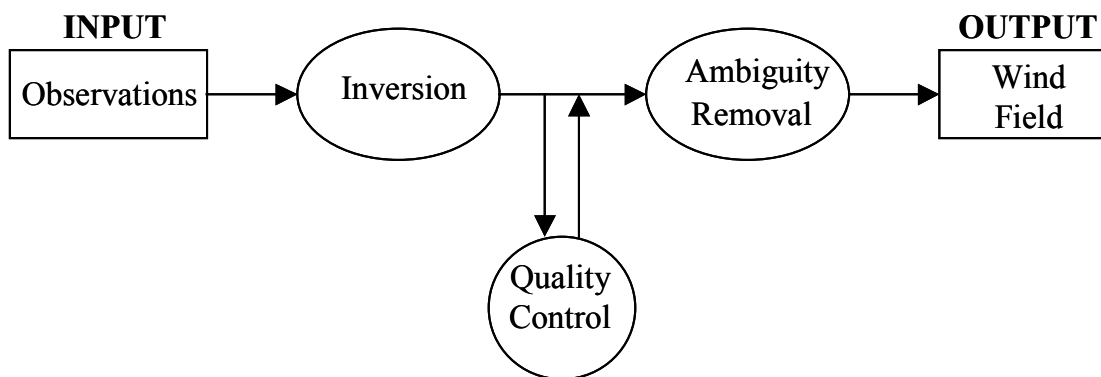
Figure 2 Schematic illustration of the scatterometer wind retrieval process

An important aspect of wind retrieval is the quality control (QC). The output from inversion can be used for QC purposes prior to AR. The goal of the QC is to detect and reject low quality WVCs. Several geophysical phenomena other than wind such as for example rain, confused sea state or ice, can "contaminate" the scatterometer observations and in turn decrease the quality of the retrieved winds. In particular, the QuikSCAT Ku-band beams are significantly sensitive to rain. It is therefore very important to include a consistent QC procedure in the QuikSCAT wind retrieval process.

In this report we describe our work on QuikSCAT product validation in chapter 2. An extensive check on data consistency is performed to both HDF and BUFR data products.

In chapter 3 a new procedure to QC SeaWinds data in HDF and BUFR formats is set, in particular to screen out rain-contaminated points. Our QC method is based on the Maximum Likelihood Estimator (MLE). The methodology was already used to screen ERS (*Stoffelen and Anderson,* 1997) and NSCAT backscatter measurements (*Figa and Stoffelen*, 2000). It checks whether the consistency of the backscatter

measurements at a particular WVC is compatible with the consistency as predicted by the Geophysical Model Function (GMF). Incompatible measurement sets are assumed to be anomalous and result in invalid wind retrieval. To validate the QC and rain screening procedure, we collocated QuikSCAT data with ECMWF winds and with a SSM/I rain product. We seeked for a statistical scheme resulting in a proper rejection threshold and verified the settings of the scheme in many cases of which we show a few here. Although HDF QC skill is very similar to BUFR QC skill, a comparison reveals very little correlation, between between BUFR an HDF MLE distributions. A comprehensive characterization of the MLE is performed in order to understand this difference. It turns out that the different level of measurement averaging between both formats (BUFR is an averaged version of HDF) is the main cause for the poor correlation. However, the QC properties remain the same. Moreover, the quality of the retrieved winds is comparable in both products. Finally, a comparison of our (KNMI) QC with a rain flag developed by JPL is performed in order to improve QC for QuikSCAT. The KNMI QC is more efficient as a QC procedure than the JPL rain flag. The JPL rain flag is very efficient in rejecting rain. However, it is also rejecting a significant amount of consistent winds in dynamically active areas. The use of the KNMI QC is therefore recommended. In the nadir region of the swath, where KNMI QC is less efficient in detecting rain, the combined use of both procedures is recommended.

In chapter 4, the QuikSCAT inversion problem is extensively examined. It turns out that the areas of the swath with poor azimuth diversity, such as the nadir region, result in low accuracy retrieved winds. We test different GMFs, smoothing techniques and interpolation schemes, in order to get the least ambiguous and most accurate winds from the inversion. The MLE is transformed into probability for ambiguity removal purposes. A comparison in terms of probability of two different QuikSCAT wind resolutions, 25-km and 100-km, shows that the lower resolution product is less ambiguous and more accurate, and therefore more suitable for wind retrieval. Finally, we propose a multiple solution scheme, which provides all the cost function solutions with their corresponding probability to a variational analysis ambiguity removal procedure, as a way to improve wind retrieval in the conflictive areas of the QuikSCAT swath.

Finally, the summary and recommendations can be found in chapter 5.

2 Product Validation

During the pre-launch period, a full validation of the different simulated QuikSCAT sample data products was performed. In particular, the work focused on the Level 2A and 2B HDF (Hierarchical Data Format) Science product and on the near-real time BUFR (Binary Universal Format Representation) product. The Level 2A contains the radar backscatter or sigma0 (σ^o) related information and the level 2B the surface wind related information, while the BUFR product is containing both σ^o and wind information.

The main difference between the HDF and the BUFR product is related to the spatial resolution of σ^o. In each WVC, the σ^o of a particular beam (fore-inner, fore-outer, aft-inner, aft-outer) in the BUFR product is an average of all σ^os of that particular beam in the HDF product which fall in the same WVC.

The SeaWinds σ^os can be either "eggs" or slices. In a particular WVC, an "egg" σ^o is the radar backscatter from the whole pulse or footprint whose centre falls in that WVC. The "egg" can be subdivided in individual range-resolution elements or slices; the slices of a particular "egg" whose centre fall in the same WVC are weight-averaged (the weighting factor is directly dependent on the noise of each slice "measurement") to become a composite σ^o. The antenna footprint or "egg" is an ellipse approximately 25-km in azimuth by 37-km in the look (or range) direction. The slices are 25-km in azimuth by a variable range resolution of approximately 2 to 10 km (the nominal width is 6 km).

The HDF real data are given (up to now) in "egg" resolution. Therefore, although the size of the WVC is 25 km, the actual resolution of the winds retrieved from the "egg" σ^os is approximately 40 km. Composites enhance the wind resolution mainly in range direction down to 25 km, and have little effect on azimuth resolution.

Real BUFR data were released to the Science Working Team (SWT) on March 2000, approximately 7 months later than the HDF real data. The BUFR real σ^os are finally weighted average of composites.

During the pre-launch period, two different versions of sample data were released by JPL and NOAA in HDF and BUFR format respectively. The "old" version was containing "egg" σ^o and the "new" one was based on slice σ^o. The most significant results of the QuikSCAT product validation on these sample files are explained in the following sections.

2.1 Azimuth averaging

In order to check inconsistencies in the way the azimuth information is computed across the swath for any beam, we look at the relative azimuth distribution for all node numbers (or WVC numbers). Figure 3 shows the mean azimuth separation between fore and aft beams by node for a few revolutions of HDF data (plot a) and the Standard Deviation (SD) of the azimuth separation for each node (plot b). The plots show a very consistent azimuth separation distribution going from small separation at the edges of both swaths, i.e., the outer (nodes 1-2 and 75-76) and the inner swath (nodes 9-10 and 67-68), and increasing gradually to a separation of almost 180º at nadir (nodes 38 and 39). The SD plot also shows consistent results with small values all across the swath, except at the edges of both the inner and the outer swaths, where the SD increases as the number of measured σ^os significantly decreases. (These nodes are set to accommodate occasional measurements that lie outside of the pre-defined 1800-km swath for the outer beam and 1400-km swath for the inner beam).

If we look at the same SD plot (Figure 4) but for BUFR (the mean azimuth separation plot is not shown because it is very similar to Figure 3a), we see a large peak around node 46 for the inner swath and node 48 for the outer swath. This peak, which does not appear in the HDF product, clearly shows some problem in the way the σ^o azimuths are averaged from HDF to BUFR. After taking a closer look to the azimuths at those particular nodes, we discovered that there was an error while averaging the azimuths close to 0º. In those particular areas, the azimuths can be either close to 360º or close to 0º. The software was not taking into account this periodicity and just averaged azimuths, leading to averaged azimuth values very different from 360º or 0º, the problem depending on the ratio of the number of azimuth values close to 360º and the number of azimuths close to 0º.

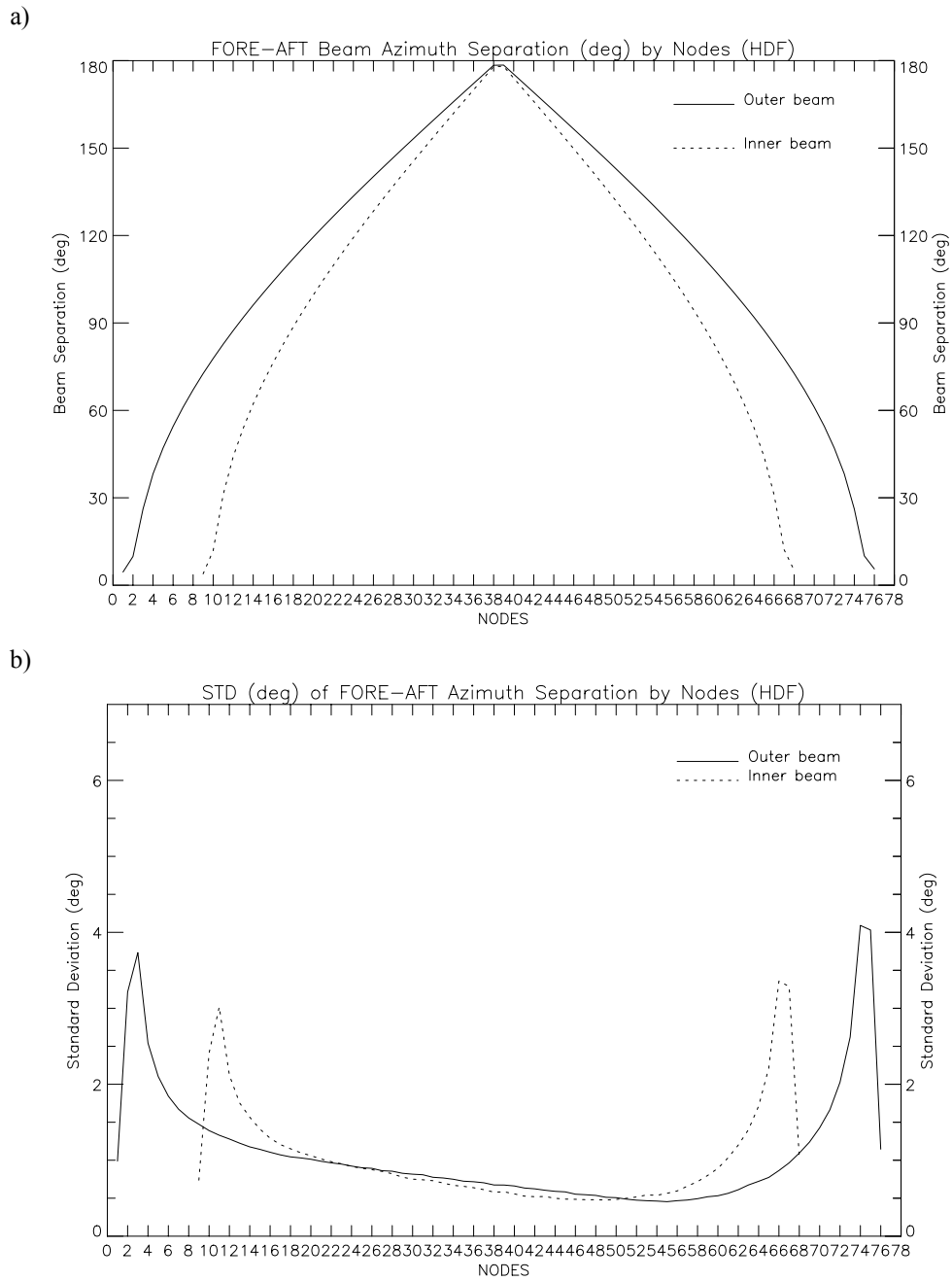The problem was reported to JPL and corrected straightaway.

a)

b)

Figure 3 a) Mean fore-aft azimuth separation by node for one revolution of HDF data; the outer beam separation is in solid line and the inner beam separation in dotted line; b) Standard Deviation of the azimuth separation.
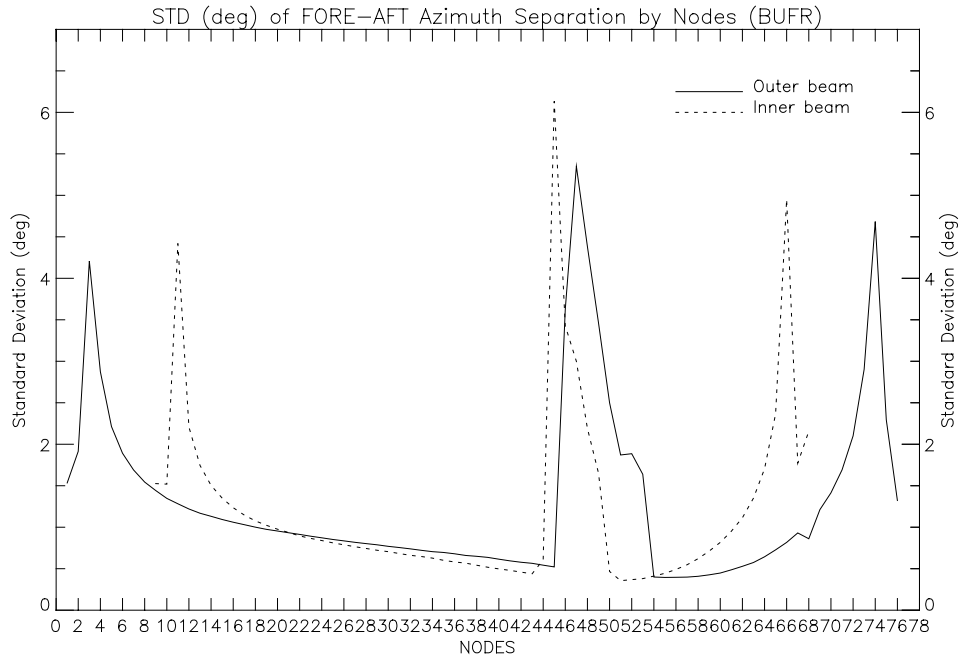
Figure 4 same as Figure 3b but for BUFR data

2.2   Wind Direction Convention

The σ^o sample data were generated applying the NSCAT-2 model function to NWP winds (from NCEP 1° spatial resolution and 12-hour forecast, which are included in the product), including additional realistic measurement noise (*Kp*) generated by a random selection from a noise distribution with width $\sqrt{Kp}$. Then, these simulated measurements of σ^o (σ^o_m) were inverted (using JPL's objective function as described in *JPL, 2001*) into winds. In order to check for any inconsistency in the simulation process we simulate σ^o (σ^o_{sim}) from the JPL retrieved winds, applying the NSCAT-2 model function. Figure 5 shows the mean σ^o_m and the mean σ^o_{sim} by node for the fore-inner beam (the results for the other beams are very similar) in one orbit (or revolution) of data. The results are very consistent although there is a systematic bias in the σ^o_{sim}. The reason is that the σ^o_m were corrected for atmospheric attenuation prior to retrieving the JPL winds, while the σ^o_{sim} were computed without "uncorrecting" for atmospheric attenuation. Therefore, σ^o_{sim} is systematically higher than σ^o_m.

Figure 6a is showing the same plot as Figure 5 but for the new version of sample data. The results are very different compared to the old version of sample data, showing no systematic bias at all. Figure 6b shows the same as Figure 6a but changing the JPL wind direction by 180° prior to compute the σ^o_{sim}. The systematic bias of σ^o_{sim} is now clearly discernible again, suggesting that JPL did change the wind direction

conventions in the product but forgot to report it in the User's Guide. This problem was confirmed by JPL and is corrected already.
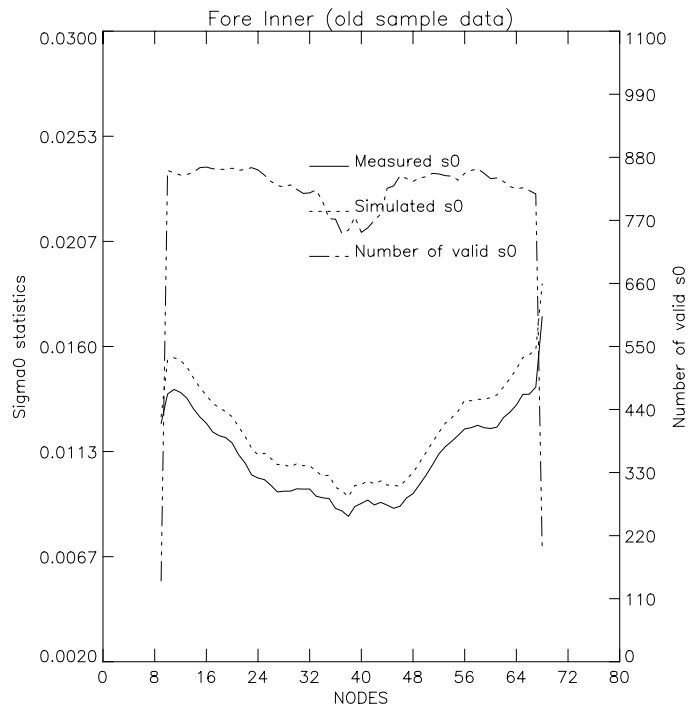
Figure 5 Mean σ°_{m} (solid) and σ°_{sim} (dotted) versus node number for the old sample data. The number of σ° used is in dash-dotted line.

The final wind direction conventions for both products is the following:

- HDF: both NWP and retrieved winds are in oceanographic or flow vector convention (0° meaning wind blowing towards North with positive angles increasing in the clockwise direction).

- BUFR: both NWP and retrieved winds are in meteorological convention or flags (0° meaning wind blowing from North with positive angles increasing in the clockwise direction).

2.3 Flags

All the flags present in the BUFR and HDF product were checked for inconsistencies. We found no meaningful information in the **wvc_quality_flag** (this flag indicates the quality of wind retrieval within a given WVC) of the BUFR product. After reporting the problem to JPL, it turned out that this flag was containing less information and in a different way than the same flag of the HDF product. In order to avoid confusion, they set this flag in BUFR in the same way as in HDF.

a)   Fore Inner (new sample data)

b)   Fore Inner (new sample data + change 180 deg)
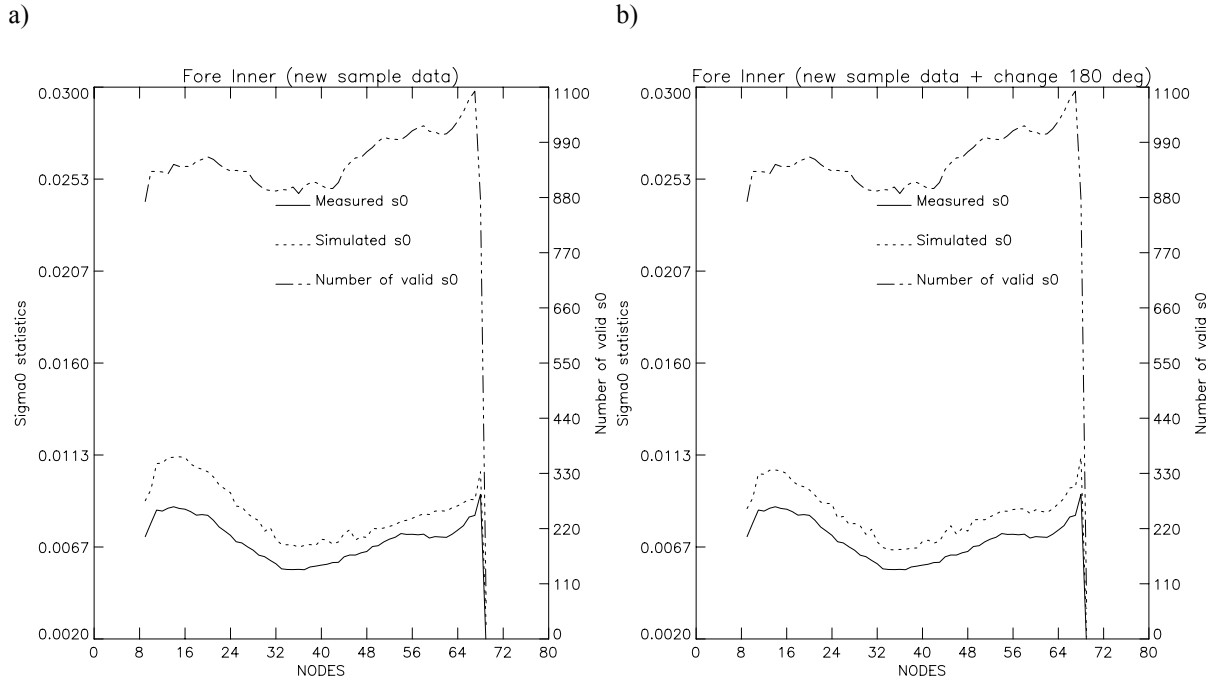
*Figure 6 a) same as Figure 5 but for new sample data; b) same as plot a) but changing the wind direction 180°
prior to computing σ^o_{sim}*

2.4   Other Problems

Every variable contained in the data product is defined between a range of values. The
best way to look for bugs in the processing software is to look for out of range values
and distribution of values in the variables. Here there is a summary of the most
significant bugs we found:

a) A few null Kp_β values per orbit were found in both HDF and BUFR, as well as
some null Kp_γ values in HDF.

b) The Kp_α values of the new sample data were all out of range and the mean Kp_α
value was twice as high as the mean Kp_α value of the old sample data.

[Note: Kp_α, Kp_β, and Kp_γ are the coefficients used to compute the measurement
noise (Kp)]

c) A few values per orbit of the **wind_speed_err** (estimated error in the retrieved
speed) were above 50 m/s; in the same way, some values of **wind_dir_err** (estimated
error in the retrieved wind direction) were above 180°.

d) $\sigma^o < -70$ dB were also found.

All these problems were reported to JPL. We have performed this kind of validation
on the real HDF data and none of these problems are present. The σ^o range has been
extended to [20,−300] dB in the real data. Note that there is no physical lower limit of
σ^o.

The same validation has been recently performed on the real BUFR data. There still are some out of range values in **wind_speed_err** and **wind_dir_err** variables as well as a few null Kp_β values per orbit. As before, we have already reported these problems to JPL.

3   Quality Control

The forecast of extreme weather events is not always satisfactory, while their consequences can have large human and economic impact. The lack of observations over the oceans, where many weather disturbances develop, is one of the main problems of Numerical Weather Prediction (NWP) for predicting the intensity and position of such disturbances. A space-borne scatterometer with extended coverage is able to provide accurate winds over the ocean surface and can potentially contribute to improve the situation for tropical and extratropical cyclone prediction [*Isaksen and Stoffelen* (2000) and *Stoffelen and Van Beukering* (1997)]. The impact of observations on weather forecast often critically depends on the Quality Control (QC) applied. For example, *Rohn et al.* (1998) show a positive impact of cloud motion winds on the European Centre for Medium-Range Weather Forecasts (ECMWF) model after QC, while the impact is negative without QC. The QC is also true for scatterometer data. Besides its importance for NWP, in applications such as nowcasting and short-range forecasting, the confidence of meteorologists in the scatterometer data is boosted by a better QC. Therefore, in order to successfully use scatterometer data in any of the mentioned applications, a comprehensive QC needs to be done in advance.

Stoffelen and Anderson (1997) and *Figa and Stoffelen* (2000) use a method to detect and reject WVCs with poor quality wind information using a Maximum-Likelihood-Estimator-based (MLE) parameter for ERS and NSCAT respectively. Here we adapt this method for QuikSCAT.

The Maximum Likelihood Estimator (MLE) is defined as [adopted from *JPL* (2001)]:

$$MLE = \frac{1}{N} \sum_{i=1}^{N} \frac{\left(\boldsymbol{s}_{mi}^{o} - \boldsymbol{s}_{s}^{o}\right)^{2}}{kp\left(\boldsymbol{s}_{s}^{o}\right)} \tag{1}$$

where N is the number of measurements, σ_{mi}^{o} are the backscatter measurements, σ_{s}^{o} is the backscatter simulated through the Geophysical Model Function (GMF) for different wind speed and direction trial values, and $Kp(\sigma_{s}^{o})$ is the measurement error variance.

Stoffelen and Anderson (1997) interpret the MLE as a measure of the distance between a set of σ_{mi}^{o} and the solution σ_{s}^{o} lying on the GMF surface in a transformed measurement space where each axis of the measurement space is scaled by $kp(\sigma_{s}^{o})$.

The MLE therefore indicates how well the backscatter measurements used in the retrieval of a particular wind vector fit the GMF, which is derived for fair weather wind conditions. A large inconsistency with the GMF results in a large MLE, which indicates geophysical conditions other than those modeled by the GMF, such as for example rain, confused sea state, or ice, and as such the MLE provides a good indication for the quality of the retrieved winds.

Rain Effects

Rain is known to both attenuate and backscatter the microwave signal. *Van de Hulst* (1957) explains these effects. Rain drops are small compared to radar wavelengths and cause Rayleigh scattering (inversely proportional to wavelength to the fourth power). Large drops are relatively more important in the scattering and smaller wavelengths more sensitive. For example, *Boukabara et al.* (1999) show the variation of the signal measured by a satellite microwave radiometer with the rain rate. As the rain rate increases, the spaceborne instrument sees less and less of the radiation emitted by the surface, and increasingly sees the radiation emitted by the rainy layer that becomes optically thick due to volumetric Rayleigh scattering. A dense rain cloud results in a radar cross section corresponding to a 15-20 m/s wind.

Comparing Ku-band (13.4 GHz) to C-band (5 GHz) scatterometers, the higher frequency of the former makes both effects (rain attenuation and scattering) about 50 times stronger. In particular, as SeaWinds operates at high incidence angles and therefore the radiation must travel a long path through the atmosphere, the problem of rain becomes acute.

In addition to these effects, there is a "splashing" effect. The roughness of the sea surface is increased because of splashing due to rain drops. This increases the measured σ^o, which in turn will affect the quality of wind speed (positive bias due to σ^o increase) and direction (loss of anisotropy in the backscatter signal) retrievals.

3.1   Quality Control in HDF[1]

In this Section, we define and characterize a parameter based on the MLE to quality control the QuikSCAT data. Since the first QuikSCAT data available are provided by JPL in HDF format (late September 1999), we will first investigate the Quality Control procedure with this data format.

3.1.1   Methodology

The method consists in normalizing the MLE with respect to the wind and the node number (or cross-track location). The MLE does not uniformly behave over these parameters (wind and node number) and the main reason is that the measurement noise is sometimes miscalculated. In order to avoid this problem, for a given wind and node number, we compute the expected MLE. Then we define the normalized residual as:

---

[1] Based on: Portabella, M., and Stoffelen, A., "Rain Detection and Quality Control of SeaWinds," *J. Atm. and Ocean Techn.*, Vol. 18, No. 7, pp. 1171-1183, 2001, © American Meteorological Society.

Rn = MLE / <MLE>   (2)

where MLE is the maximum likelihood estimator of a particular wind solution (given by the inversion) and <MLE> is the expected MLE for that particular WVC (node number) and wind solution.

We hypothesize that the MLE is very much altered in the case of rain and therefore very different from the expected MLE. A set of σ^o_m coming from a "rainy" WVC (or a WVC where some geophysical phenomena other than wind is "hiding" the wind-related information) is expected to be inconsistent with any set of σ^o_m that is simulated from the GMF, since basic properties of the backscatter measurements such as H-pol to V-pol ratio (Wentz et al., 1999) and the isotropy of scattering at the ocean surface are expected to be different. In other words, the set of backscatter measurements coming from a "rainy" WVC is expected to be further away from the GMF than a set of measurements coming from a "windy" WVC (which should lie very close to the GMF). Therefore, the MLE is much higher than <MLE> and the normalized residual is high. In contrast, the MLE of a "windy" WVC is closer to the <MLE> and consequently we have Rn values of the order of 1.

In order to compute the expected MLE for a given wind and node number we study the dependencies of the MLE with respect to the wind speed, wind direction and node number over 60 revolutions of real data.

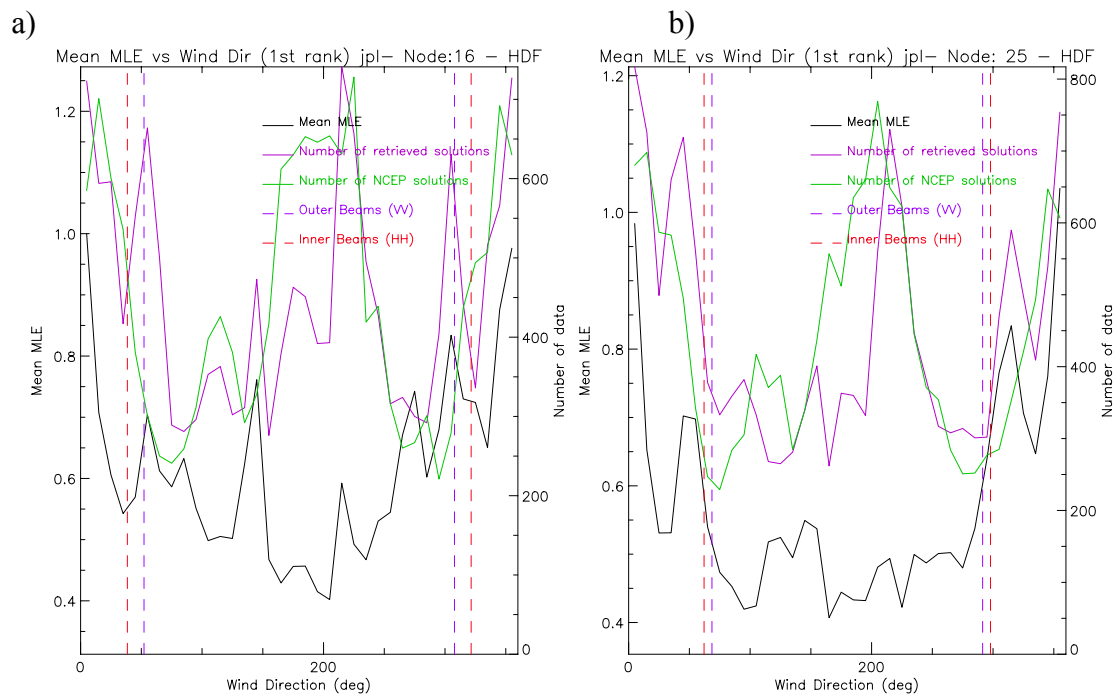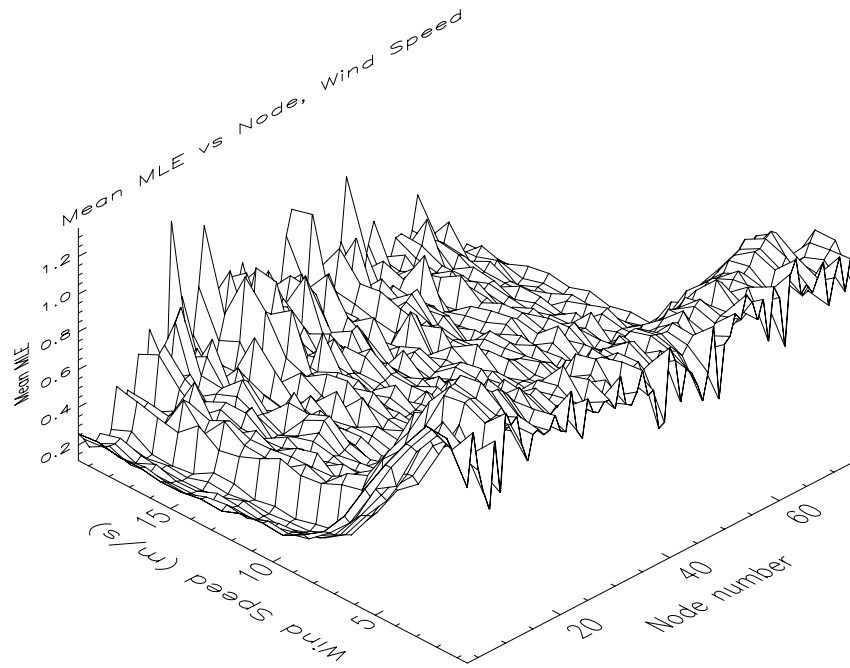*Figure 7 Mean JPL-selected MLE versus JPL-selected wind direction (solid black line) and wind direction distribution of JPL-selected winds (solid purple line) and NCEP winds (solid green line) for nodes 16 (plot a) and 25 (plot b). The direction binning is 10° and the vertical dashed lines correspond to the azimuth of inner (red) and outer (purple) beams with respect to the cross-track flight satellite direction.*

Figure 7 shows the mean MLE of the JPL-selected solution versus JPL-selected wind direction together with the wind direction distribution of both the NCEP model and the JPL retrieved solutions (the selected solution after ambiguity removal) for nodes 16 (plot a) and 25 (plot b). The JPL direction distribution shows some significant differences (peaks and troughs) as compared to the NCEP distribution, which may be associated to some deficiencies in the inversion and the NSCAT-2 model function. We note that the mean MLE is following these relative peaks and troughs of the JPL wind direction distribution with respect to NCEP. This is an expected result as measurement sets far away from the GMF solution surface in measurement space (*Stoffelen*, 1998), i.e., with large MLE, are systematically assigned to certain wind directions (the shape of the GMF solution surface makes certain wind directions to be favoured in such cases). However, these peaks are due to an inversion problem and not to a realistic MLE dependency on wind direction. In other words, the mean MLE peaks are not always showing a real MLE dependency on wind direction but just some artificial accumulation of wind direction solutions due to some deficiencies in the inversion. Therefore, we discard the wind direction dependency when computing the <MLE>.

As such, <MLE> is computed as a function of wind speed and node number. The method to compute <MLE> is as follows:

- We compute the mean MLE of the JPL-selected solution with respect to the JPL-selected wind speed and the node number for the 60 revolutions of HDF data. Figure 8a shows a 3D plot of this mean MLE. The surface is a bit noisy, which is mainly due to geophysical effects such as rain, which we want to discard. At high wind speeds additional noise is present due to the small amount of data we get at these speeds and node numbers.

- In order to filter the noise on the surface, we set up an iterative process which consists in rejecting the MLEs which are at least two times higher than the mean MLE for that particular wind speed and node number, and we compute again the mean MLE surface. Then, we start the rejection process again in an iterative mode until it converges (no more rejections). The process converges very rapidly after two iterations and the number of data rejected in each speed and node bin is very small (up to 7% in some high-speed bins). This gives faith in the noise filtering method as it shows that only the tail of the MLE distribution is cut in each bin, corresponding to geophysical anomalies. The resulting surface is shown in Figure 8b. The peaks have disappeared in general and at high speeds the surface is much smoothed. In order to show the consistency of this filtering procedure, we show the contour plots of both mean MLE surfaces (before and after filtering) in Figure 9. It is clearly discernible that the shape of the surface remains the same and only the noise has been removed.

- In order to extrapolate to high wind speeds, we fit in a very simple way a two-dimensional function to the filtered surface (see Appendix A). The function is only fit in the inner swath (nodes 12 to 65) and extrapolated for the outer swath (nodes 1 to 11 and 66 to 76) (see discussion below). The result of the fitting is shown in Figure 10. The 3D surface is the expected MLE and compares well to the computed mean MLE in the inner part of the swath.
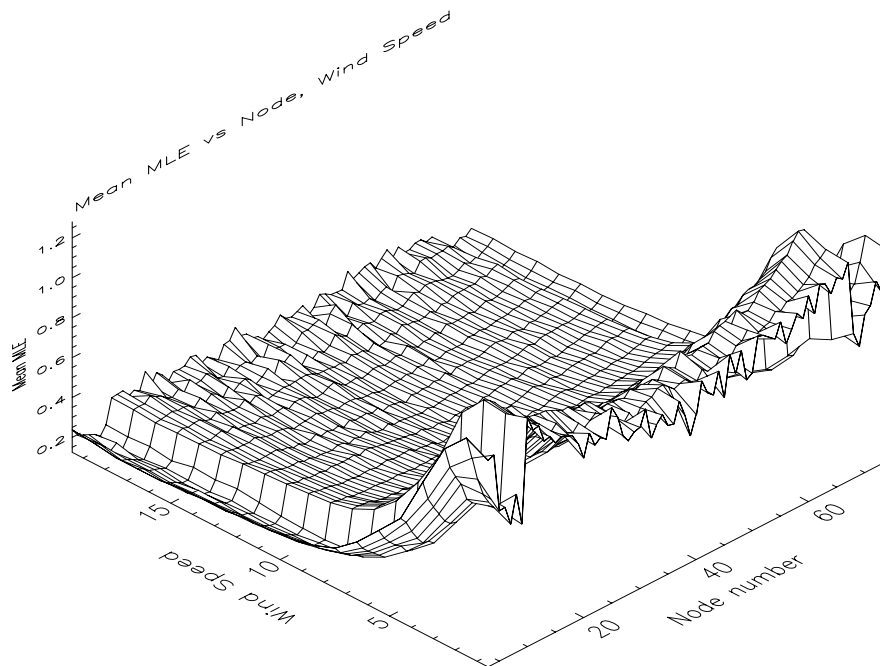
a)

b)

Figure 8 Mean JPL-selected MLE (plot a) and "filtered" mean JPL-selected MLE (plot b) versus JPL-selected wind speed and node number. The speed binning is 1 m/s and the node binning is 1

a)　　　　　　　　　　　　　　　　b)
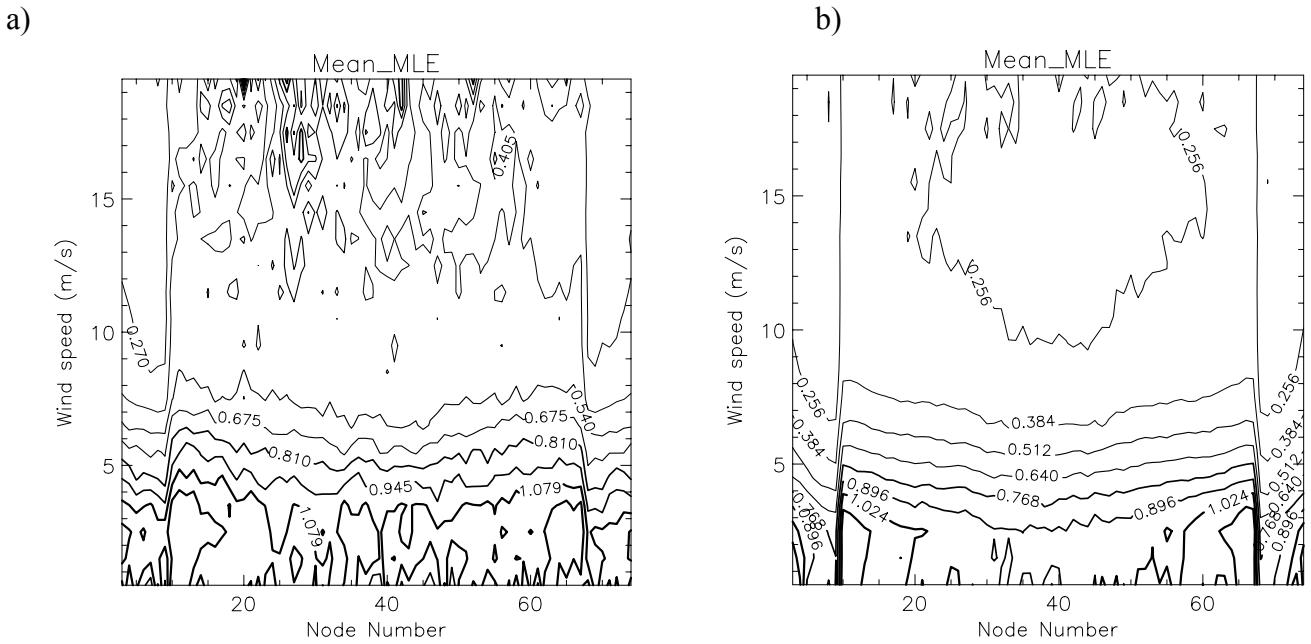
Figure 9 Contour plots of Figure 8a (plot a) and 8b (plot b).

As said before, large departures from fair weather conditions result in a large MLE value. In turn, this MLE, larger than its corresponding expected MLE, results in a large Rn. Therefore, large Rn is indicating bad quality of the retrieved winds for any given WVC.

However, this correlation between the MLE and its expected value is expected to work well when there are more than two measurements and enough azimuth diversity in the σ^o measurements of each WVC, i.e., when the inversion problem is overdetermined. In the outer parts of the swath, where there are only one or two beams (fore and/or aft VV), the wind vector is not overdetermined and generally multiple wind speed and direction combinations exist that exactly fit the measurements. Then the MLE is going to be zero or very close to zero in most of the cases, regardless of the quality of the data. Only for the exceptional case when the MLE is substantially larger than our extrapolated <MLE> we can infer that the data are of bad quality in these parts of the swath. This means that our QC procedure is generally not going to work well in the outer regions. Nevertheless, to provide a gross check and in order to arrive at a simple function fit to the <MLE> surface, we have extrapolated the inner swath function to the outer regions.

Once Rn is defined, we have to characterize it. The way to characterize Rn is to test it against a variety of geophysical conditions such as rain, confused sea state (in wind fronts, centre of lows, coastal regions) or just pure wind cases. As the method is expected to work fine in the inner swath, especially in its sweet parts (nodes 12 to 28 and 49 to 65), we are going to focus our research on these regions.
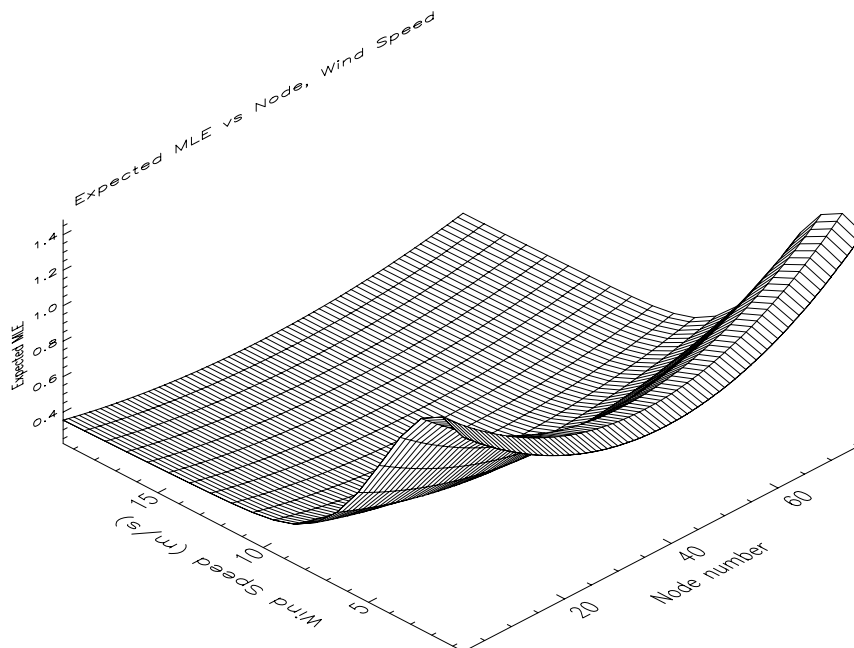
Figure 10 Expected MLE versus wind speed and node number. The speed binning is 1 m/s and the node binning is 1.

3.1.2 Collocations

In order to characterize QC by Rn, we collocate a set of 180 orbits of QuikSCAT HDF data with ECMWF winds and SSM/I rain data. The HDF data correspond to the preliminary science data product produced by JPL using the NSCAT-2 GMF.

We use the analyses 3-hour and 6-hour forecast ECMWF winds on a 62.5-km grid and we interpolate them both spatially and temporally to the QuikSCAT data acquisition location and time respectively.

The collocation criteria for SSM/I rain data are less than 30 minutes time and 0.25º spatial distance from the QuikSCAT measurement.

The SSM/I instruments are on board DMSP (Defense Meteorological Satellite Program) satellites. We have used DMSP F-13 and F-14 satellites (the most recent ones). Most of the collocations with F-13 were found at low latitudes (tropics) while collocations with F-14 were found at mid and high latitudes.

3.1.3 Rn characterization

In this section, we study the correlation between Rn and the quality of QuikSCAT winds. Collocated ECMWF winds and SSM/I rain are used as characterization and validation tools. Note that both the ECMWF winds and SSM/I rain data contain uncertainties and obey different space and time representations than the QuikSCAT winds.

Characterizing Rn results in a QC procedure by finding a threshold value of Rn which separates the good quality from the low quality retrieved winds.

As said in section 3.1.1, the Rn is defined from the MLE of the JPL-selected solution. Therefore, if we identify a low quality wind selected solution we will assume that all wind solutions in that particular WVC are of low quality. This means that the QC is performed on a node-by-node basis. Nodes that are accepted may have wind solutions with MLE above the threshold. These solutions are kept but will be down-weighted in the data assimilation procedure (*Stoffelen et al.*, 1999).

We characterize Rn in the sweet parts of the swath, where it is most meaningful. However, as we show in the validation, the threshold is applicable for the entire inner swath.

Rn as a quality indicator

The first step in the characterization of this QC procedure is to confirm the correlation between Rn and the quality of the data. The vector RMS difference between the JPL-selected and ECMWF winds (RMS-ECMWF) is used as a quality indicator.

Figure 11 shows a contour plot of a two-dimensional histogram of RMS-ECMWF against Rn. We set an arbitrary threshold at RMS=5 m/s which is roughly separating the "good" from the "bad" quality cases. Plot a), which represents the whole collocated data set, shows a clear correlation between RMS-ECMWF and Rn. Most of low Rn cases, represented by the two darkest grey-filled contours (remember that the plots are in logarithmic scale), are of good quality. The RMS-ECMWF increases as Rn increases, which means that, as expected, the quality of the data is decreasing while Rn increases, i.e., Rn is a good quality indicator.

Plots b) c) and d) show a different histogram distribution with respect to wind speed. The RMS-ECMWF is increasing more rapidly with Rn at higher wind speeds. The quality of the data is poor for lower values of Rn as the retrieved wind speed increases. This suggests a Rn threshold dependent on the retrieved wind speed with a threshold value smaller at high wind speeds than at low speeds.
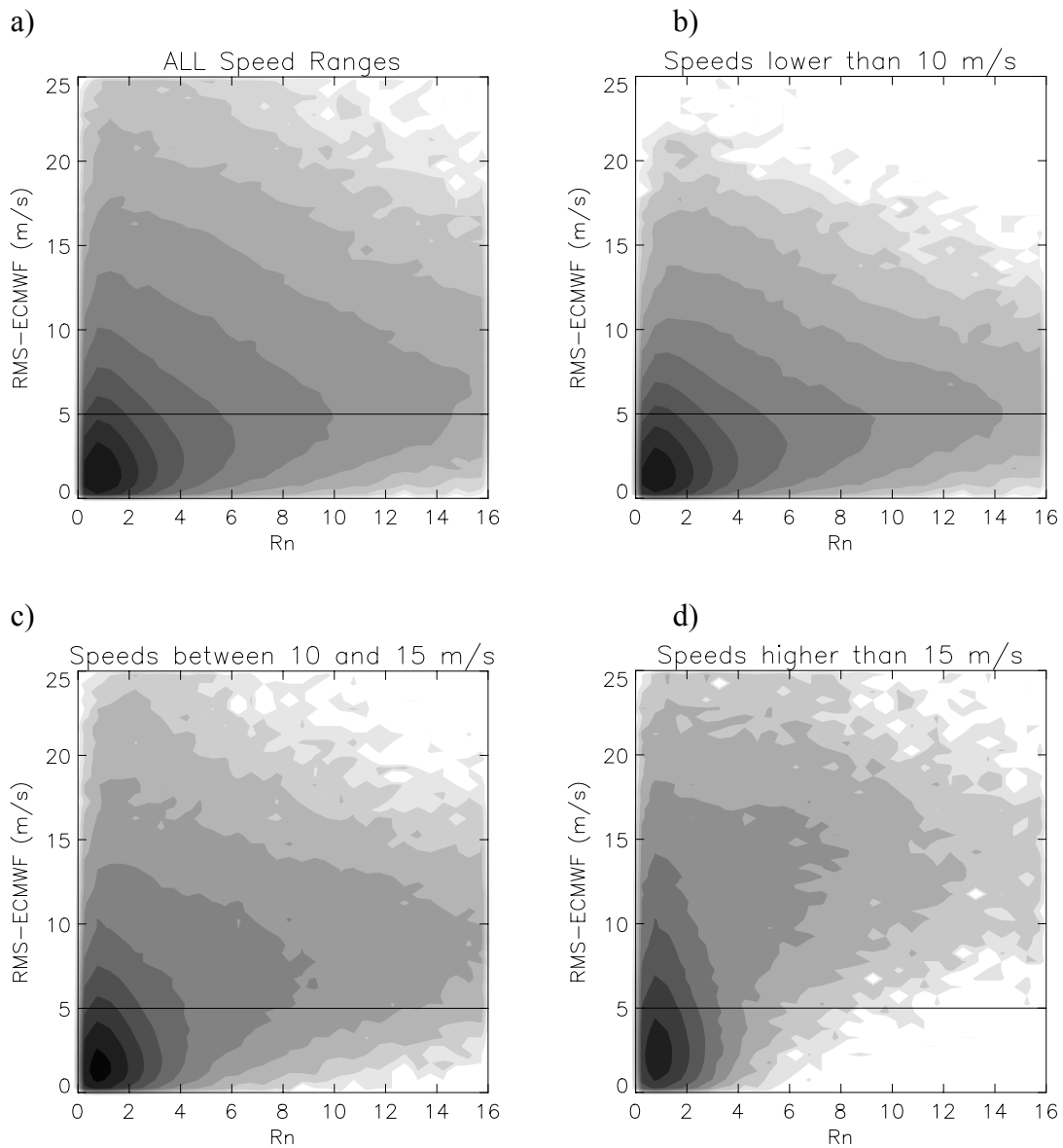
Figure 11 Two-dimensional histograms of RMS-ECMWF versus Rn, for all data (plot a), JPL-selected speeds under 10 m/s (plot b), speeds between 10 and 15 m/s (plot c) and speeds over 15 m/s (plot d). The contouring is in logarithmic scale (two steps corresponding to a factor of 10 in number density) filled from white (unpopulated areas) to black (most populated areas).

Quality Control of rain

As said before, the Ku-band signal is known to be distorted in the presence of rain. In order to study this distortion effect, SSM/I collocations are used as a rain indicator.

Figure 12 shows both the mean retrieved wind speed (plot a) and the mean ECMWF wind speed (plot b) versus the rain rate. The retrieved wind speed is increasing with the rain rate while the ECMWF wind speed shows obviously no significant dependence on the rain. As the rain rate increases, the density and size of the droplets increases and the probability of having a homogeneous rainy WVC (no patches with absence of rain) increases. Therefore, the wind information contained in a particular WVC is increasingly hidden and the backscatter signal is becoming more and more

"rain-related" instead of "wind-related". From these plots, one may infer that the "rainy" WVCs produce high winds in the retrieval process.

a)   b)
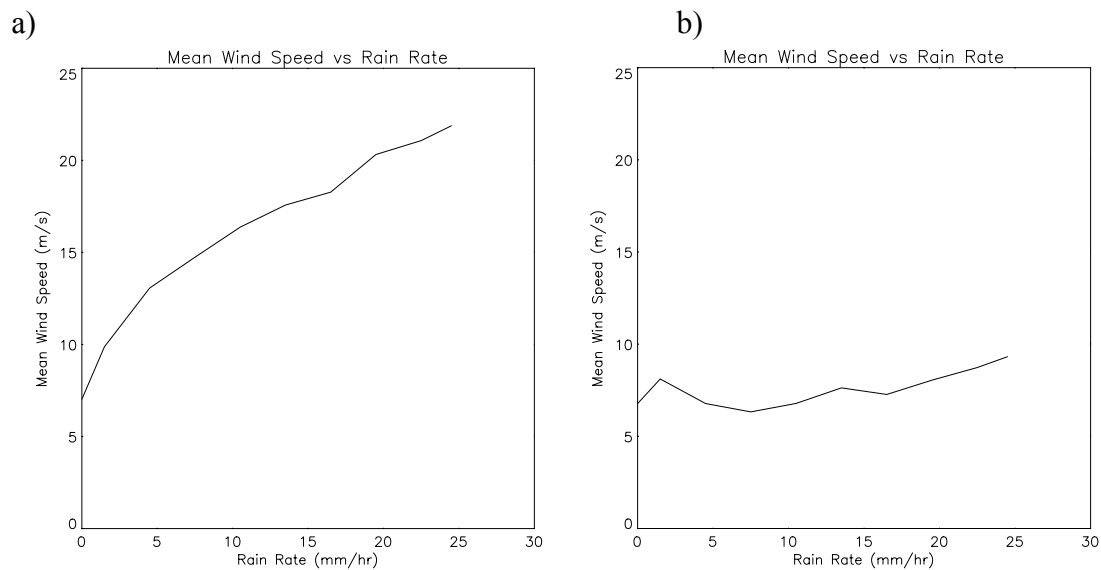
Figure 12 Mean JPL-selected wind speed (plot a) and Mean ECMWF wind speed (plot b) versus rain rate at intervals of 3 mm/hr (except for the rain-free mean speed value, included at 0 mm/hr)

Figure 13 shows the two-dimensional histogram of RMS-ECMWF versus the retrieved wind speed for rain-free (plot a) and for different rain rate intervals (plots b and c). The upper plot shows a generally horizontal orientation of the contour lines while the bottom plots show mainly a vertical orientation, suggesting a decline of the data quality (higher mean RMS-ECMWF) in the presence of rain. At rain rates higher than 6 mm/hr most of the data are above the RMS threshold of 5 m/s, indicating no useful wind information in them. However, when the rain is lower than 6 mm/hr there is still a significant portion of the retrieved winds with low RMS and therefore containing significant wind information in their backscatter signal. We want to define a threshold capable of removing those "rainy" WVCs with rain rates over 6 mm/hr and those with lower rain rates but no significant wind information (high RMS-ECMWF values) in them.

Rn threshold

Up to now, we have achieved three major conclusions:

a) The Rn seems a good quality indicator

b) When it is rainy, the retrieved wind speed is in general too large by an amount which is proportional to rain rate

c) For SSM/I rain rates above 6 mm/hr the WVCs contain no valuable wind information.

a)

b)   c)
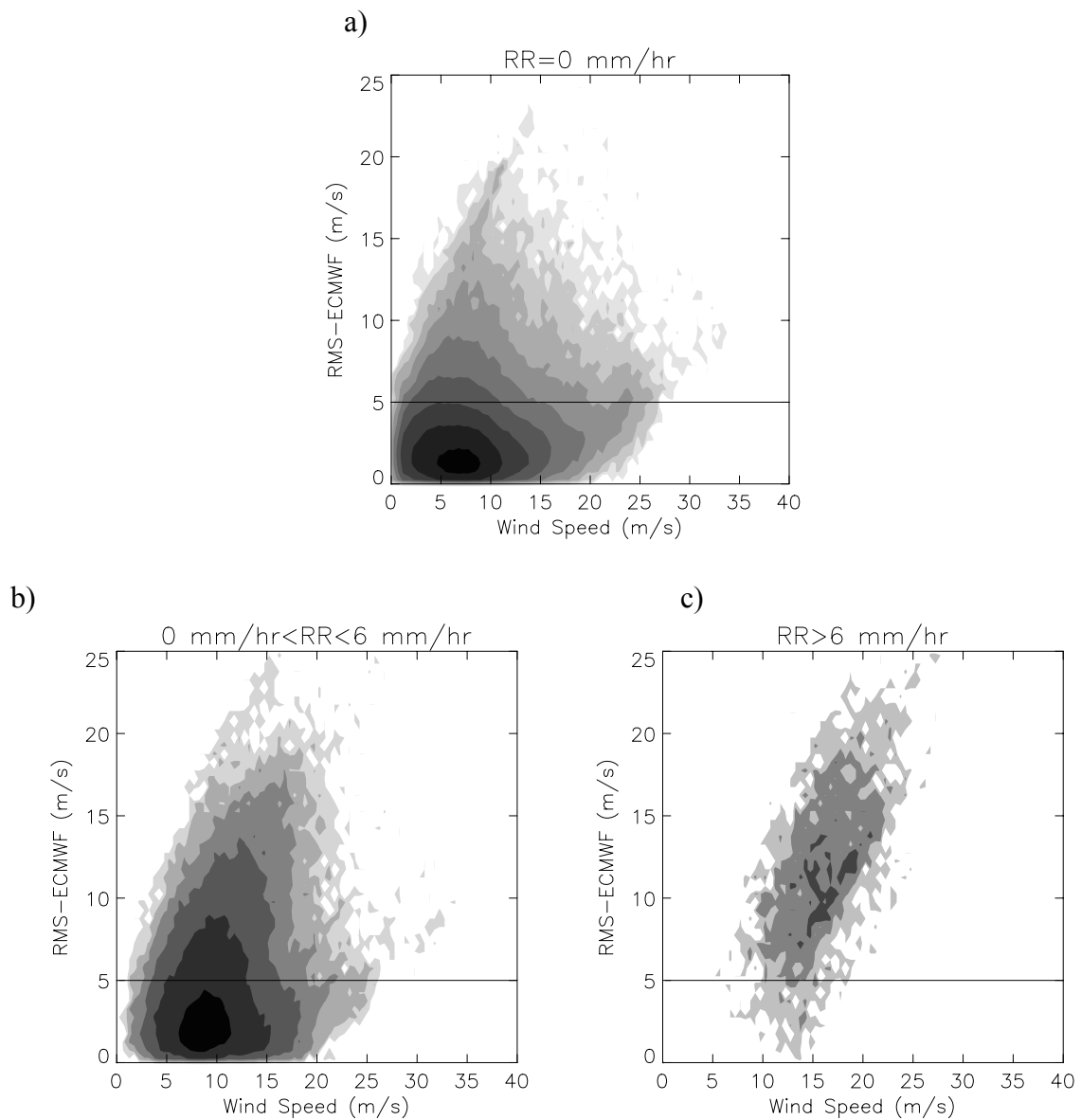
Figure 13 Two-dimensional histograms of RMS-ECMWF versus JPL-selected wind speed for rain-free (plot a), for rain rates from 0 to 6 mm/hr (plot b) and for rain rates above 6 mm/hr (plot c). The contouring is in logarithmic scale (two steps corresponding to a factor of 10 in number density) filled from white (unpopulated areas) to black (most populated areas).

Figure 14 summarizes all these points. The left plots correspond to two-dimensional histograms of Rn versus JPL retrieved wind speeds for different rain rate intervals. The right plots are the same histograms of Rn but versus ECMWF wind speed. In the absence of rain (upper plots), we clearly discern the significant difference between the retrieved and ECMWF wind speeds at Rn values larger than 4 (see speed shift in the contour line), denoting a poor quality of the retrieved solutions. Thus, in case of no rain high Rn is seemingly associated with systematically wrong winds. This wind speed difference at Rn values larger than 4 becomes significantly larger (2-3 m/s) in the mid plots while for low Rn (darkest contour) there is no significant difference. This is denoting that although at mid and high winds the wind retrieval is not very much affected by low rain rates, at low winds the sensitivity to rain is so important that even at low rain rates the quality of the retrievals is poor. This is an expected result as for low winds you get lower backscatter than for high winds and therefore

the backscattering from the rain droplets becomes more significant. Comparing the contours from the left and the right plots, there is a positive shift of the left ones with respect to the right ones (indicating a positive bias of the retrieved speeds with respect to ECMWF speeds) as the rain rate increases. This shift is becoming excessively large and unacceptable (more than 10 m/s) for rain rates over 6 mm/hr (bottom plots), denoting again the poor quality of the retrieved solutions.

In the definition of a Rn threshold we would like to achieve the following goals:

- Maximum low-quality data rejection, including rain;

- Minimum good-quality data rejection.

As said before, the Rn threshold may be dependent on the retrieved wind speed. Figures 14a and 14b (no rain) suggest that the threshold should include and follow the contour lines that are very similar in both plots (showing good quality data). Obviously, this threshold should become constant at a certain wind speed. Otherwise, we would start rejecting more and more data for increasing wind speed, until the threshold reaches zero at a certain wind speed from where on all higher retrieved speeds would be rejected. Figures 14a and 14b do not suggest poor quality of all high wind speeds. The constant threshold value has to be a compromise between the amount of high-wind data we want to keep and the amount of "rainy" data we want to reject.

From Figure 11, it is obvious that for higher winds we should be more critical with the Rn threshold. Therefore and in order to reject most of the "rainy" data (see Figure 14e), we define a minimum threshold value of 2 for speeds higher than 15 m/s. From Figures 14a and 14b, we define a parabolic threshold with a maximum value of 4 at 5 m/s, which reaches a value of 2 at 15 m/s (see Rn threshold in black solid lines in Figure 14). Therefore, the defined threshold function is:

$$v \leq 15m/s \qquad y = y_0 + A \cdot (v - v_0)^2$$
$$v > 15m/s \qquad y = 2$$
$$where, \qquad\qquad\qquad\qquad\qquad\qquad\qquad\qquad (3)$$
$$y_0 = 4, A = -\frac{2}{100}, v_0 = 5,$$

v is the retrieved wind speed and y the Rn threshold value.

Note that we have tested different thresholds including: 1) different parabolas with maxima and minima at different Rn/Speed locations; 2) a constant value for all wind speeds; and 3) a constant value for all speeds but with a step (change in value) at different wind speed locations. None of them have given better results than the one defined above according to our statistics and the two previously mentioned goals.

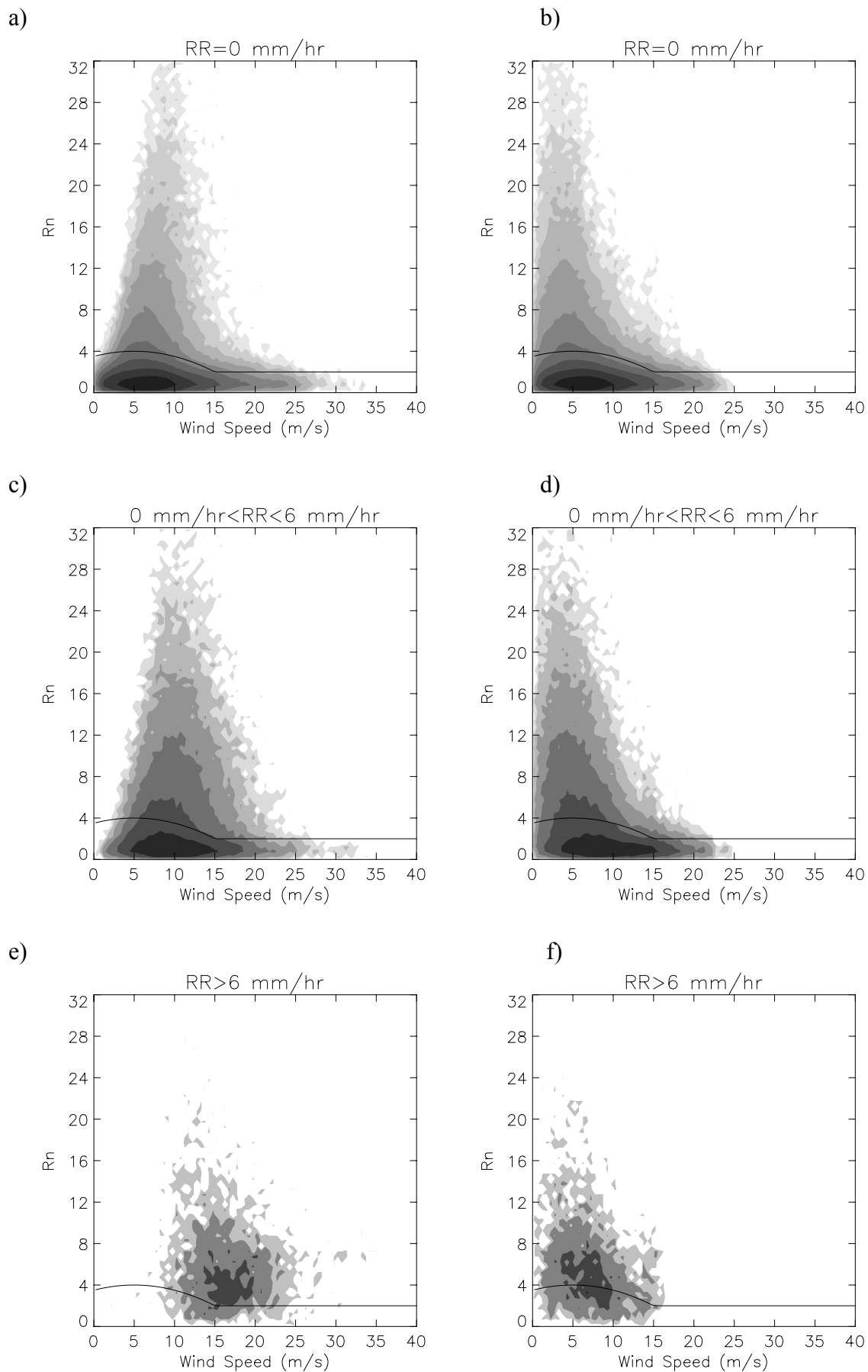*Figure 14 Two-dimensional histograms of Rn versus JPL-retrieved wind speed (left plots) and versus ECMWF speeds (right plots) for rain-free data (plots a and b), for rain rate from 0 to 6 mm/hr (plots c and d), and for rain rate above 6 mm/hr (plots e and f). The contouring is in logarithmic scale (two steps corresponding to a factor of 10 in number density) filled from white (unpopulated areas) to black (most populated areas).*

3.1.4 Threshold validation

We test the defined threshold against the ECMWF and SSM/I collocations. The test consists of looking at the Rn of the selected solution of any WVC. If the Rn is lower or equal to the threshold, the WVC is accepted; otherwise, the WVC is rejected. The results for the sweet parts of the swath are shown in tables 1, 2 and 3.

Table 1 shows the percentage of accepted and rejected WVCs from all the WVCs, segregated by wind speed intervals. 5.6% of data are rejected and the rejection rate is increasing with wind speed. This is an expected result. As "rainy" cells result in higher retrieved wind speeds (the larger the rain rate the larger the speed bias) and we want to get rid of those cells, the amount of rejections should increase with wind speed. However, in order to reject rain we have defined a threshold which is decreasing with wind speed (up to 15 m/s where it remains constant) and therefore we might reject an increasing amount of "good" solutions as well.

Table 2 shows the total and the percentage of the accepted and rejected solutions for above and below a RMS-ECMWF threshold of 5 m/s. For the total, accepted and rejected classes, the different mean RMS-ECMWF value is also shown. On the one hand, there is a very small portion of rejected data (2.9 %) with RMS values below 5 m/s, indicating that most of the "good" quality solutions have been accepted. On the other hand, there is a significant percentage of rejected data (35.2%) with RMS values over 5 m/s, showing that the Rn threshold is effective in rejecting poor quality data. The difference between the mean RMS of rejected and accepted data is 4 m/s, showing again the effectiveness of the Rn threshold.

Table 3 shows the percentage of the accepted and rejected solutions divided by rain rate intervals. When there is no rain, the percentage of rejections is 3.4%. If we compare this result with the total portion of rejections given in table 1 (5.6%) we can conclude that in more than 2% of the cases we are rejecting "rainy" cells. When the rain is over 6 mm/hr, most of the "rainy cells" are rejected (87.3%), denoting a very good behaviour of the Rn threshold. When the rain is lower or equal to 6 mm/hr, the percentage of rejections decrease significantly (29.4%) compared to higher rain rates. As said in the previous section, at these rain rates we are still getting "fair" quality winds (with enough wind information) which we may want to keep, but still there is a significant portion of low winds (see discussion of Figure 14) of low quality which are rejected. In this sense, we achieve a good compromise in the screening of cases in the absence of rain (3.4% of rejections) and in cases of SSM/I rain over 6 mm/hr (87.3% of rejections).

Figure 15 shows the two-dimensional histograms of RMS-ECMWF versus retrieved wind speed for different rain intervals. The left plots correspond to the accepted solutions and the right plots to the rejected solutions. It is clear when comparing the contour lines of the left with the right plots that the latter show a much more vertical orientation with the maximum (darkest contour) significantly higher than the former (accepted solutions). This is a way to show the mean RMS difference between the

accepted and the rejected solutions presented in table 2. For rain rates over 6 mm/hr (see bottom plots) most of the solutions are rejected.

Comparing the distributions of Figures 13a and 13b (prior to QC) with the distributions of Figures 15a and 15c (accepted solutions), it is discernible that either for no rain or for rain rate lower than 6 mm/hr, the distributions have become flatter (less vertically oriented) after QC. This indicates a general decrease of the mean RMS and therefore a good performance of the method.

Tables 4, 5 and 6 are the same as tables 1, 2 and 3 but for the nadir swath. In the nadir swath, there is not always enough azimuth diversity in the σ^o beams. In particular, WVCs very close to the nadir have fore and aft beams 180º apart, which is almost the same as having only one of the two beams. As said in Section 3.1.1, when there is not enough azimuth diversity this QC procedure may not work well. Therefore, we expect a lower skill of the QC in the nadir swath compared to the sweet swaths. And this is what we see in the results shown in the tables mentioned above.

Comparing table 4 with table 1, we see a larger percentage of rejections in the nadir swath, which increases with wind speed. At speeds higher than 15 m/s, 23.8% of the data are rejected. This represents almost 5% more rejections than in the sweet spots.

Comparing table 5 with table 2, there is a slightly larger percentage of rejections at RMS-ECMWF < 5m/s and a smaller percentage of rejections at RMS-ECMWF > 5m/s in the nadir swath, indicating a slight decrease in the performance of the QC procedure. Although the mean RMS-ECMWF of the accepted solutions is slightly higher in the nadir swath, the mean RMS-ECMWF difference between accepted and rejected solutions is the same (4 m/s), showing a comparable result in both regions.

Comparing table 6 with table 3, when rain is over 6 mm/hr there are slightly less rejections in the nadir swath. This shows again a slightly worse performance in the nadir swath, especially if we consider that overall (see tables 1 and 4) this region suffers more rejections (especially at high winds, where the rain is "located"). However, the percentage of rejections for rain under 6 mm/hr is about 6% higher in the nadir swath. Most of these rejections have an RMS-ECMWF over 5 m/s. This result is unexpectedly positive, as even if the overall portion of rejections with RMS-ECMWF > 5 m/s (see tables 2 and 5) is about 6% smaller in the nadir swath, the portion of rejections when the rain is below 6 mm/hr is around 6% higher for the nadir swath.

In general, the skill of the QC procedure is good in both regions of the swath, although it is slightly better in the sweet region.

We have also tested a QC based on the MLE of the first rank instead of the selected solution. It shows similar results although the QC based on the selected solution is marginally better. A possible explanation for this small difference is that there is more correlation between a geophysical disturbance and the MLE of the selected solution rather than with the MLE of the first-rank solution. In other words, there is some correlation between the data quality and the number of the wind solutions and their corresponding MLE values. Ambiguity removal then picks the geophysically most consistent solution. Therefore, we recommend to use the QC based on the selected solution.

TABLE 1

	Total	V<10	10≤V≤15	V>15
Num. Points (n/a)	4826841	3796408	859747	170686
Accepted (%)	94.4	95.8	91	81
Rejected (%)	5.6	4.2	9	19

TABLE 2

	RMS<5	RMS>5	Mean RMS (m/s)
Total (n/a)	4429905	396970	2.46
Accepted (%)	97.1	64.8	2.24
Rejected (%)	2.9	35.2	6.24

TABLE 3

	RR=0	0<RR≤6	RR>6
Num. Points (n/a)	1027124	88311	3664
Accepted (%)	96.6	70.6	12.7
Rejected (%)	3.4	29.4	87.3

TABLE 4

	Total	V<10	10≤V≤15	V>15
Num. Points (n/a)	2812095	2186477	511131	114487
Accepted (%)	93.7	95.9	88.5	76.2
Rejected (%)	6.3	4.1	11.5	23.8

TABLE 5

	RMS<5	RMS>5	Mean RMS (m/s)
Total (n/a)	2483112	329113	2.81
Accepted (%)	96.8	70.6	2.55
Rejected (%)	3.2	29.4	6.62

TABLE 6

	RR=0	0<RR≤6	RR>6
Num. Points (n/a)	572894	47529	2526
Accepted (%)	96	64.5	14.8
Rejected (%)	4	35.5	85.2

Note : RMS is refered as the vector RMS difference between JPL-retrieved winds and ECMWF winds in m/s; V is the JPL-retrieved wind speed in m/s; and RR is the SSM/I rain rate in mm/hr.

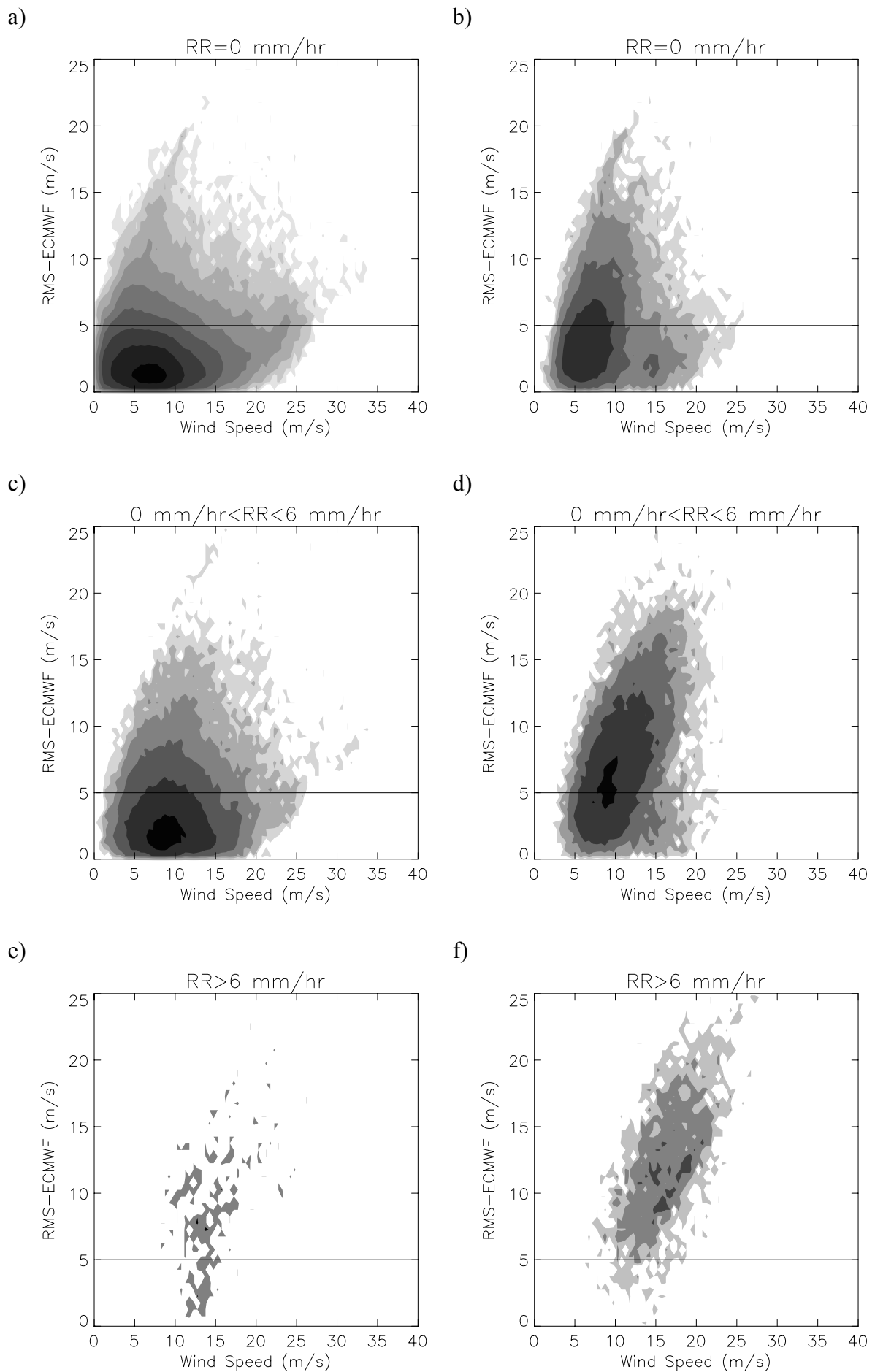*Figure 15 Two-dimensional histograms of RMS-ECMWF versus JPL-retrieved wind speed for the accepted (left plots) and rejected WVCs (right plots). Plots a and b correspond to rain-free data, plots c and d to rain rate from 0 to 6 mm/hr and plots e and f to rain rate above 6 mm/hr. The contour areas are in logarithmic scale (steps of 0.5) filled from white (unpopulated areas) to black (most populated areas).*

3.1.5 Cases

In this section, we show a few wind field examples where the QC procedure has been applied. Figures 16, 17 and 18 show triple collocated QuikSCAT-ECMWF-SSM/I data. The arrows in plot a) correspond to the QuikSCAT JPL-selected wind solutions and the colors represent the accepted (green) and the rejected (red) solutions by the Rn threshold (QC). The squares correspond to the collocated SSM/I rain data, where the size of the squares annotates rain rate. The arrows in plot b) correspond to the collocated ECMWF winds. The violet solid lines divide the different regions of the swath (outer, sweet and nadir).

In Figure 16, there is a case of significant rain (up to 25 mm/hr) over the entire plot, especially in the mid-left and upper-right parts. It is clearly discernible that most of the areas with rain rate above 6 mm/hr (mid-large squares) are rejected by the QC.

At about 12º latitude, there is a "band" of rejections going from the centre to the right side of the plot. This area is dividing a mid and high wind speed area (south part) from a low speed one (north part), suggesting the presence of a wind front. The QC is performing well as in the frontal area, confused sea state is expected (due to high temporal wind variability) and therefore poor quality wind solutions exist. The wind field in plot b (ECMWF wind field) does not at all reflect the spatial detail seen in plot a, showing a potential positive impact of assimilation of QuikSCAT winds into the ECMWF model.

Although the low wind speed region shows some erratic flow patterns, most of the wind solutions have been accepted by the QC. This region is mostly located in the nadir part of the swath. As said before, in the nadir regions there is a lack of azimuth diversity in the σº beams. This is going to affect the skill of the wind retrieval, in particular at low wind speeds where the GMF is less sensitive to wind direction changes. Our QC will not detect these points since they do not exhibit large Rn. However, we think that improved inversion schemes could produce solution patterns that are more consistent. This will be investigated in the future.

In Figure 17a, the presence of a wind front is clearly discernible in the middle of the plot, where again a confused sea state and therefore poor quality winds are expected. WVCs along the front line are rejected by QC. This is also the case for the centre of the low at the bottom of the plot, where there is probably extreme temporal and spatial sea state variability or rain. At the left side of the wind front we see a region of significant rain (above 6 mm/hr) which has been successfully detected by the QC. In the outer swath region (right side of the plot), there are very few rejections as expected (see section 3.1.1). In general, the QC does not detect much of the poor quality data in the outer regions. However, in this case, the flow looks consistent and therefore the QC apparently seems to work.

The ECMWF forecast (plot b) does not accurately place the centre of the low and the associated wind front is not so pronounced as in the QuikSCAT plot. This example

illustrates again the potential positive impact of assimilating QuikSCAT winds into ECMWF after using our QC.

Figure 18 is a clear pure wind case. No fronts were predicted by ECMWF (plot b) and almost no rain was observed by SSM/I. Most of the wind solutions have been accepted by the QC. Indeed, QuikSCAT winds show a meteorologically consistent pattern, indicating again a good performance of this QC.

CASE : 02/09/99 1400 UTC
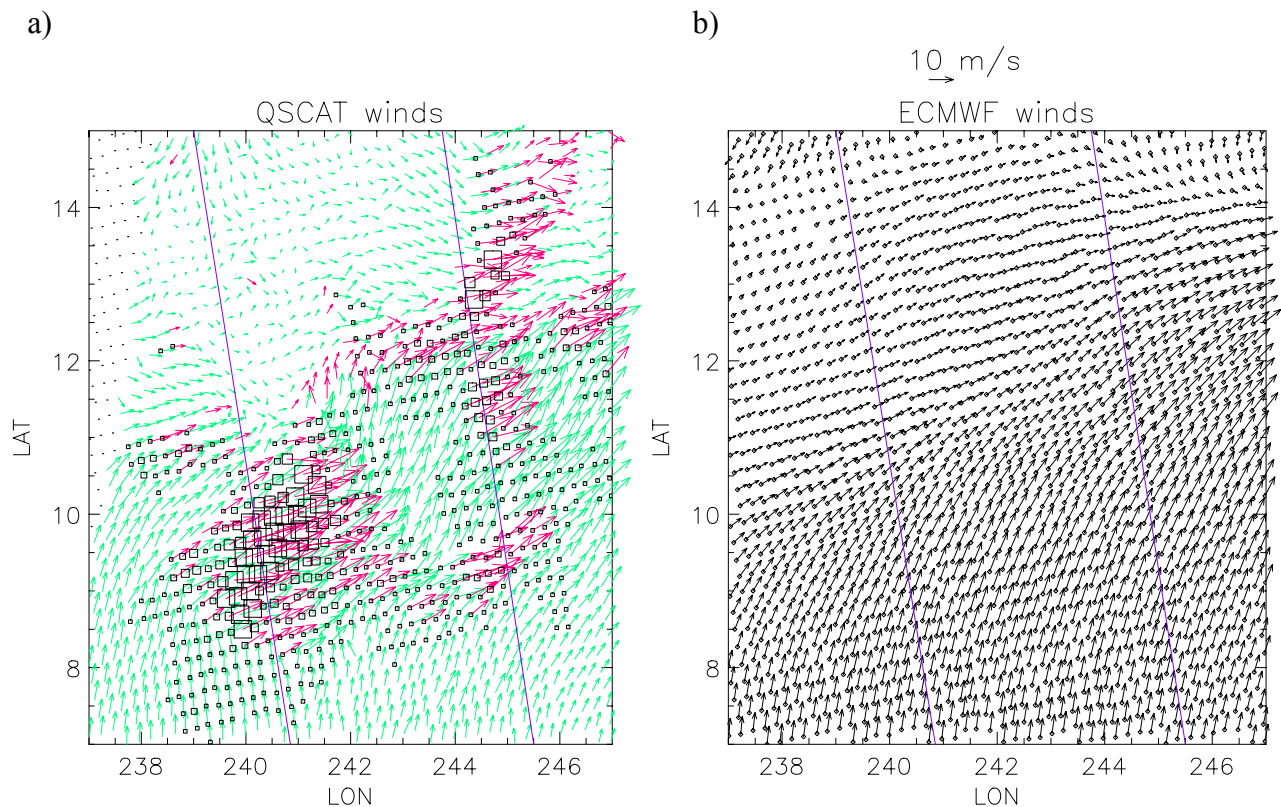
Figure 16 Collocated QuikSCAT-ECMWF-SSM/I data. Plot a shows QuikSCAT wind arrows (JPL-selected winds), where green color correspond to accepted WVCs and red color to rejected WVCs. The size of the squares represent the different rain rates from 0 mm/hr (no square) to 25 mm/hr (the largest ones). Plot b shows the collocated ECMWF winds. The violet lines separate different regions of the swath. In this case, the left side of the plot corresponds to the sweet-left region, the middle to the nadir region and the right side to the sweet-right region. The acquisition date was September 2 1999 at 14 hours UTC

CASE : 28/08/99 0500 UTC

a)

b)
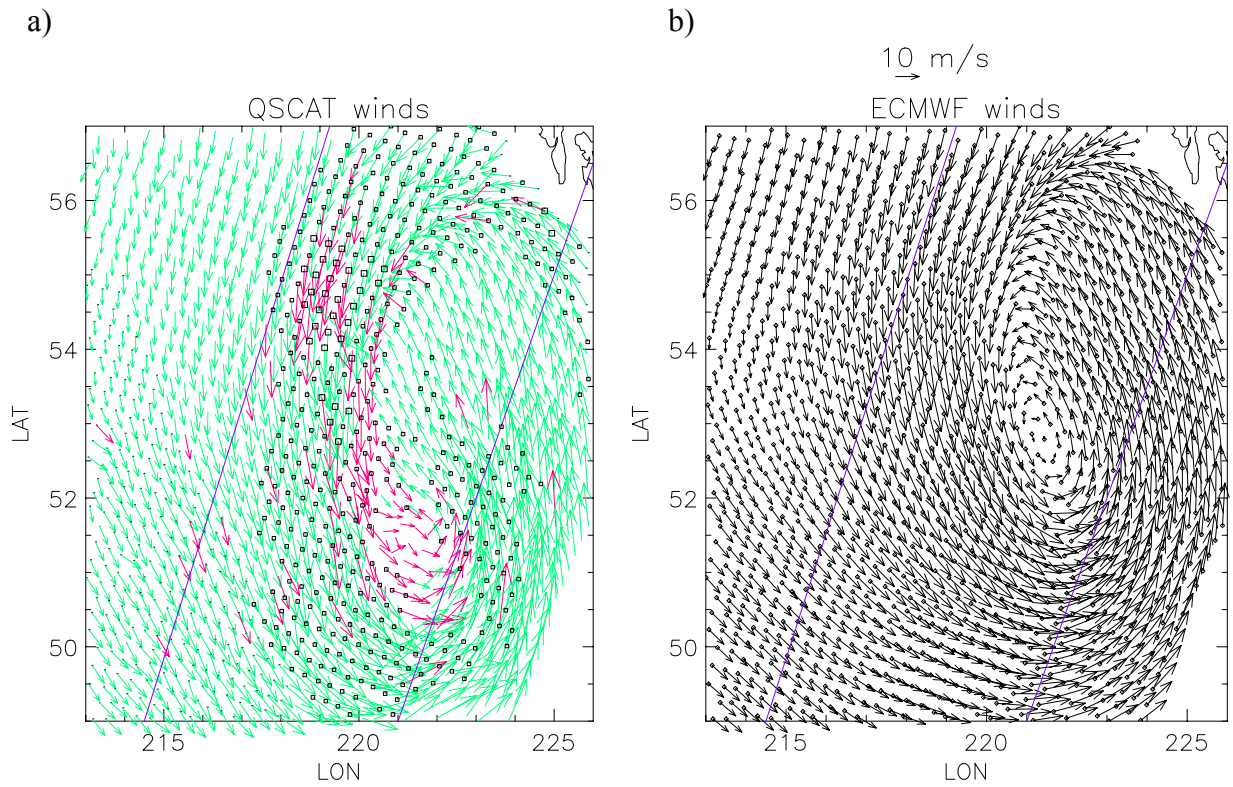
Figure 17 Same as Figure 16 but for different date (August 28 1999 at 5 hours UTC) and location. The violet lines separate the nadir (left side), the sweet-left (middle) and the outer-left (right side) regions.

CASE : 28/08/99 1000 UTC

a)

b)
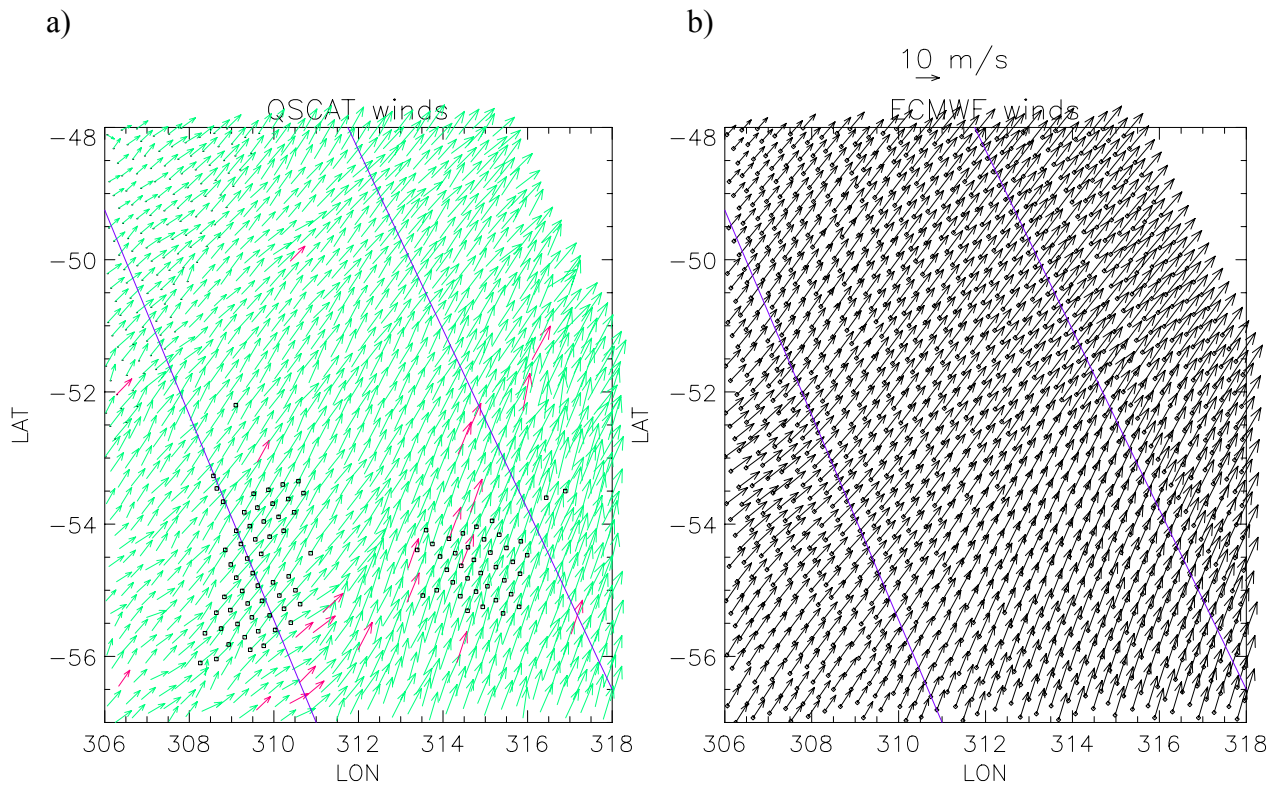
Figure 18 Same as Figure 16 but for different date (August 28 1999 at 10 hours UTC) and location. The violet lines separate the nadir (left side), the sweet-right (middle) and the outer-right (right side) regions.

Quality Control and Wind Retrieval for SeaWinds

3.2 Quality Control in BUFR[2]

As shown in Section 3.1, there is a potential positive impact of assimilating QuikSCAT winds into NWP models, such as ECMWF, after using our QC. Since March 2000, the QuikSCAT Near Real Time (NRT) BUFR product is available. As this product is the one used for assimilation purposes, we also want to set a QC for the BUFR product.

3.2.1 Data Repetition

First of all, we would like to make a few comments about a common problem in the QuikSCAT BUFR data. It appears that certain rows of data are repeated in the data stream. For a given row that repeats, the data values may be identical or different, depending on whether additional σ^o values are present in one of the row records or not. The row of lower quality is the one with fewer σ^o values. In all cases, the higher quality data is expected to be furthest from the edge of the data pass. A parameter called **time_to_edge**, which indicates the time difference to the nearest edge of the data pass, has been set in the product. Therefore, in order to avoid repetitions and keep the higher quality data, we first have to detect the repeated rows and then keep the one with the largest value of **time_to_edge** (*Leidner et al., 2000*).

The above procedure always requires reading the data an extra time and this may be computationally very inefficient when used in operational assimilation. In order to avoid this inefficiency problem, we have made an exhaustive analysis over a set of 6-hour QuikSCAT BUFR data files available at the ECMWF MARS archive. Here are the key points of this analysis :

   a) there is no more than one repetition;

   b) when a row is repeated, the one of highest quality can be either before or after the one of lower quality;

   c) there is 10% (approx) of repetitions per file;

   d) if we only look at WVC with 4 σ^o, there is only 1% of repetitions;

   e) the retrieved winds of repeated WVCs with 4 σ^o are almost identical.

Therefore, if we always keep WVCs with 4 σ^o and we reject repetitions when they occur (no matter if the repeated or second one is of higher quality as in this case the

winds are almost identical), the data files do not need to be read in advance as with the other procedure.

This procedure can only be used in the inner swath as in the outer swath we have a maximum of 2 σ^o per WVC. Since for now we are only interested in the inner swath (see Section 3.1.1) and the amount of WVCs which contain less than 4 σ^o and wind-derived information is only 1% of the total in this part of the swath, the procedure is not expected to distort the results in the QC.

Furthermore, we can apply the same concept in the outer swath but keeping WVC with 2 σ^o and rejecting repetitions and extend this method to any operational use of the BUFR data.

3.2.2 Differences with the QC procedure in HDF

As for HDF, the QC in BUFR is based on Rn. In order to compute and characterize Rn in BUFR, we have applied the same procedure than for HDF. However, a few differences were found which we think are important to report.

The expected MLE is also computed from 60 orbits of real data (BUFR in this case). From the mean MLE surface versus wind speed and node number, the noise is filtered using the same iterative process as for HDF. However, the MLEs rejected are three (or more) times higher than the mean MLE instead of two times as for HDF. This is done to keep consistency in the filtering procedure in terms of rejecting a small amount of data and conserving the shape of the original function (see discussion in section 3.1.1).

Figure 19a shows the filtered mean MLE versus wind speed and node number for BUFR. Comparing this surface with the one for HDF (Figure 8b), both are very similar although the BUFR surface looks more irregular for speeds higher than 7 m/s. These irregularities make the two-dimensional function fit (see Appendix B) to the BUFR surface less accurate. As said in section 3.1.1, the function fit is required for extrapolation purposes. Figure 19b shows the function fit (or expected MLE surface). It is clearly discernible that the irregularities seen in Figure 19a are filtered out in the fit, but the main shape of both surfaces remains the same and therefore the accuracy of the resulting Rn is not expected to decrease significantly.

Both surfaces in Figure 19 are for speeds lower than 20 m/s and for the inner nodes. The two-dimensional function fit is used in the same way as in HDF to extrapolate the expected MLE surface for winds higher than 20 m/s and the outer nodes.

Figure 20 shows the contour plot of a two-dimensional histogram of RMS-ECMWF against Rn for two weeks of BUFR data. As in Figure 11 (same plot but for HDF), the RMS-ECMWF increases as Rn increases, or in other words, the quality of data is decreasing with increasing Rn. From plots b), c) and d) we can also say that the RMS-ECMWF is increasing more rapidly with Rn at higher wind speeds. However, when comparing both Figures, it is clearly discernible that the RMS-ECMWF in HDF is

a)
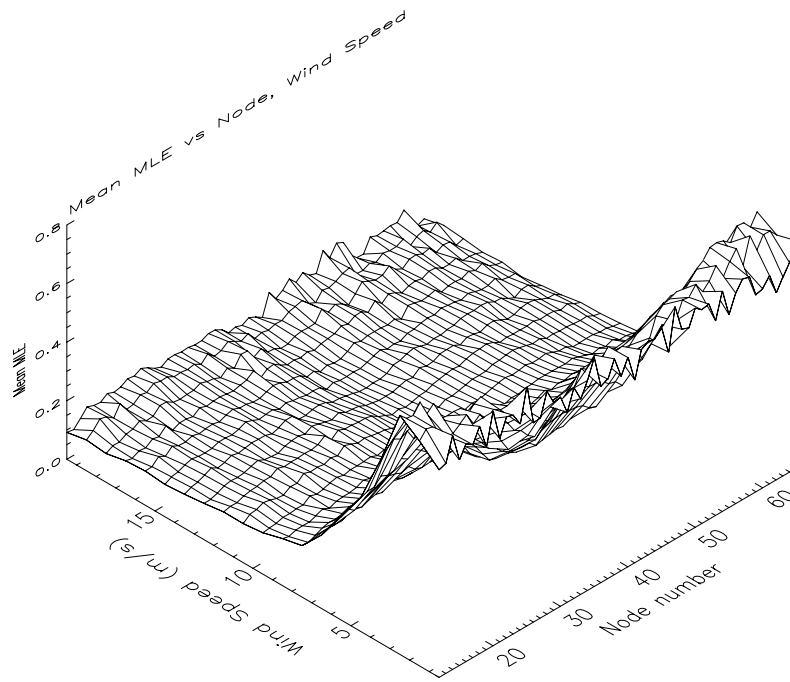
b)
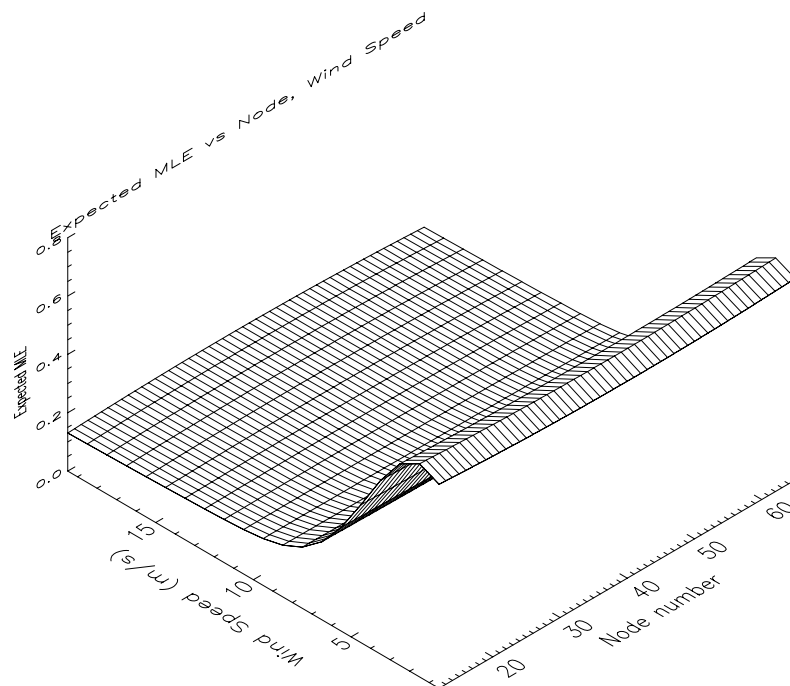
Figure 19 "Filtered" mean JPL-selected MLE (plot a) and Expected MLE versus wind speed and node number for the inner swath nodes. The speed binning is 1 m/s and the node binning is 1.

increasing more rapidly with respect to Rn for all wind speeds, suggesting a better behaviour of the HDF Rn as a quality control indicator.

Nevertheless, we have looked at the same plots as in Figures 12 and 13 but for BUFR (not shown) and they are very similar to HDF. Therefore, the rain rate is also proportionally increasing the retrieved wind speed and above 6 mm/hr produces undesirable "rainy" WVCs. Moreover, the same plot as in Figure 14 but for BUFR (not shown) is also very similar to HDF, suggesting that the optimal BUFR Rn threshold may be the same as that used for HDF.

Note that, as for HDF, we have tested different thresholds. The one which has given better results is the one used in HDF (see equation 3).
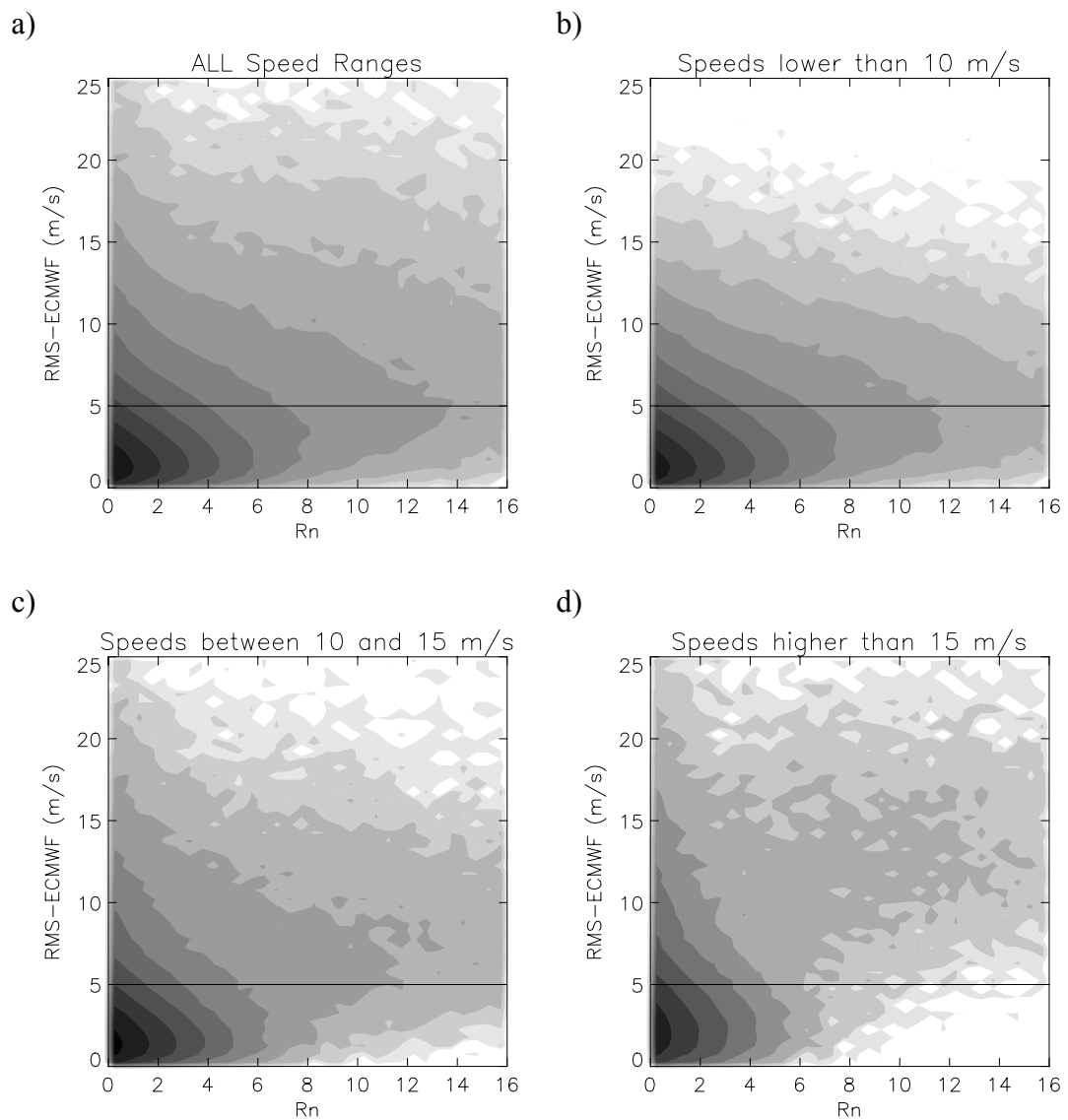
Figure 20 Same as Figure 11 but for BUFR data.

3.2.3 Threshold Validation

In the same way as in HDF (see section 3.1.4), we test the defined threshold against ECMWF and SSM/I collocations. The results for the sweet parts of the swath are shown in tables 7,8 and 9, and the results for the nadir parts are shown in tables 10, 11 and 12. Tables 7-12 are in the same format as tables 1-6 (see section 3.1.4) respectively.

In general, the results show that the BUFR QC works slightly worse than the HDF (see discussion on the Rn behaviour in the previous section).

Comparing table 7 to table 1, we note a larger percentage of rejections in BUFR than in HDF at all speeds. From tables 8 and 2, we see that this excess of rejections is mostly concentrated below the RMS value of 5 m/s, which in turn makes the mean RMS-ECMWF smaller. The mean RMS-ECMWF difference between accepted and rejected solutions is 4 m/s in HDF, while in BUFR is slightly lower than 3 m/s. Therefore, the excess of rejections in BUFR with respect to HDF (see tables 1 and 7) is mostly concentrated at low RMS-ECMWF values, which in turn makes the mean RMS-ECMWF smaller (4.92 m/s in BUFR, while 6.24 m/s in HDF). This indicates a better performance of the HDF QC with respect to the BUFR QC. Moreover, from tables 9 and 3, the amount of "rainy" WVCs rejected is slightly lower for BUFR, perhaps as a result of the slightly poorer performance.

Comparing the BUFR QC in the nadir (tables 10-12) with the HDF QC in the same region (tables 4-6), we can draw similar conclusions than for the sweet parts of the swath, except that in this case the total number of rejections in BUFR is comparable to HDF. The reason why the number of rejections in the nadir swath is not higher for BUFR is the fact that the <MLE> in BUFR is misfit towards higher values (compared to the filtered mean MLE values) in the nadir parts (see Figures 19a and 19b). This in turn decreases the value of Rn and therefore decreases the number of rejections.

In general, the BUFR QC works fine, although its performance is slightly worse than the HDF QC. This is due to the fact that the properties of the Rn as a quality control indicator are somehow smeared in BUFR compared to HDF, as it is further explained in the next section.

TABLE 7

	Total	V<10	10≤V≤15	V>15
Num. Points (n/a)	3005557	2261475	617140	126942
Accepted (%)	93.3	94.9	90.5	79.2
Rejected (%)	6.7	5.1	9.5	20.8

TABLE 8

	RMS<5	RMS>5	Mean RMS (m/s)
Total (n/a)	2805852	203084	2.26
Accepted (%)	95.5	63.8	2.07
Rejected (%)	4.5	36.2	4.92

TABLE 9

	RR=0	0<RR≤6	RR>6
Num. Points (n/a)	647292	56939	2904
Accepted (%)	95.3	72.7	16.1
Rejected (%)	4.7	27.3	83.9

TABLE 10

	Total	V<10	10≤V≤15	V>15
Num. Points (n/a)	1744647	1290254	372353	82040
Accepted (%)	93.9	95.9	90.3	79.1
Rejected (%)	6.1	4.1	9.7	20.9

TABLE 11

	RMS<5	RMS>5	Mean RMS (m/s)
Total (n/a)	1585453	160703	2.48
Accepted (%)	96.1	72.3	2.29
Rejected (%)	3.9	27.7	5.49

TABLE 12

	RR=0	0<RR≤6	RR>6
Num. Points (n/a)	360953	28150	1536
Accepted (%)	95.9	70.7	19.4
Rejected (%)	4.1	29.3	80.6

Note : RMS is refered as the vector RMS difference between JPL-retrieved winds and ECMWF winds in m/s; V is the JPL-retrieved wind speed in m/s; and RR is the SSM/I rain rate in mm/hr.

3.3 *MLE Characterization*[3]

In the previous section, we have shown that the BUFR Rn slightly differently behaves as a QC indicator compared to the HDF Rn, denoting differences between the Rn distributions of both formats. Since the Rn is just a normalized MLE, the Rn differences are expected to be seen in the MLE as well. Figure 21 shows the contour plot of the two-dimensional histogram of the BUFR MLE versus the HDF MLE. The plot shows only small correlation (around 0.5) between both MLE distributions. Moreover, the mean BUFR MLE value (0.28) is significantly smaller than the mean HDF value (0.57). It is clear from these results that, although the QC skill does not differ much between BUFR and HDF, the MLE distributions of both formats are significantly different. In order to better understand this, we perform a comprehensive characterization of the MLE.
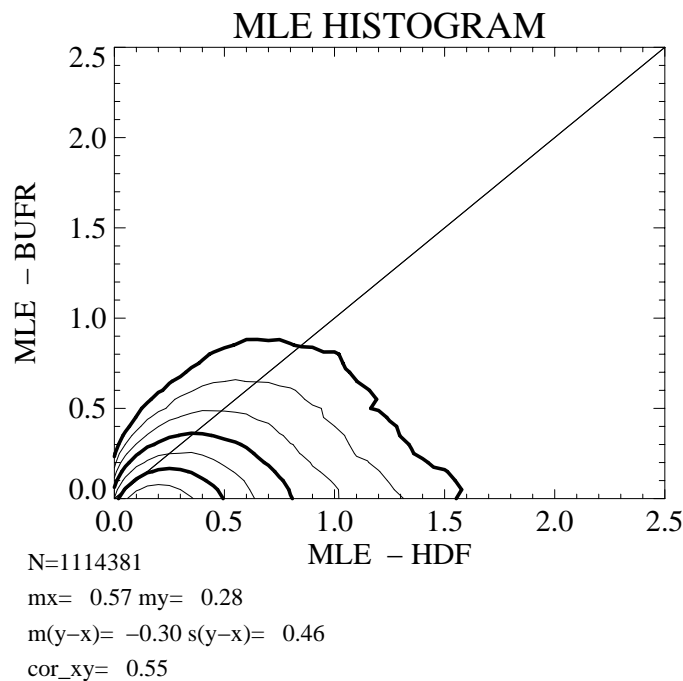
Figure 21 Contour plot of the two-dimensional histogram of the BUFR MLE versus the HDF MLE. N is the number of data; mx and my are the mean values along the x (HDF) and y (BUFR) axis, respectively; m(y-x) and s(y-x) are the bias and the standard deviation with respect to the diagonal, respectively; and cor_xy is the correlation value bween the HDF and the BUFR MLE distributions. The contour lines are in logarithmic scale (each step is 2 to the power of 1 and the lowest level corresponds to N/4000 data).

As discussed in section 2 and at the beginning of section 3, the BUFR σ^o is an average of the HDF σ^o per beam and the MLE a distance to the solution lying on the GMF,

---

[3] Based on the manuscript submitted to the *IEEE Transactions on Geoscience and Remote Sensing*, July 2001, IEEE.

more precisely a squared distance (see equation 1). From a theoretical point of view, the HDF and BUFR MLE distribution characteristics may differ just by using a different number of σ^o in their computation. In this section, we show this with a simple example. In order to validate the theoretical results, a simulation is performed to bridge the gap between theory and reality.

3.3.1 Theoretical case

This case corresponds to a simplified version of the MLE, which uses the following set of assumptions:

1) Typically for SeaWinds, HDF contain N>4 σ^o per WVC while BUFR contain M=4 σ^o per WVC in the inner swath. Therefore, the MLE is computed for HDF in a higher dimensional measurement space than for BUFR. In this example we simplify the problem assuming N=2 and M=1.

2) The truth or solution lies in the origin of our measurement space for simplicity.

3) Since in scatterometry the errors are considered Gaussian, we consider pairs of measurements (x,y) in the N(=2)-dimensional space as Gaussian distributed points around the origin (solution). Therefore, we use the following two-dimensional Gaussian PDF (Probability Density Function):

$$p(x,y)dxdy = \frac{1}{2\pi s^2} e^{-\frac{1}{2}\frac{(x^2+y^2)}{s^2}} dxdy, \tag{4}$$

where the standard deviation in both axis is assumed identical, i.e. $s = s_x = s_y$.

4) For simplicity, we also assume constant Kp noise values for both HDF and BUFR. As such, the MLE is equivalent to a squared distance to the origin weighted by a constant factor. Moreover, this assumption is important since it will allow us to show the significant change between the mentioned MLE distributions just by setting N>M.

Mathematical demonstration

In order to show the difference between two different distributions, we should use the following mathematical definitions:

- The mean or expected value of a function *f(x,y)* is defined in terms of the PDF *p(x,y)* by

$$E(f) = \int\limits_{-\infty}^{\infty}\int\limits_{-\infty}^{\infty} f(x,y) \cdot p(x,y) \cdot dx \cdot dy \tag{5}$$

- The standard deviation (SD) of a function $f(x,y)$ is defined in terms of the PDF $p(x,y)$ by

$$SD(f) = \sqrt{VAR(f)} = \sqrt{E(f^2) - (E(f))^2} \qquad (6)$$

where *VAR* is the variance.

- Finally, the correlation between two functions $f(x,y)$ and $g(x,y)$ is defined by

$$COR(fg) = \frac{(E(fg) - E(f) \cdot E(g))}{SD(f) \cdot SD(g)} \qquad (7)$$

Using the above assumptions, we can rewrite equation 1 as:

$$MLE_{nD} = \frac{1}{n} \cdot \frac{D_{nD}}{Kp_{nD}} \qquad (8)$$

where n is the number of dimensions (1 for BUFR and 2 for HDF), the subscript nD refers to each dimensional case, D_{nD} is the squared distance to the origin, and Kp_{nD} the constant Kp value.

Using the previous equations, we compute the MLE for both HDF and BUFR cases by setting the different terms of equation 8:

a) HDF ($n=2$)

Since the solution is at the origin, the squared distance for a measurement pair (x,y) in this case is:

$$D_{2D} = x^2 + y^2. \qquad (9)$$

The measurement noise is assumed fixed and according to the predefined PDF (equation 4) corresponds trivially to its variance and is identical in both x and y axis: s^2. However, this can easily be computed substituting equation 4 in 5, and 5 in 6:

$$Kp_{2D} = (SD(x))^2 = (SD(y))^2 = s^2 \qquad (10)$$

Substituting equations 9 and 10 in 8, the MLE is as follows:

$$MLE_{2D} = \frac{x^2 + y^2}{2s^2} \qquad (11)$$

b) BUFR ($n=1$)

In this case, the measurement is an average of the N measurements, $z = \left(\frac{x+y}{2}\right)$, with $z = 0$ as solution. Therefore, the squared distance is:

$$D_{1D} = z^2 = \frac{x^2 + y^2}{4} + \frac{x \cdot y}{2} . \tag{12}$$

The measurement noise is computed similar to the HDF Kp, using equations 4, 5 and 6:

$$Kp_{1D} = (SD(\frac{x+y}{2}))^2 = \frac{\sigma^2}{2} \tag{13}$$

Substituting equations 12 and 13 in 8, the MLE is as follows:

$$MLE_{1D} = \frac{x^2 + y^2}{2\sigma^2} + \frac{x \cdot y}{\sigma^2} \tag{14}$$

In order to show that the distributions of MLE_{1D} and MLE_{2D} (analogous to MLE in BUFR and HDF, respectively) differ, we compute their mean values, standard deviations and finally the correlation.

Substituting equations 4 and 14 in 5 and solving the latter, we get the mean value for MLE_{1D}:

$$E(MLE_{1D}) = 1 \tag{15}$$

Similarly, substituting equations 4 and 11 in 5, we get the mean value for MLE_{2D}:

$$E(MLE_{2D}) = 1 \tag{16}$$

Using equations 5, 6, 11, and 14, we get the following SD values for the MLE_{1D} and MLE_{2D} distributions:

$$SD(MLE_{1D}) = \sqrt{2} \tag{17}$$

$$SD(MLE_{2D}) = 1 \tag{18}$$

Solving equation 7, we get for the cross term of MLE_{1D} and MLE_{2D} distributions an expected value of

$$E(MLE_{1D}MLE_{2D}) = 2 . \tag{19}$$

Using the results of equations 15-19, we solve equation 7 and get the following correlation value between the HDF and BUFR MLE distributions:

$$COR(MLE_{1D}MLE_{2D}) = \frac{1}{\sqrt{2}} \tag{20}$$

The results show that reducing the number of dimensions from two to one in the observational space by averaging the observations, does not affect the mean MLE value (identical values in equations 15 and 16) but produces an increase in the SD of the MLE distribution (see equations 17 and 18). Moreover, there is a clear

---

decorrelation between the 2D and the 1D MLE distributions (correlation of 0.7 approx., from equation 20). Therefore, it is clear that the distributions differ.

In Figure 21, we directly compare the MLE distributions from the HDF and BUFR products for the entire set of 3 days of QuikSCAT HDF data collocated with the QuikSCAT BUFR data. The contour plot of the two-dimensional histogram of the BUFR MLE versus the HDF MLE shows indeed small correlation between both MLE distributions, as presented in the introduction. However, the results differ somewhat from the theoretical example. The correlation is smaller in the real case and the ratio between the mean values of HDF and BUFR distributions is 1 in the case of the theoretical example while 2 in the real case where the mean BUFR MLE value (0.28) substantially smaller than the mean HDF value (0.57). This can be expected, since the theoretical example is just a simplification of the problem as discussed above. In order to understand the real results in more detail, a simulation is needed.

3.3.2 MLE Simulation

In the simple example that we theoretically solve in Section 3.3.1, we show that the small correlation between HDF and BUFR MLE distributions is due to the σ^o averaging, assuming two measurements for HDF and one for BUFR. However, in the real case, where HDF contains more than four measurements and BUFR typically four, the results, although similar, present some differences with respect to the theoretical case. In particular, the correlation is significantly smaller (0.5) compared to theory (0.7).

In this section, we simulate HDF and BUFR MLEs, assuming a realistic number of measurements for both sets. First, the simulation is constrained to the most important assumptions used in the theoretical case to show that the theoretical demonstration can be extrapolated to the real case by using a larger number of σ^o in both HDF and BUFR products. Then, a more realistic simulation is compared to the real distribution. We also simulate the effects of varying the number of σ^o on the MLE distributions. Finally, since real and simulated MLE distributions present some differences, we perform a detailed analysis of the problem to better understand these differences.

3.3.2.1 Simulation procedure

We use the JPL selected winds of the BUFR files as truth to simulate two sets of measurements. The first set simulates the HDF product, using realistic noise values and number of measurements per beam (or flavor). Then, similar to the real data, these measurements are averaged per flavor to generate the second set which simulates the BUFR product. The more observations of a particular WVC that we simulate, the larger the measurement noise that we assume, such that the information content is the same in each simulated HDF and BUFR WVC. Once we have simulated

both sets of measurements, we invert them, using equation 1, to derive the simulated MLE.

Number of σ^o

In order to adequately simulate both products we have to use a realistic number of σ^o per WVC. In the case of the HDF simulation, we produce a variable number of measurements depending on the WVC number and beam.

Figure 22 shows the histogram of the number of measurements per WVC and beam for one day of HDF data. Plot a corresponds to WVC number 12 and plot b to WVC number 55. It is clearly discernible from the different distributions of plots a and b that the number of measurements in HDF varies from one WVC to another. Moreover, these distributions are broad, indicating that the number of measurements is considerably varying in each WVC as well. However, to simplify the simulation, we have chosen the number of σ^o corresponding to the peak of each distribution as the fixed value which will represent the number of σ^o for each particular WVC and beam.

As explained above, the BUFR measurements are produced by averaging the HDF measurements per beam. Therefore, the number of σ^o in BUFR will depend on the number of σ^o in HDF. Since we perform this simulation in the sweet parts of the swath, we use 4 σ^o per WVC for BUFR.
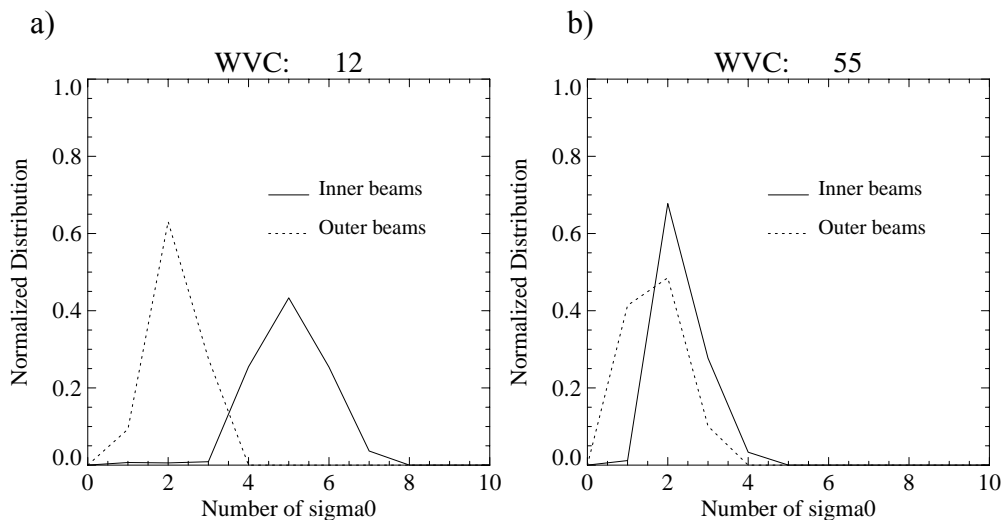

Figure 22 Normalized histogram of the number of sigma0 for WVC number 12 (plot a) and 55 (plot b). The solid line correspond to the inner swath beams (fore and aft) and the dotted line to the outer swath beams.

3.3.2.2 Simulation results

MLE closest to theory

We first use the simulation tool to extrapolate the theoretical case to a higher number of measurements and therefore check whether the theoretical assumptions used are valid or not to explain the real behavior of the MLE. We use the simulation procedure as defined in section 3.3.2.1 but including two additional constraints based on the assumptions 2 and 4 used in the theoretical case (see section 3.3.1):

- We consider only one truth (origin in the theoretical case), which in this case is an eastward wind of 7.8 m/s.

- We use fixed Kp values for both HDF and BUFR.

Since the assumption of Gaussian errors (assumption 3) is already used in the simulation procedure, the only assumption which is not used is the assumption of N=2 (two σ^o measurements in HDF) and M=1 (one σ^o measurement in BUFR). Instead, we are using N=8 and M=4 (typical number of measurements in the sweet parts of the swath). Therefore, the main difference between the theoretical case and this new simulation is the number of measurements and the dimension of the solution (in the simulation the solution is a surface, but in the theoretical case it is a point) used. In other words, this simulation corresponds to an extrapolation of the theoretical case to a higher dimensional order of the measurement space both for HDF and BUFR.

Figure 23 shows the same contour plot than Figure 21, but for this constrained simulation. The shape of the two-dimensional histogram slightly differs from the shape of real histogram (Figure 21). The ratio between HDF and BUFR mean values is around 1.6 and the individual means are smaller than one (Figure 23), which is different from the theoretical case where both HDF and BUFR mean values are identical and equal to one (see equations 15 and 16). In the theoretical case, the solution is a point in the multi-dimensional space. In the simulation (also for real data), the solution is a multi-dimensional folded surface with a strong non-linear behavior. This non-linearity may contribute to the change in the MLE properties when going from HDF to BUFR.

In general, the distributions differ somewhat from reality. This can be expected since the constraints of fixed Kp and truth have an effect on the MLE distributions. However, the correlation value is similar to reality (Figures 21 and 23). This result on the one hand, reinforces our suggestion of pointing to the σ^o averaging as the main cause for the low correlation between HDF and BUFR; on the other hand, confirms validity of the extrapolation of the results to a higher number of measurements.

MLE HISTOGRAM

N= 24927

mx= 0.76 my= 0.52

m(y−x)= −0.24 s(y−x)= 0.42

cor_xy= 0.54
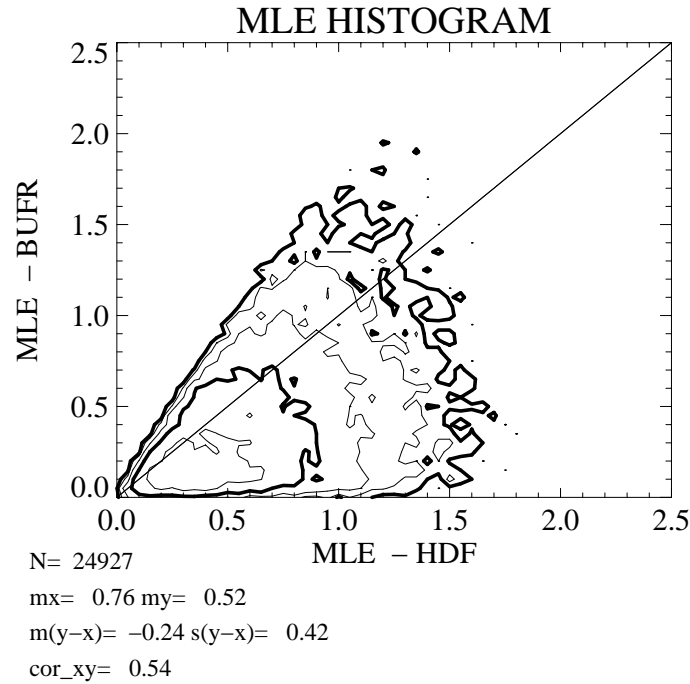
Figure 23 Same as Figure 21 but for the constrained simulation.

Realistic MLE

In order to provide a more realistic simulation, we do not use the assumptions of fixed Kp and truth as in the previous section, but use Kp and wind distributions as provided in the JPL product. We also use a more realistic number of measurements for HDF and BUFR (see discussion in section 3.3.2.1) than in the previous simulation.

Figure 24 shows the contour plot of the two-dimensional histogram of the simulated BUFR MLE versus the simulated HDF MLE. Although the distribution differs somewhat from the real case (Figure 21), it is clearly discernible that we have successfully reproduced the same small correlation (about 0.5 in both cases) by simply assuming a different number of measurements (more σ^o in HDF than BUFR). Moreover, the mean BUFR and HDF MLE values of the histograms are now more similar to the real ones (Figure 21) than in the previous simulation (Figure 23).

The remaining differences between the simulated and the real distributions can be explained by many issues. These differences are analyzed in detail in section 3.3.3. Nevertheless, it is clear from the results that the simulation is a good reflection of reality. Therefore, since averaging σ^o from HDF to BUFR is the main assumption of the realistic simulation, we conclude that this is the main cause of the low correlation of the MLE values (see Figure 21 or Figure 24). Moreover, we notice that the realistic and the constrained (previous section) simulated MLE distributions are quite similar (see Figures 23 and 24). This shows that the constrained assumptions have no significant effect on the low correlation of the MLE values as compared to the σ^o averaging (from HDF to BUFR). Therefore, this result validates the assumptions used in the theoretical example.

MLE HISTOGRAM

N=1105137

mx= 0.67 my= 0.45

m(y−x)= −0.22 s(y−x)= 0.39

cor_xy= 0.54
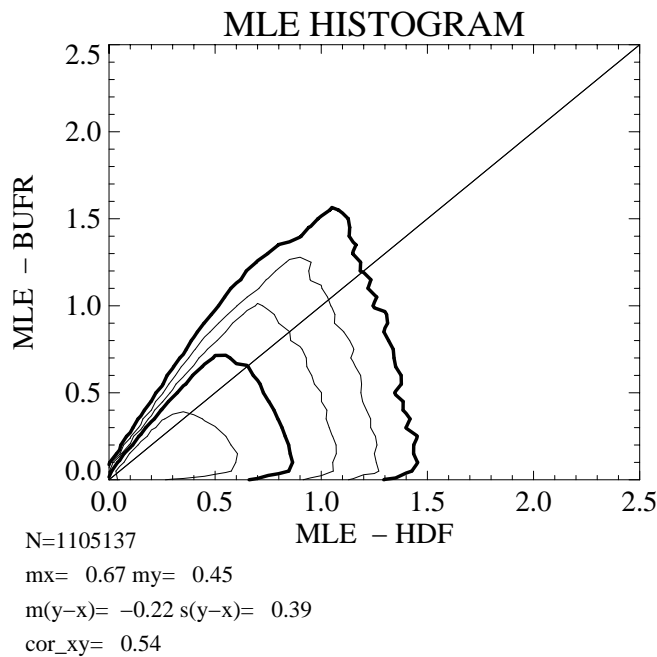
Figure 24 Same as Figure 21 but for the realistic simulation.

MLE distribution dependence on number of σ^o

Figure 25 is similar to Figure 24. We use the same simulation procedure but in this case we fix the number of σ^o used in the simulated HDF instead of using a realistic number. In the case of fixing the number of HDF measurements to 5 (plot a), one beam has two σ^o measurements and the rest of the beams have only one each. In the case of 6 σ^o measurements (plot b), two beams have two measurements each and two beams have only one each. Analogous explanation goes for the cases of 7 (plot c) and 8 (plot d) measurements. [Note that the different combinations of measurements / beams (e.g. in the case of 5 σ^o, you may use two measurements for the fore inner, the fore outer, the aft inner or the aft outer beam) do not affect the two-dimensional histograms (not shown)].

The plots in Figure 25 clearly show a decreasing correlation value with increasing number of HDF measurements (from 0.78 in plot a to 0.53 in plot d). Moreover, this effect is also seen in the shapes of the two-dimensional histograms, which are progressively smeared away from the diagonal. The correlation value of the theoretical case (0.7) is in between the correlation values of plots a (0.78) and b (0.66). This suggests that the decorrelation of the MLE when going from N=2 to M=1 is similar to the one from N=5 or 6 to M=4. The two-dimensional histogram in plot d is very similar to the one in Figure 24. Both histograms present as well similar correlation values. This is due to the fact that the realistic distribution of the number of σ^o measurements used for HDF in Figure 24 contains 8 σ^o measurements per WVC on average for the sweet parts of the swath. We can therefore interpret Figure 25 as a transition from the theoretical case to reality.

a)

MLE HISTOGRAM

N= 24927

mx= 0.54 my= 0.45

m(y−x)= −0.09 s(y−x)= 0.28

cor_xy= 0.78

b)

MLE HISTOGRAM

N= 24927

mx= 0.59 my= 0.44

m(y−x)= −0.15 s(y−x)= 0.34

cor_xy= 0.66

c)

MLE HISTOGRAM

N= 24927

mx= 0.63 my= 0.45

m(y−x)= −0.19 s(y−x)= 0.37

cor_xy= 0.60

d)

MLE HISTOGRAM

N= 24927

mx= 0.67 my= 0.44

m(y−x)= −0.22 s(y−x)= 0.39

cor_xy= 0.53
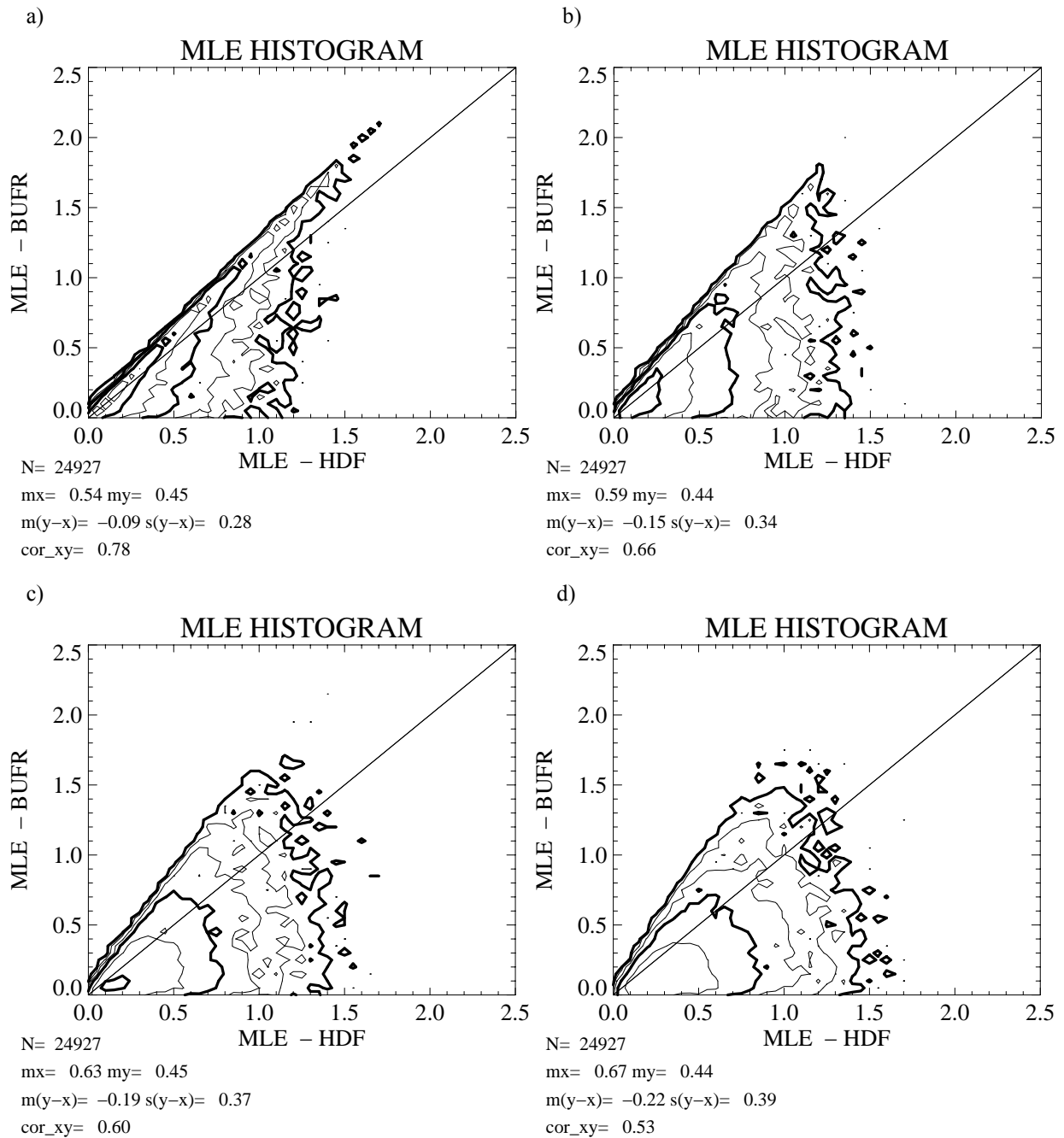
Figure 25 Same as Figure 24 but using a varying number of measurements in the HDF simulation: a) 5; b) 6; c) 7; and d) 8.

Figure 26 shows separately the distributions (one-dimensional histograms) of simulated BUFR and HDF MLEs. The different plots correspond to the different number of measurements simulated in HDF, in the same way as for Figure 25. As explained at the beginning of section 2, the BUFR simulated measurements are a flavor averaging of the HDF simulated measurements. Figure 26 clearly shows that the MLE distribution for simulated BUFR is invariant to the number of HDF measurements used prior to the BUFR averaging. This is an expected result since the number of BUFR simulated measurements per WVC is always assumed constant (4, one for each beam). However, the distribution of HDF MLE is significantly changing with the number of simulated HDF measurements, increasing its peak and mean value with increasing number of simulated measurements (see evolution from plots a to d).

Since the MLE value is a measure of the distance from the measurements to the GMF, this distribution change indicates that the more measurements (or the more dimensions in the measurement space) we use, the lower the probability to be close to the solution or GMF. As discussed in the first simulation, the dependence of the mean MLE value on the number of measurements is due to the non-linearities in the GMF.

a)

MLE HISTOGRAM

N= 24927
mh= 0.54 mb= 0.45
sh= 0.43 sb= 0.41

b)

MLE HISTOGRAM

N= 24927
mh= 0.59 mb= 0.44
sh= 0.42 sb= 0.41

c)

MLE HISTOGRAM

N= 24927
mh= 0.63 mb= 0.45
sh= 0.40 sb= 0.41

d)

MLE HISTOGRAM

N= 24927
mh= 0.67 mb= 0.44
sh= 0.39 sb= 0.41

Figure 26 One-dimensional histogram plots of the MLE distributions of Figure 25. mh and mb are the mean values of the HDF and BUFR distributions, respectively; sh and sb are the standard deviation values of the HDF and BUFR distributions, respectively.
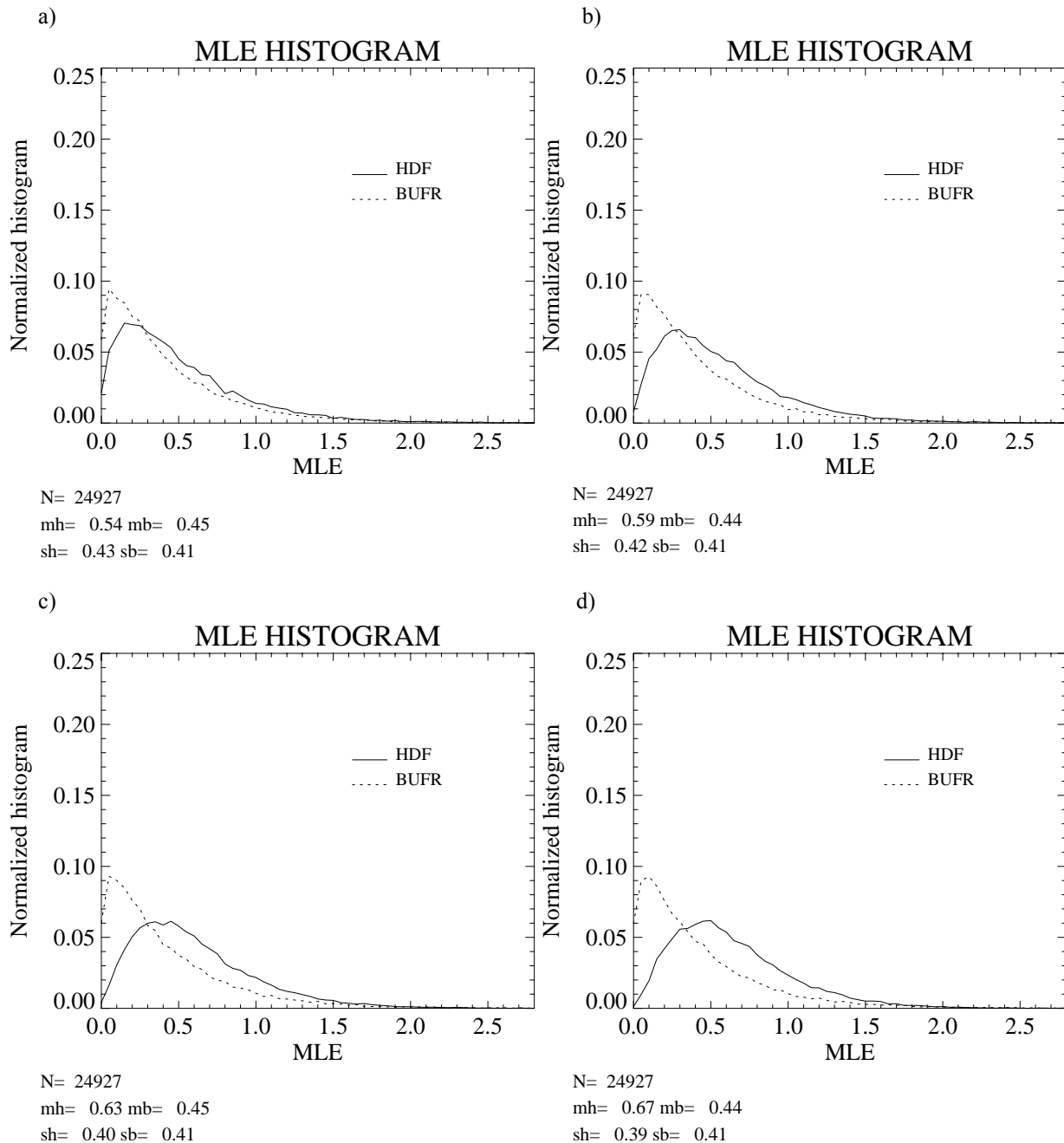
The decorrelation between HDF and BUFR MLE is explained by the change in the distribution characteristics of the latter. Although the non-linear behavior of the GMF

is affecting the MLE distributions, it is clear from the simulation results that the decorrelation is mainly due to a much smaller number of σ^o used in the inversion for BUFR compared to HDF (about half, since typically BUFR contains 4 and HDF 8 measurements).

In section 3.3.1, we demonstrate the change in the MLE distribution characteristics when averaging from a two-dimensional measurement space to a one-dimensional one. With this simulation we are able to better characterize the evolution of the MLE distributions when encountering higher dimensional measurement spaces.

3.3.3   Detailed analysis of MLE differences: real versus simulated

In sections 3.3.1 and 3.3.2, we clearly show the change in the MLE distribution characteristics when averaging the σ^o information (from HDF to BUFR), which leads to a small correlation of the HDF and BUFR MLEs. However, some differences are discernible in the simulated MLE distributions compared to the real MLEs. In this section, we perform a deeper analysis of these differences.

Distributions

Figure 27 is similar to Figure 26, but for real (plot a) and (realistic) simulated (plot b) data. It is clearly discernible the different shape of the simulated HDF and BUFR distributions compared to the real distributions. In particular, the mean value of the BUFR distributions is larger for the simulated MLE than for the real MLE. Moreover, the SD value of the HDF distributions is significantly larger for the real compared with the simulated MLE. We also note that in the HDF real data there is a larger accumulation of values in the vicinity of zero MLE.

MLE HISTOGRAM

N=1114381

mh= 0.57 mb= 0.28

sh= 0.53 sb= 0.40

MLE HISTOGRAM

N=1105137

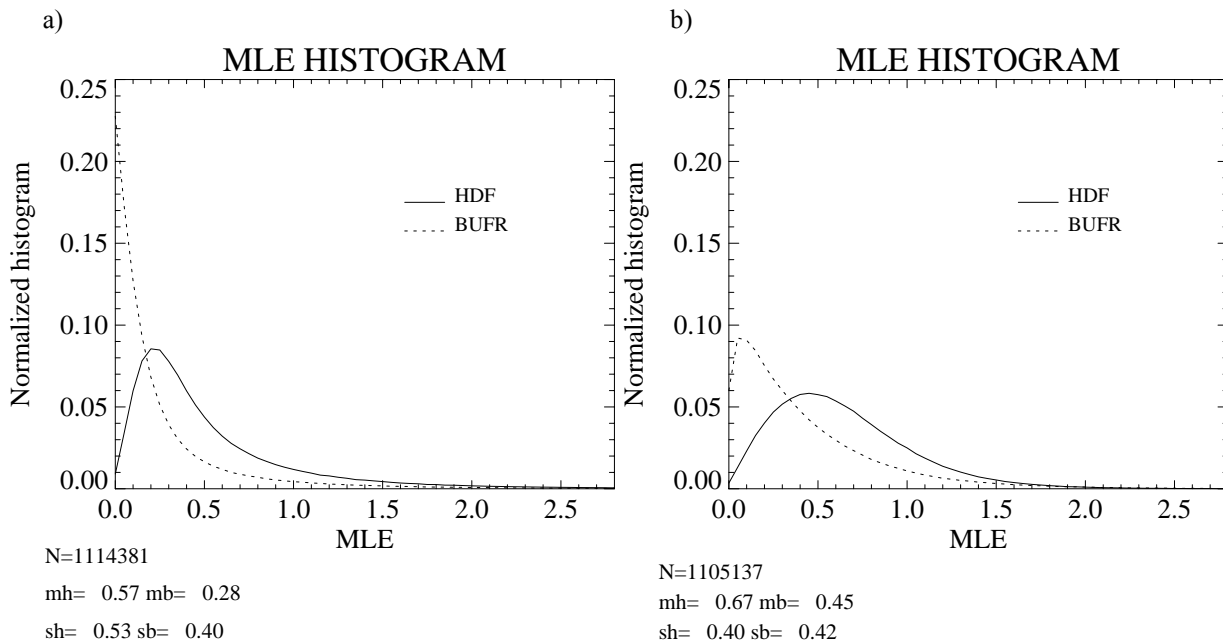mh= 0.67 mb= 0.45

sh= 0.40 sb= 0.42

Figure 27 One-dimensional histogram plots of the HDF and BUFR MLE distributions for real data (a) and the realistic simulation (b). The legend is the same as in Figure 26.

Mean values versus node number and wind speed

In order to better understand these differences in the MLE distributions, we study the behavior of the mean simulated and real MLE as a function of wind speed and cross-track location.

Figure 28 shows the mean MLE surface as a function of wind speed and WVC number for the HDF (plot a) and BUFR (plot b) real data (same surfaces as Figures 8b and 19a, respectively, but for the 1st rank instead of the selected MLE). The noise in the MLE surfaces, caused by geophysical effects (such as rain) and/or small amount of data (at high winds), is filtered out. The MLEs used in this Figure correspond to the MLEs of the 1st rank solutions provided in both QuikSCAT data products (HDF and BUFR). Figures 29a and 29b show the same surfaces as Figures 28a and 28b, respectively, but for simulated data. The MLEs used in this Figure correspond to the MLEs of the 1st rank solutions provided by our inversion software.

In HDF, there is a slight increase of the surface with increasing distance to nadir (Figures 28a and 29a). The increase is stepwise in the simulated data (Figure 29a) and not monotonic as for real data (Figure 28a) because of the approximation in the number of σ^o made in the simulation of HDF data. The reason for this increase lies in the inversion. As the inversion is a non-linear process, the scaling (linear correction) is not sufficient to compensate for the increase in the MLE due to the increase in the number of σ^o. Nevertheless, the mean MLE surfaces show that this effect is minor.

a)
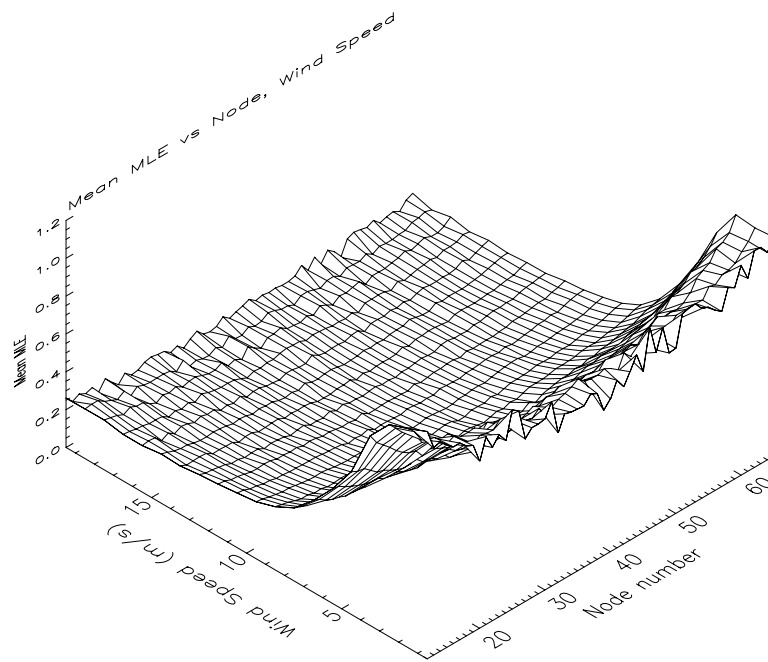
b)

Figure 28 Mean 1ˢᵗ-rank MLE versus wind speed and node number (only inner swath nodes are shown) for HDF (a) and BUFR (b) real data. The speed binning is 1 m/s and the node binning is 1.

Quality Control and Wind Retrieval for SeaWinds

a)

b)

Figure 29 Same as Figure 28 but for HDF (a) and BUFR (b) simulated data..
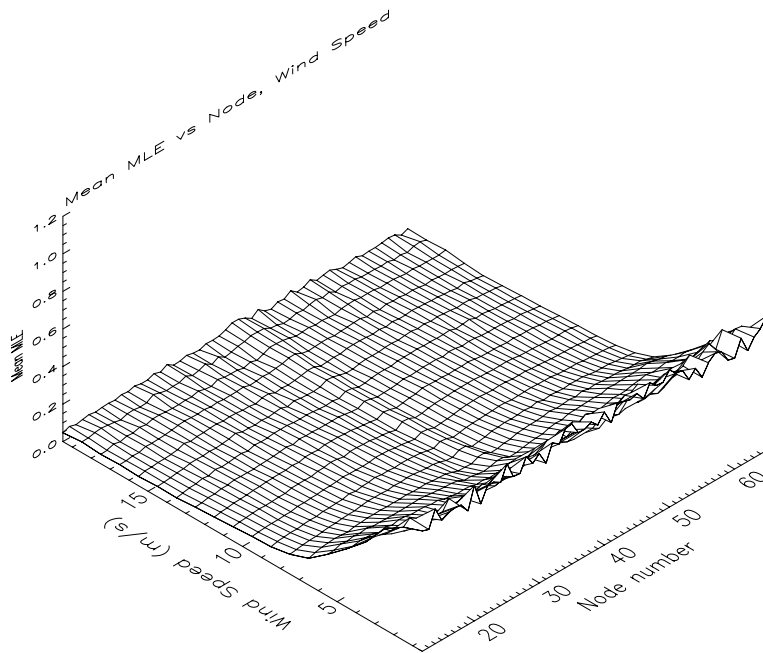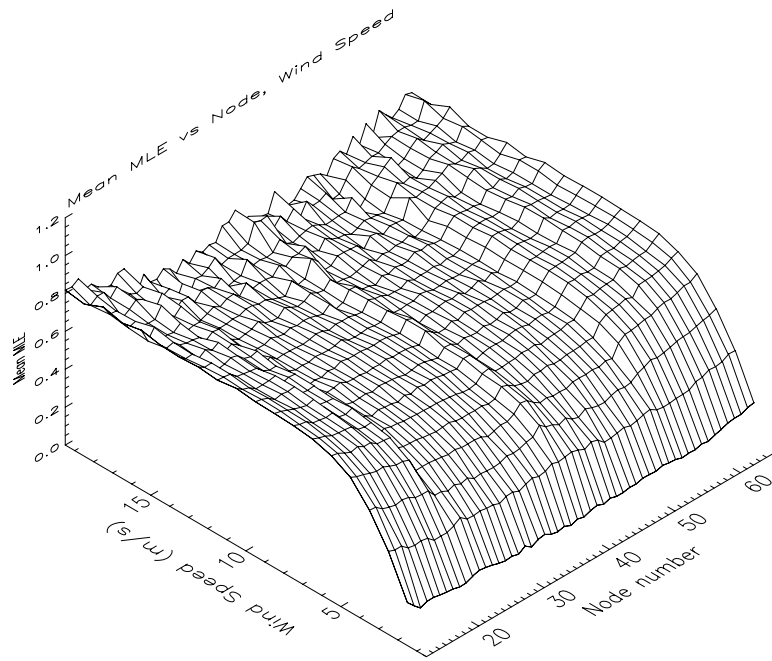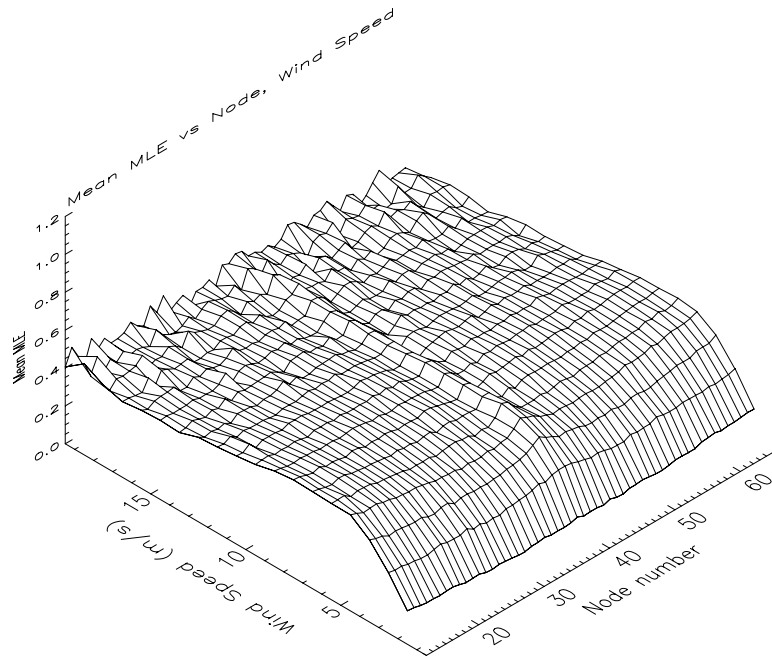
In BUFR, there is no increase in MLE with increasing distance to nadir (Figures 28b and 29b), as the number of σ^o is kept constant for all WVCs. As for the HDF case, the simulated MLE behaviour across track (Figure 29b) compares well with the real case in BUFR (Figure 28b).

If we compare the mean MLE behaviour as a function of wind speed between the real (Figure 28) and the simulated (Figure 29) cases, we see a large discrepancy at low speeds. In reality, the MLE increases with decreasing speed while in the simulated case the MLE decreases with decreasing speed.

The reason for this MLE increase in the real case is that the observation error (Kp) is underestimated for low wind speeds. From equation 1, an underestimation in the Kp (denominator term) will in turn produce an increase in the MLE. The Kp noise contains two terms: the instrument noise and the geophysical noise. *Figa and Stoffelen* (2000) provide a physically-based model for the NSCAT backscatter observation error. They find that for low wind speed, the largest uncertainty lies in the spatial variability of the geophysical target (geophysical noise). Since the different beam and polarization measurements in a WVC do not sample exactly the same area, the geophysical collocation error variability becomes substantial at low backscatter levels.

However, in the simulated case, the Kp is considered as a true value and therefore we would expect no increase or decrease in the MLE value at low wind speeds. This is however not the case. The problem lies in the inversion and a.o. in the fact that we assume that the measurement noise is proportional to the true value. The latter leads to a Kp which is proportional to σ_s^o (simulated σ^o from the GMF) in the denominator of equation 1. *Stoffelen* (1998) explains on page III-29 how proportional errors cause positive bias in the solution (after inversion). This positive bias will in turn produce a decrease in the MLE. Figure 30 illustrates the problem in the case of a two-beam measurement system (QuikSCAT has four beams, but for simplicity we draw a 2D case). The solid curves represent the solution space. The diamond represents the pair of "true" measurements, which are the starting point in the simulation process. The solid circle around the diamond represents the "true" measurement noise (Kp_t). Using this Kp_t we simulate the measurement pair (triangle inside the solid circle). The dashed circle represents its corresponding estimated noise (Kp_m). After inversion, we get a positively biased solution (star) which has its proportional noise (Kp_s) represented by the dotted circle. As Kp_s increases significantly, the MLE decreases (Kp_s is the denominator of equation 1) and this effect is more acute as we approach the origin corresponding to lower speeds.

Finally, it is clearly discernible that the mean MLE at mid and high speeds is significantly larger for simulated data compared to real data (see the surface plateau level of Figure 29 compared to Figure 28). This means that there is an overestimation of the Kp (or measurement) noise at these speed regimes. Since the largest uncertainty at these speeds lies in the instrument noise and not in the geophysical noise, we conclude that there is probably an overestimation of the instrument noise.
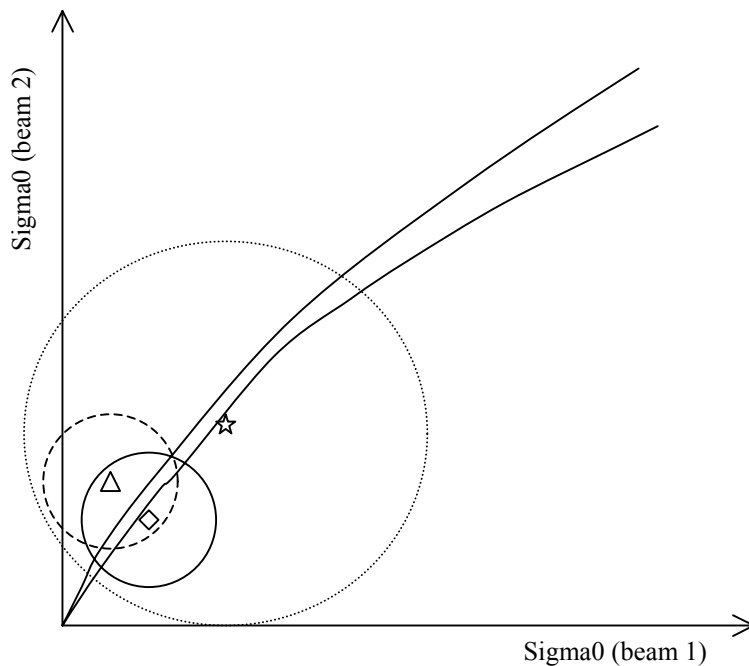
Figure 30 schematic illustration of the problem in a 2D measurement space

Main differences

According to the analysis, we conclude that the remaining differences between the simulated and the real distributions can be attributed to the following:

- The simulation of the number of σ^o per WVC and beam in HDF is just a rough approximation. In the real data a WVC can contain a variable number of σ^o (see Figure 22) and in the simulation we have fixed this number.

- The different behaviour of the real and simulated MLEs at low speeds as discussed above (see Figures 28 and 29). In the real data, the estimated Kp values, and more specifically the geophysical noise values, are underestimated.

  - An overall overestimation in the real data of the estimated Kp values (except at low winds where the opposite occurs), more specifically, the instrument noise values. This is deduced from the higher mean MLE values of both HDF and BUFR simulated distributions (Figure 29) compared to the mean values of the real distributions (Figure 28).

There may be other reasons that could cause minor differences in the distributions, such as processing of eggs or composites, i.e., for real data HDF uses eggs and BUFR

composites (see section 2), whereas for simulated data we treated both HDF and BUFR as composites. Nevertheless and as discussed in the previous section, these differences are not so relevant as the simulation is a good reflection of reality.

3.3.4 MLE influence on wind retrieval

In the previous sections, we have shown how different the MLE distributions are in HDF and BUFR. In the BUFR product, σ^o measurements are combined to result in only 4 independent σ^o observations. In HDF on average 8 σ^o measurements are available per WVC in the sweet swath. This data reduction could cause information in the σ^o measurements to be lost. As such, the poor BUFR and HDF MLE comparison should be taken seriously. As discussed in previous sections, the MLE is the residual parameter output from wind retrieval and is very important for Quality Control. However, as seen in section 3.2, the QC skill in BUFR is similar, although slightly worse, to the QC in HDF. In this section, we investigate in some detail the wind retrieval performance properties of SeaWinds BUFR as compared to HDF

Figure 31 shows the two-dimensional histograms of BUFR winds versus HDF winds (upper plots), BUFR versus ECMWF (mid plots) and HDF versus ECMWF (bottom plots). The left plots correspond to the histograms of wind speeds and the right plots to the histograms of wind directions. Both BUFR and HDF retrieved winds correspond to the 1st rank solution.

From the upper plots it is discernible that the BUFR and HDF retrieved winds are not identical, although very similar. Plot a) shows almost no bias in speed and a very small SD (0.58 m/s). Plot b shows a typical effect of comparing 1st rank solutions, which is the secondary distribution around 180°. This is due to the fact that 1st and 2nd rank solutions (often with very similar wind speed but wind direction 180°apart) can have very similar MLE values and therefore be switched from one data product to the other. This effect is leading to very high SD values. Still, we can see from the correlation factor (0.87) that the retrieved directions are similar.

Looking at the mid and the bottom plots, we can see almost no difference between HDF and BUFR when compared to ECMWF winds. Plots c) and e) show almost identical wind speed distributions with almost the same bias and SD. Plots d) and f) show very similar wind direction distributions with almost the same correlation factor.

Therefore, we conclude that the difference in the MLE distributions is not affecting the quality of the retrieved winds.

a)

WINDS HISTOGRAM

N=1114381
mx= 7.87 my= 7.89
m(y-x)= 0.02 s(y-x)= 0.58
cor_xy= 0.99

b)

WINDS HISTOGRAM

N= 962552
mx= 196.92 my= 196.76
m(y-x)= -0.16 s(y-x)= 51.54
cor_xy= 0.87

c)

WINDS HISTOGRAM

N=1060810
mx= 7.59 my= 7.85
m(y-x)= 0.26 s(y-x)= 1.90
cor_xy= 0.86

d)

WINDS HISTOGRAM

N= 856586
mx= 196.51 my= 197.07
m(y-x)= 0.56 s(y-x)= 57.30
cor_xy= 0.85

e)

WINDS HISTOGRAM

N=1058882
mx= 7.60 my= 7.85
m(y-x)= 0.25 s(y-x)= 1.89
cor_xy= 0.86

f)

WINDS HISTOGRAM

N= 858657
mx= 197.22 my= 197.87
m(y-x)= 0.65 s(y-x)= 58.67
cor_xy= 0.84

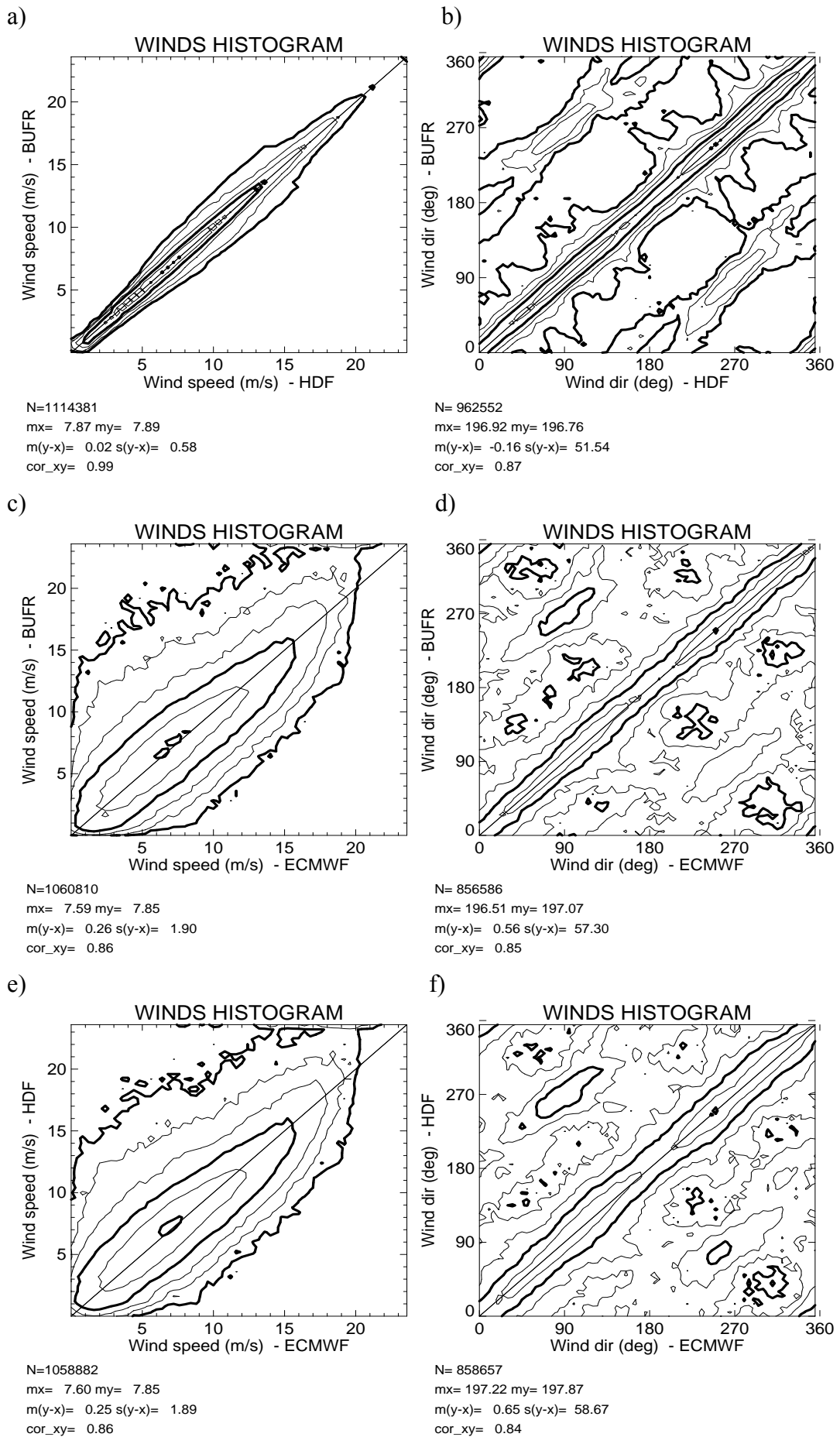*Figure 31 Two-dimensional histogram of BUFR winds versus HDF winds (plots a and b),BUFR winds versus ECMWF winds (plots c and d) and HDF winds versus ECMWF winds (plots e and f). The left plots correspond to wind speeds (bins of 0.4 m/s) and the right plots to wind directions (bins of 2.5°). Only ECMWF winds over 4 m/s are used in the wind direction plots. The legend and contour lines are the same as in Figure 21.*

3.4   KNMI Quality Control versus JPL Rain Flag[4]

In the presence of extreme weather events, the likelihood of rain is relatively high and QC of SeaWinds particularly important, according to the KNMI experience with near-real time (NRT) processing of SeaWinds data (http://www.knmi.nl/scatterometer). Although the KNMI QC is effective in rejecting rain-contaminated data, additional information on rain may be needed. In this respect, since May 2000, the SeaWinds data products, including the NRT data distributed by the National Oceanic and Atmospheric Administration (NOAA), have a rain flag (*JPL*, 2001). Since both the KNMI QC and the JPL rain flag are used in NRT processing, it is useful to compare them in order to improve the quality control for SeaWinds. In this section, we test the JPL rain flag against our QC.

3.4.1   Quality Control with new GMF

Also since May 2000, JPL wind retrievals have been produced using a new GMF called QSCAT-1. In order to perform a consistent comparison with the JPL rain flag (set simultaneouly to QSCAT-1 GMF), we want to use the new data. QSCAT-1 is the first empirically derived GMF from QuikSCAT measurements (*Freilich et al., 2002*), since the one used up to now, NSCAT-2, was derived from NSCAT data (*Wentz et al., 1999*). If we invert winds using a different GMF, we will get different MLE values. Although these differences are not expected to be significant, it may well be that Quality Control is affected and therefore it needs to be revised.

Assuming no major changes, we first compute the Rn using the new QSCAT-1 GMF MLE data and the existing <MLE> surface (computed from NSCAT-2 GMF data). The test is performed for two weeks of QuikSCAT HDF data.

Rn Characterization

As in the previous sections, we have collocated QuikSCAT data with ECMWF winds and SSM/I rain data and looked at the same kind of plots as in Figures 11 to 14 in order to characterize and validate Rn. The plots show very similar features as in section 3.1.3. The only difference is a slight increase in the Rn values.

Figure 32 shows the contour plot of a two-dimensional histogram of RMS-ECMWF against Rn. As in Figure 11 (same plot but for the NSCAT-2 GMF), the RMS-ECMWF increases (quality of data decreases) as Rn increases and the RMS-ECMWF

---

[4] Based on: Portabella, M., and Stoffelen, A., "A Comparison of KNMI Quality Control and JPL Rain Flag for SeaWinds," *Can. Jour. of Rem. Sens.* (special issue on Remote Sensing of Marine Winds), Vol. 28, No. 3, 2002, © Canadian Meteorological Society.

a)

b)

c)

d)
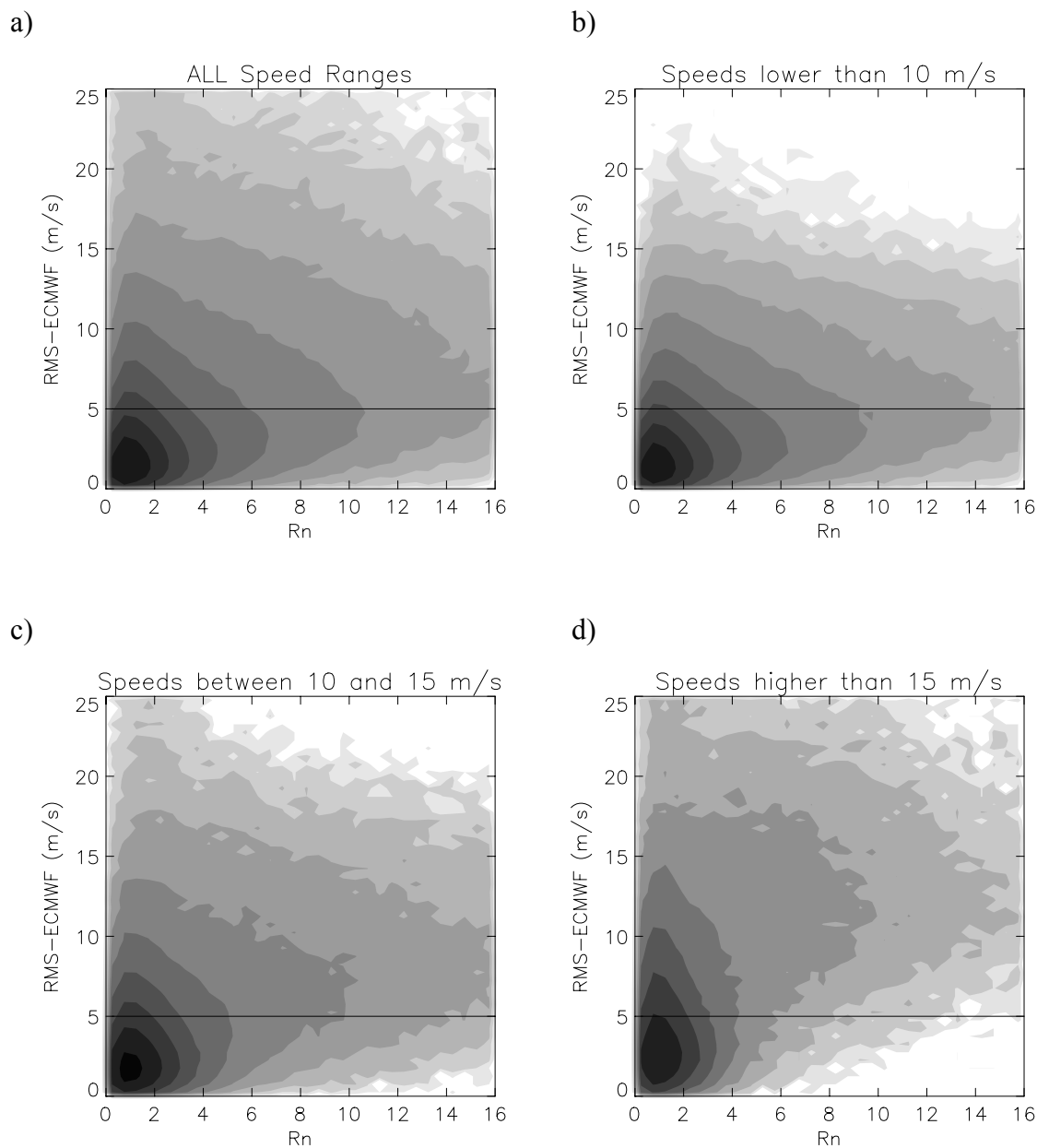
Figure 32 Same as Figure 11 but for the QSCAT-1 GMF.

is increasing more rapidly with Rn at higher wind speeds (see plots b, c and d). However, when comparing both Figures, it is discernible that the distributions (see contour lines) in Figure 32 are slightly shifted towards higher Rn values compared to Figure 11. The shift is more significant at mid and high wind speeds (see plots c and d in both Figures).

As we have used the same <MLE> surface to compute the Rn, this shift means that in general MLE values coming out from the inversion are slightly higher using the QSCAT-1 GMF than using the NSCAT-2 GMF. This is an indication that the NSCAT-2 GMF better fits the backscatter measurements than the QSCAT-1 GMF.

Therefore, if we keep the same Rn threshold as in Section 3.1, we would expect to have more rejections in this case.

Threshold Validation

We test the same Rn threshold as defined in section 3.1.4 against ECMWF and SSM/I collocations. The results for the sweet parts of the swath are shown in tables 13, 14 and 15, and the results for the nadir part are shown in tables 16, 17 and 18. Tables 13-18 are in the same format as tables 1-6 (see section 3.1.4) respectively.

Comparing table 13 to table 1, we appreciate a larger percentage of rejections in the former at all speeds, and more in particular at mid and high winds. From tables 14 and 2, we see a considerable amount of this excess of rejections concentrated below the RMS value of 5 m/s, which in turn makes the mean RMS-ECMWF slightly smaller. The mean RMS-ECMWF difference between accepted and rejected solutions is slightly smaller in table 14 (3.6 m/s) compared to table 2 (4 m/s). This indicates a somewhat better performance of the HDF QC using the NSCAT-2 GMF. However, this excess in rejections is positively contributing to rain detection. From tables 15 and 3, the amount of "rainy" WVCs rejected is higher in the former, especially at rain rates below 6 mm/hr where there is 9.7% more of rejections.

Comparing the HDF QC using the QSCAT-1 GMF in the nadir (tables 16-18) with the HDF QC using the NSCAT-2 GMF (tables 4-6), we can draw the same conclusions than for the sweet parts of the swath. In terms of quantitative results, the only significant differences with respect to the sweet parts are the following: the excess of rejections is 1.6 % in total (see tables 4 and 16) while in the sweet parts is 1.4% (see tables 1and 13); and the excess of rejections for rain rates below 6 mm/hr is 6.6% (see tables 6 and 18) compared to the 9.7% in the sweet parts (see tables 3 and 15).

In general, the results show that with the QSCAT-1 GMF the QC rejects more data than with the NSCAT-2 GMF. However, this gives a positive impact on rain detection, especially for rain rates below 6 mm/hr. Therefore, we believe that using the same QC procedure (i.e. same <MLE> surface and Rn threshold) as in Section 3.1 for the new GMF (QSCAT-1) is appropriate and there is no need to tune the QC procedure to the new data.

TABLE 13

	Total	V<10	10≤V≤15	V>15
Num. Points (n/a)	5170647	3922963	982175	265509
Accepted (%)	93.0	95.2	88.9	77.1
Rejected (%)	7.0	4.8	11.1	22.9

TABLE 14

	RMS<5	RMS>5	Mean RMS (m/s)
Total (n/a)	4726341	444378	2.49
Accepted (%)	95.9	62.1	2.24
Rejected (%)	4.1	37.9	5.83

TABLE 15

	RR=0	0<RR≤6	RR>6
Num. Points (n/a)	1188320	89416	4742
Accepted (%)	95.7	60.9	9.0
Rejected (%)	4.3	39.1	91.0

TABLE 16

	Total	V<10	10≤V≤15	V>15
Num. Points (n/a)	3006927	2295287	555318	156322
Accepted (%)	92.1	95.0	85.9	71.1
Rejected (%)	7.9	5.0	14.1	28.9

TABLE 17

	RMS<5	RMS>5	Mean RMS (m/s)
Total (n/a)	2634399	372757	2.85
Accepted (%)	95.5	68.0	2.56
Rejected (%)	4.5	32.0	6.23

TABLE 18

	RR=0	0<RR≤6	RR>6
Num. Points (n/a)	670388	48638	3370
Accepted (%)	95.0	57.9	12.9
Rejected (%)	5.0	42.1	87.1

Note : RMS is referred as the vector RMS difference between JPL-retrieved winds and ECMWF winds in m/s; V is the JPL-retrieved wind speed in m/s; and RR is the SSM/I rain rate in mm/hr.

3.4.2 JPL Rain Flag Description

In January 2000, JPL incorporated in the QuikSCAT products two different rain flags based the mp_rain_probability and the nof_rain_index respectively. However, since May 2000, JPL merged both techniques into a single rain flag. This rain flag procedure is actually based on the mp_rain_probability and called the MUDH (Multidimensional Histogram) rain algorithm (*Huddleston and Stiles, 2000*). The nof_rain_index (*Mears et al., 2000*) is incorporated as an additional parameter in the MUDH rain algorithm, but it is currently not being used (zero weight is assigned to this parameter) in the computation of the rain flag (*JPL, 2001*).

Briefly, mp_rain_probability is the probability of encountering a columnar rain rate that is greater than 2km*mm/hr. This probability value is read directly from a table based on several input parameters including average brightness temperature (both H-pol and V-pol), normalized beam difference, wind speed, wind direction relative to along track, and a normalized MLE. The space spanned by these parameters can detect whether the set of σ^o used in wind retrieval contain a noteworthy component created by some physical phenomenon other than wind over the ocean's surface, assuming that the most likely phenomenon is rain.

The final rain flag deduced from the MUDH rain algorithm is also incorporated in the QuikSCAT products and can be found in the wvc_quality_flag variable.

3.4.3 Comparison

The JPL rain flag separates "rain" (rain rate above 2km*mm/hr) from "no rain" (rain rate below 2km*mm/hr) cases and the KNMI QC separates cases of low quality to be rejected (above Rn threshold) from those of good quality to be accepted (below Rn threshold).

Both the JPL rain flag and the KNMI QC are meant to separate the usable data from the non-usable data. Therefore, the user should use only "no rain" data according to JPL rain flag and reject the "rain" data. In the same way, the user should accept or reject data according to KNMI QC, and therefore a study of the difference in behaviour of both procedures is of interest.

In order to make a consistent comparison, we have processed two weeks of HDF data and classified the results in four different categories: A) "JPL Rain Flag - No Rain" and "KNMI QC - Accepted"; B) "JPL Rain Flag - Rain" and "KNMI QC - Accepted"; C) "JPL Rain Flag - No Rain" and "KNMI QC - Rejected"; and D) "JPL Rain Flag - Rain" and "KNMI QC - Rejected". In line with the previous paragraph, categories A and D show similarities and categories B and C show discrepancies between the two procedures.

In tables 19-21 we present the results of collocating 2 weeks of QuikSCAT HDF data (sweet parts of the swath only) with ECMWF winds and SSM/I rain data. [Note: we have performed the same comparison in the nadir swath and got similar results]. In total, there are about 5.2 million collocations with ECMWF and 1.1 million collocations with SSM/I. We refer to rain data when SSM/I surface rain rate (RR) value is above 2 mm/hr, and to rain-free data when SSM/I surface rain rate value is below 2 mm/hr.

Table 19 shows by category the percentage of total data, the QuikSCAT mean speed, the ECMWF mean speed, the mean bias (QuikSCAT-ECMWF), the mean RMS-ECMWF, the percentage of data with rain (RR>2 mm/hr), and the percentage of all rain points (RR>2 mm/hr).

Results in table 19 show a very good agreement between both procedures as 94% of the data corresponds to categories A and D (91.1% in A and 2.9% in D). Moreover, category A shows good quality (0.5 m/s bias and 2.2 m/s RMS) rain-free (only 0.1% of data a rain contaminated) data while category D shows very low quality (5.1 m/s bias and 8.2 m/s RMS) and rain-contaminated (31.9% of data are rain contaminated) data.

Categories B and C contain 6% of the data and correspond to the differences in behaviour of both procedures.

Comparing both categories in terms of SSM/I rain detection, category B contains 13.9% of all the rain data while category C is only containing 2.4%. Therefore, JPL rain flag is more efficient as rain detector since only 7.6% (5.2% in A and 2.4% in C) of all rain data is not rejected, while the KNMI QC is accepting 19.1% (5.2% in A and

TABLE 19

	JPL Rain Flag No Rain		JPL Rain Flag Rain	
KNMI QC Accepted	Number of data (%):	91.1	Number of data (%):	2.0
	QuikSCAT Mean Speed (m/s):	7.6	QuikSCAT Mean Speed (m/s):	14.2
	ECMWF Mean Speed (m/s):	7.1	ECMWF Mean Speed (m/s):	11.8
	Bias-ECMWF (m/s):	0.5	Bias-ECMWF (m/s):	2.4
	RMS-ECMWF (m/s):	2.2	RMS-ECMWF (m/s):	4.8
	Rain > 2 mm/hr (%[1]):	0.1	Rain > 2 mm/hr (%[1]):	13.6
	Rain > 2 mm/hr (%[2]):	5.2	Rain > 2 mm/hr (%[2]):	13.9
KNMI QC Rejected	Number of data (%):	4.0	Number of data (%):	2.9
	QuikSCAT Mean Speed (m/s):	9.1	QuikSCAT Mean Speed (m/s):	12.3
	ECMWF Mean Speed (m/s):	7.4	ECMWF Mean Speed (m/s):	7.2
	Bias-ECMWF (m/s):	1.7	Bias-ECMWF (m/s):	5.1
	RMS-ECMWF (m/s):	4.1	RMS-ECMWF (m/s):	8.2
	Rain > 2 mm/hr (%[1]):	1.0	Rain > 2 mm/hr (%[1]):	31.9
	Rain > 2 mm/hr (%[2]):	2.4	Rain > 2 mm/hr (%[2]):	78.5

[1] : % of data in this category with rain (RR> 2 mm/hr)

[2] : % of all rain points (RR>2mm/hr)

13.9% in B) of rain.

In terms of quality of the data, both categories contain data of low quality, with similar bias (2.4 m/s in B and 1.7 m/s in C) and RMS (4.8 m/s in B and 4.1 m/s in C) values. The KNMI QC is more efficient in rejecting low quality data than the JPL rain flag since category C contains twice as much data as category B (4% in C; 2% in B). However, the JPL rain flag seems to work reasonably well as a Quality Control flag as categories B and D show that only 27% of that data (13.6% in B and 31.9% in D) are rain contaminated data and therefore the rest are rain-free but still low quality data.

Tables 20 and 21 are similar to table 19 but only for rain-free data and rain data respectively. Table 20 contains about 1.1 million data and table 21 about 17000 data.

Table 20 shows very similar results to table 19. The most significant result is that for rain-free data, categories B and D contain low quality data, as seen from the high bias (2.2 m/s in B and 4.4 m/s in D) and RMS (4.4 m/s in B and 7 m/s in D). This confirms the JPL rain flag as a Quality Control flag as well.

Table 21 shows clearly the effect of rain in the quality of the data. All categories have larger bias and RMS values compared to tables 19 and 20. In particular, category A contains 5.2% of rainy data, which are clearly of low quality (2.4 m/s bias and 5.5 m/s RMS). These data are detected neither by the JPL rain flag nor by the KNMI QC.

The results clearly show that category B contains low quality data, including a significant amount of rainy data. Therefore, it seems a good idea to incorporate the JPL rain flag to the KNMI QC in order to improve the Quality Control of QuikSCAT data. However, according to the results in these three tables, ECMWF winds in category B are in general significantly larger than in the rest of the categories, up to 4.7 m/s larger. This means that category B corresponds to dynamically active situations. Therefore, it could well be that this category systematically corresponds to frontal or low-pressure system areas where the discrepancy between ECMWF and QuikSCAT is indeed of valuable interest and therefore we want this data to be kept and not rejected.

In order to determine the convenience of incorporating the JPL rain flag in the KNMI QC, some meteorological cases need to be examined.

TABLE 20

	JPL Rain Flag No Rain			JPL Rain Flag Rain		
KNMI QC Accepted	Number of data (%): QuikSCAT Mean Speed (m/s): ECMWF Mean Speed (m/s): Bias-ECMWF (m/s): RMS-ECMWF (m/s):		92.7 7.0 6.5 0.5 2.0	Number of data (%): QuikSCAT Mean Speed (m/s): ECMWF Mean Speed (m/s): Bias-ECMWF (m/s): RMS-ECMWF (m/s):		1.3 12.2 10.0 2.2 4.4
KNMI QC Rejected	Number of data (%): QuikSCAT Mean Speed (m/s): ECMWF Mean Speed (m/s): Bias-ECMWF (m/s): RMS-ECMWF (m/s):		3.5 7.8 5.9 1.9 4.2	Number of data (%): QuikSCAT Mean Speed (m/s): ECMWF Mean Speed (m/s): Bias-ECMWF (m/s): RMS-ECMWF (m/s):		2.5 10.3 5.9 4.4 7.0

TABLE 21

	JPL Rain Flag No Rain			JPL Rain Flag Rain		
KNMI QC Accepted	Number of data (%): QuikSCAT Mean Speed (m/s): ECMWF Mean Speed (m/s): Bias-ECMWF (m/s): RMS-ECMWF (m/s):		5.2 10.8 8.4 2.4 5.5	Number of data (%): QuikSCAT Mean Speed (m/s): ECMWF Mean Speed (m/s): Bias-ECMWF (m/s): RMS-ECMWF (m/s):		13.9 13.7 9.0 4.7 8.2
KNMI QC Rejected	Number of data (%): QuikSCAT Mean Speed (m/s): ECMWF Mean Speed (m/s): Bias-ECMWF (m/s): RMS-ECMWF (m/s):		2.4 9.9 6.6 3.3 6.1	Number of data (%): QuikSCAT Mean Speed (m/s): ECMWF Mean Speed (m/s): Bias-ECMWF (m/s): RMS-ECMWF (m/s):		78.5 14.4 6.4 8.0 11.2

3.4.4 Cases

In order to determine the convenience of incorporating the JPL rain flag in the KNMI QC, many meteorological cases were examined. Indeed, some systematic effects were found that help in understanding the statistical results of section 3.4.3. In this section, we show two wind field examples which are representative of the entire set of examined cases. Figures 33 and 34 show QuikSCAT winds where both the KNMI QC

and the JPL rain flag have been applied. The arrows in plot a) correspond to the QuikSCAT JPL-selected wind solutions and the colors represent categories A (green), B (yellow), C (blue) and D (red). Plot b) is the same as plot a), but arrows corresponding to categories C and D are substituted by dots.

In Figure 33, the presence of a low-pressure system in the western North-Atlantic ocean is clearly discernible in the mid-right part of the plot. A wind front is partly visible going from northeast to south of the low. The KNMI QC has rejected data in the vicinity of the low and along the front line where a confused sea state is expected (see red and blue arrows). We can also see KNMI QC rejections at low-wind areas (blue arrows at bottom part of the plot), where the QuikSCAT retrieved wind flow is clearly inconsistent. As anticipated in the previous section, category-B winds (yellow arrows) are mainly focused in the most dynamical area.

If we look at the same case but only showing category-A and -B winds (accepted winds after KNMI QC), we see that most of the yellow arrows show a spatially consistent flow which we would like to keep. Moreover, the closest Meteosat image (not shown) to the QuikSCAT pass reveals no clouds (therefore no rain) south of the low (where most yellow arrows are located). We discern very few undesirable yellow arrows in the vicinity of the low (most likely low quality winds). Therefore, since the consistent category-B winds (yellow) are located in the sweet part of the QuikSCAT swath, it seems that the KNMI QC works fine in these regions.

In Figure 34, we see a front line in the mid part of the plot associated to a low pressure system, which is not observed by QuikSCAT, presumably located around 49° North and 314° East. The red arrows in the centre of plot a) clearly show the presence of rain bands along the front line. This is confirmed by SSM/I, which detects significant rain (rain rates above 6 mm/hr) in this area. As in the previous case, there is a large number of consistent winds rejected by the JPL rain flag (yellow arrows) in the nadir region (left side of the black solid line). Some of these winds are rain-contaminated but the rain rate, according to SSM/I, is around 2 mm/hr. In section 3.1, we show no significant effect on the quality of high winds at these rain rates.

If we look at the same case but only for the accepted data after KNMI QC (plot b), we still see some inconsistent wind (yellow arrows), which are most likely rain contaminated (unfortunately no SSM/I observations available but Meteosat shows thick clouds over that area) and therefore undesirable. These arrows are located in the nadir region of the swath (right side of the black solid line), where KNMI QC is expected to perform less well than in the sweet regions.

As explained in section 3.1.4, the reason for this lies in the nature of the QC. The QC is based on MLE and therefore on the quality of inversion. In contrast with the sweet regions, in the nadir region there is poor azimuth diversity among observations, which in turn leads to a decrease in the quality of inversion. Subsequently, not only the KNMI QC but also the wind retrieval skills are lower in the nadir region than in the sweet regions of the swath. The lower quality of the retrievals is indicated in the right mid-top part of the plot, where several inconsistent winds, which are accepted by both KNMI QC and JPL rain flag (green arrows), are discernible.

From the meteorological cases examined, we can conclude that category B winds are primarily located in dynamically active areas and in many cases they show very

consistent wind flows, notably in the sweet swath. However, there are also several rain-contaminated cases and low-quality winds in the nadir region, which belong to category B (and therefore not detected by KNMI QC) and are undesirable.

From plot b of both Figures, it is clearly discernible that rejecting category B winds can significantly reduce the synoptic-scale information content in some meteorological situations. Nevertheless, in the areas where the beam azimuth diversity is poor and therefore the quality of both the retrievals and the KNMI QC is lower, the rejection of category B winds is necessary.

Therefore, for QuikSCAT QC purposes, we recommend the use of the KNMI QC in the sweet parts of the swath. In the nadir regions however, the combined use of the JPL rain flag and the KNMI QC procedure is recommended.

CASE : 14/02/01 2200 UTC
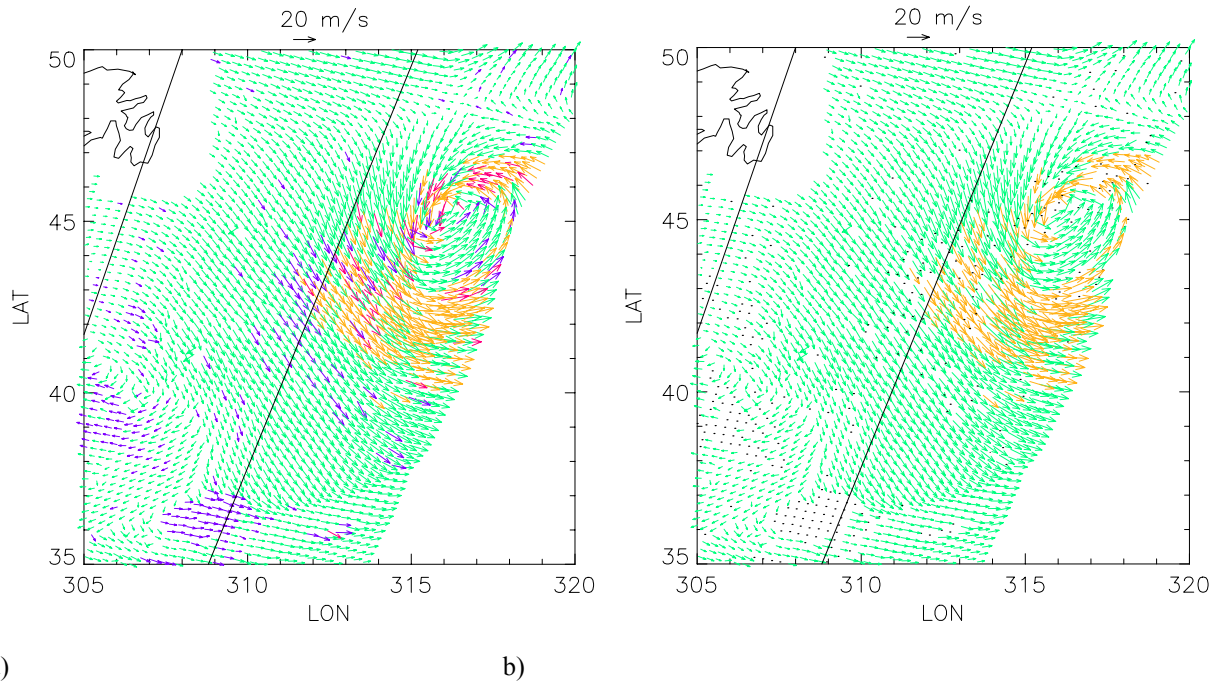

a)   b)

Figure 33 QuikSCAT wind fields. The colors represent the different categories: green is category A, yellow is B, purple is C, and red is D. Plot a shows all retrieved winds while plot b shows only KNMI QC accepted winds. The black solid lines separate different regions of the swath. In this case, the left side of the plot corresponds to the sweet-right region, the middle to the nadir region and the right side to the sweet-left region. The acquisition date is February 14 2001 at 22 hours UTC.

CASE : 20/01/01 2030 UTC

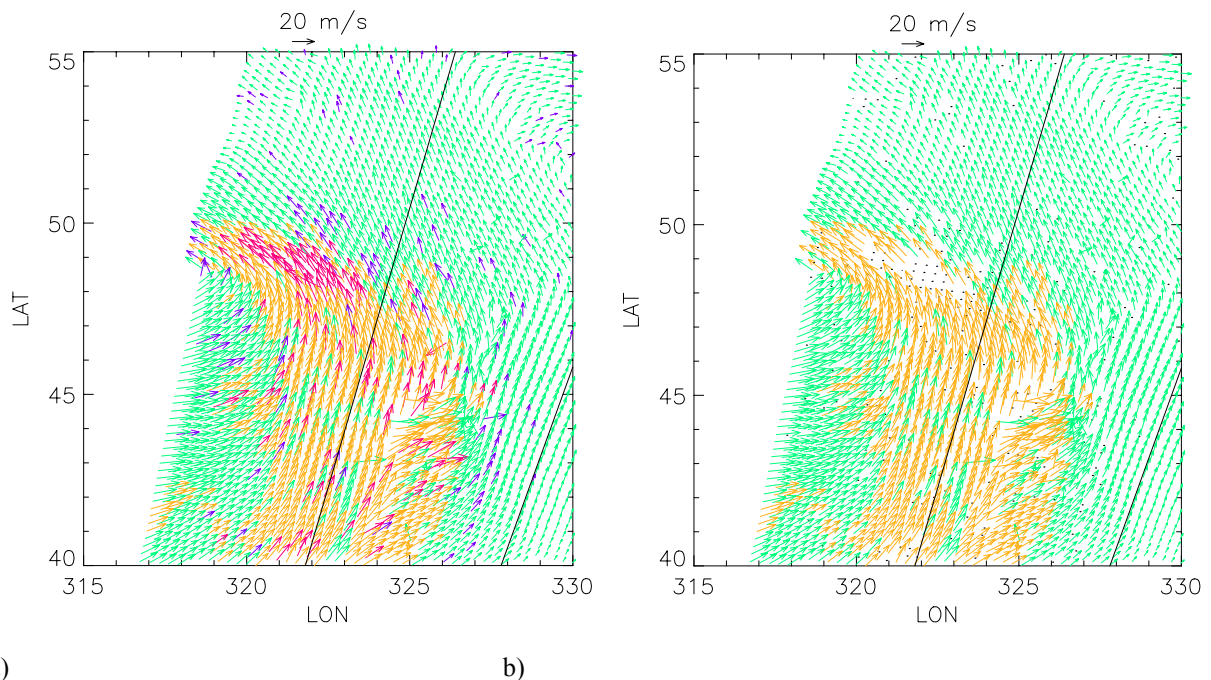a)   b)

Figure 34 Same as Figure 33 but for different date (January 20 2001 at 20:30 hours UTC) and location. As in the previous figure, the black solid lines separate the sweet-right (left side), the nadir (middle) and the sweet-left (right side) regions QuikSCAT wind fields.

4   Wind Retrieval

As discussed in section 1, the wind retrieval from scatterometer observations includes inversion, quality control, and ambiguity removal. The skill of the QuikSCAT wind retrieval depends on the antenna geometry and therefore on the swath region. The skill decreases in the regions of the swath with poor azimuth diversity. In this section, we examine the inversion problem of QuikSCAT and present a method, which uses the output from the inversion to potentially improve the wind retrieval. For this purpose, the KNMI QuikSCAT inversion software (see Appendix E) is used. The QC as described in section 3 is also used in the study.

4.1   Inversion

The relationship between any instrument observation or set of observations and one or more geophysical state variables is generally represented with the following equation:

$$\mathbf{y} = \mathbf{H}(\mathbf{x}) \tag{21}$$

where $\mathbf{y}$ is the vector of observations, $\mathbf{x}$ is the vector of state variables that we want to derive, and $\mathbf{H}$ is the forward model which relates the state variables to the observations. The process of deriving the best estimate of $\mathbf{x}$ for a given $\mathbf{y}$, allowing for observation errors, is called inversion. There are several approaches for inverting remotely-sensed variables, including Bayes' theorem, exact algebraic solutions, relaxation, least squares, truncated eigenvalue expansions, etc (*Rodgers, 2000*). The most general approach to the problem is the Bayesian approach. This approach is also used on scatterometry, where the inversion process is highly non-linear.

4.1.1   Scatterometer inversion

The empirically-derived scatterometer forward model function (GMF), which relates the state variables (wind speed and wind direction) to the observations (radar backscatter), is generally defined as:

$$\sigma^o = B_0 \left[1 + B_1 \cos(\phi) + B_2 \cos(2\phi) \right]^z \tag{22}$$

where ϕ is the wind direction ($\phi = 0°$ for a wind blowing towards the radar), and the coefficients B_0, B_1 and B_2 depend on the wind speed, and the local incidence angle, the polarization, and the frequency of the radar beam. The value of the exponent z and the number of harmonics (additional harmonics may be added to equation 22) depend on the tuning performed for each GMF. The model is based on the backscatter from

the rough ocean surface for moderate incidence angles (20°-60°), which is dominated by resonant Bragg scattering (*Valenzuela*, 1978). Additionally, Rayleigh scattering and specular reflection may contribute to the backscatter. The GMF is tabulated in order to speed-up the inversion computation. In the case of QuikSCAT, the speed binning is 0.2 m/s and the direction binning is 2.5°.

As mentioned, the Bayesian approach is used to invert winds from scatterometer observations. Several optimisation techniques, which depend on the desired statistical objective, can be applied when using the Bayesian approach, including maximum likelihood, maximum posterior probability, minimum variance, minimum measurement error, etc. The maximum likelihood estimator (MLE) is the most commonly used technique on scatterometry (*Pierson, 1990*). The MLE as defined in equation 1 is the result of applying the Bayes' theorem for inverting equation 22, assuming independent Gaussian measurement errors and no prior knowledge on the probability density of σ°. As discussed in section 3, the MLE is a measure of the distance between a set of radar backscatter measurements and the solution lying on the GMF surface in a transformed measurement space where each axis of this space is scaled by the noise. The optimisation technique consists of looking for a minimum (maximum probability) of equation 1. Since it is computationally expensive to search for minimum MLE in the entire wind domain, the following procedure is commonly applied:

- For a particular wind direction, the minimum MLE is searched in the wind speed domain, which, in contrast with the wind direction domain, behaves quasi-linearly and a single well-determined minimum is usually found. The search is performed at the speed step size (although it can be different) given by the table (0.2 m/s for QuikSCAT tables)

- The same operation is repeated for every wind direction, at the step size given by the table (2.5° for QuikSCAT tables).

- The resulting minimum MLE as a function of wind direction (here called cost function) is searched for minima. There are typically up to 4 minima, which are called ambiguous wind solutions.

Figure 35 shows an example of the MLE cost function for QuikSCAT. The green diamond symbols indicate the ambiguous wind solutions detected by the inversion procedure. The MLE value can be interpreted as the likelihood of being the "true" wind. Therefore, the modulation of the minima determines the accuracy of the wind retrieval. The broader the minima, the less accurate the retrieved winds are, since we are discarding the neighbouring wind solutions to the minima, which are of comparable probability of being the true wind. The depths of the minima relative to each other determine in this case the likelihood of each ambiguous solution of being the "true" wind and therefore the ambiguity or uncertainty of the system. The closer the secondary minima to the primary (deepest) minimum in depth and the larger the number of (deep) minima, the more ambiguous the wind retrieval is.

The modulation of the cost function is also important in terms of wind retrieval accuracy. It shows how unlikely are the lowest likelihood points of the cost function compared to the highest likelihood points. For example, the low GMF modulation at

low winds results in a low cost function modulation. In this case, the wind direction solutions coming out of the inversion are not so meaningful anymore, since the current procedure is discarding (and therefore assigning null probability to) many cost function points of comparable probability to that of the ambiguous solutions. The low cost function modulation therefore results in low quality winds when using the current wind retrieval procedure.

As we will see in the following sections, if we properly use the information on accuracy and ambiguity derived from the MLE cost function, the wind retrieval may improve significantly.
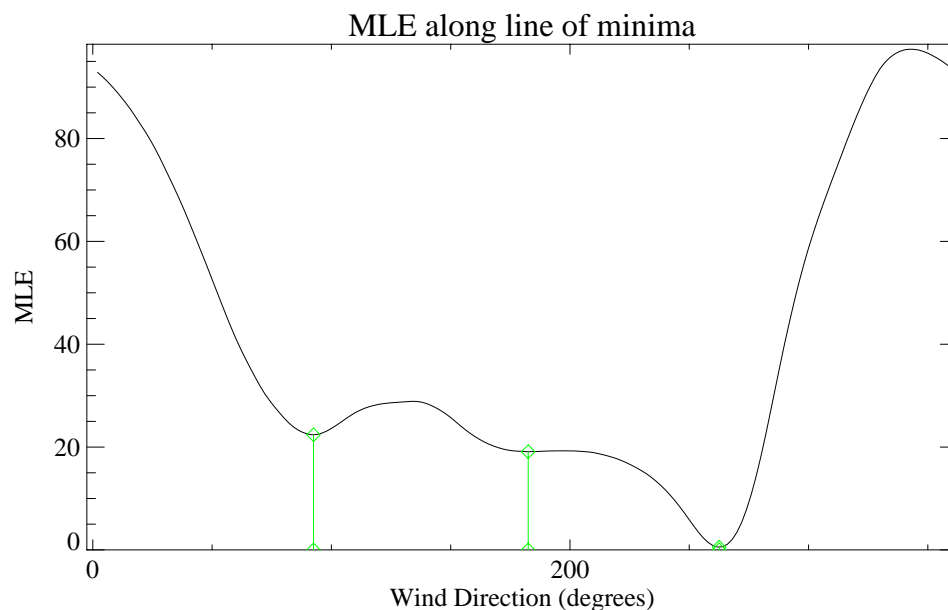

Figure 35 Example of MLE cost function for QuikSCAT WVC number 33. The green diamond symbols indicate the locations of the minima found by the inversion procedure.

4.1.2 QuikSCAT inversion problem

As said in section 0, the wind retrieval performance decreases in the nadir and the outer regions of the QuikSCAT swath. This is an inherent problem of the QuikSCAT inversion, which is reflected in the shape of the MLE cost function.

The example shown in Figure 35 corresponds to WVC number 33. This WVC is inside the nadir region, close to the sweet region. As we approach the nadir sub-track of the satellite (WVC numbers 38 and 39) and the azimuth diversity decreases, the MLE cost function minima tend to become broader and therefore wind retrieval less accurate. In contrast, when approaching the sweet region and the azimuth diversity increases, the minima become steeper and consequently the wind retrieval more accurate. In the outer region, the wind vector is not anymore overdetermined since there are only two beams. The MLE cost function will have most of the times 4 minima with nearly equal and low MLE values (very often zero values, as discussed

in section 3.1.1). The outer region is therefore the most ambiguous of the QuikSCAT swath. The minima in this region will be steep and therefore as accurate as those in the sweet swath, except for the nodes at the edges of the swath, where the two outer beams are close to each other (poor azimuth diversity) and therefore broad minima in wind direction are again present.

In order to better illustrate the QuikSCAT inversion problem, we have inverted QuikSCAT winds (using the KNMI inversion software) and performed collocations with ECMWF model winds over a period of 12 hours (more than 7 orbits).

Figure 36 shows the two-dimensional histograms of the 1st rank (deepest cost function minimum) KNMI-retrieved wind solution versus the ECMWF wind for wind speed (left plots) and wind direction (right plots), and for different parts of the swath: sweet (top plots), nadir (mid plots) and outer (bottom plots) regions. The ambiguity of the system is reflected in the quality of the 1st rank solution. In other words, the deeper the 1st rank in comparison with the secondary minima (lower ambiguity), the higher the likelihood of being the "true" wind (higher 1st rank quality) is. It is clearly discernible from the plots that the sweet swath is the region with the best 1st rank skill. It has the lowest bias and SD values and the highest correlation values of the entire swath in both speed and direction. As expected, the worst 1st rank skill corresponds to the outer regions. The uncertainty or ambiguity is revealed in the wind direction contour plots as data accumulation away from the main diagonal (see 0° line departure in the plots). In particular, the typical 180° ambiguity of scatterometer data is shown as data accumulation along the 180° diagonals. Again, the sweet region (plot b) shows little data accumulation away from the main diagonal, mainly located along the 180° diagonals. In the nadir swath (plot d), the data accumulation away from the main diagonal is larger and somewhat more spread in comparison with the sweet swath, denoting a slightly worse ambiguity problem. In the outer swath (plot f), it is clearly discernible the large accumulations of data along the 180° diagonals and elsewhere, denoting the significant ambiguity of the system at these regions.

Figure 37 shows the same as in Figure 36 but for the KNMI-retrieved wind solution closest to the ECMWF wind. The quality of the closest solution gives an idea of the accuracy of the wind retrieval. The sweet swath (top plots) shows again low bias and SD values and high correlation values in both speed and direction. The outer swath (bottom plots) shows similar scores. The wind speed and wind direction contour lines of both the sweet and the outer swaths are close to the diagonal line, denoting again high accuracy of the wind retrieval. However, this is not the case for the nadir swath (mid plots). Moreover, the bias and SD values are significantly larger than in the rest of the swath, denoting relatively poor wind retrieval accuracy.

As seen in Figures 36 and 37, although there is a significant ambiguity problem in the outer swath, its accuracy is comparable to that of the sweet swath. Therefore, if there is a way to remove the inherent ambiguity, the outer swath could provide accurate winds. At KNMI, a NRT 100-km resolution QuikSCAT wind product, which includes a variational analysis scheme for AR purposes, called 2D-Var (see description in section 4.2), has been developed. Since QC is still an issue in the outer swath (see discussion in section 3.1.1), the 2D-Var AR has not yet been tested in this region, although we anticipate it may work properly. That is, given the area extension where 2D-Var is performed (the QuikSCAT inner swath is 1400 km wide), we expect 2D-

Var to be able to extrapolate to the outer region. However, the lack of a reliable QC remains, as it can be inferred from Figure 36e. The bias at high wind speeds (note how the contour lines are not centered on the diagonal anymore), only seen in the outer swath (compared with Figures 36a and 36c), denotes possibly rain contamination, as discussed in section 3.1.3. [Note that in the outer swath we perform the same QC as in the nadir swath, i.e. a combination of KNMI QC and JPL rain flag]. Nevertheless, Figure 37e shows only small bias at high winds compared to Figure 36e. This suggests that, if it rains in the outer swath and the data are not rejected by the KNMI QC nor by the JPL rain flag, there is still a solution close to the "truth".

The accuracy problem of the nadir swath has not been solved yet. The retrieved winds very often show inconsistent wind flow patterns, which are rather confusing and difficult to interpret. In order to solve the problem, JPL performed a new wind retrieval scheme, called DIRTH (*Styles et al.*, 2000). However, the resulting wind fields are just a smooth version of the inverted wind direction, showing still very little meteorological consistency (we address this issue in section 4.2.3).

Given the lack of a reliable QC for the outer swath, we are going to focus our research on improving wind retrieval in the inner swath (sweet + nadir), giving special attention to the nadir swath. However, the results of the research are obviously applicable to the outer swath as well. We hope that the wind vector consistency checks in the 2D-Var will be sufficient for QC here.
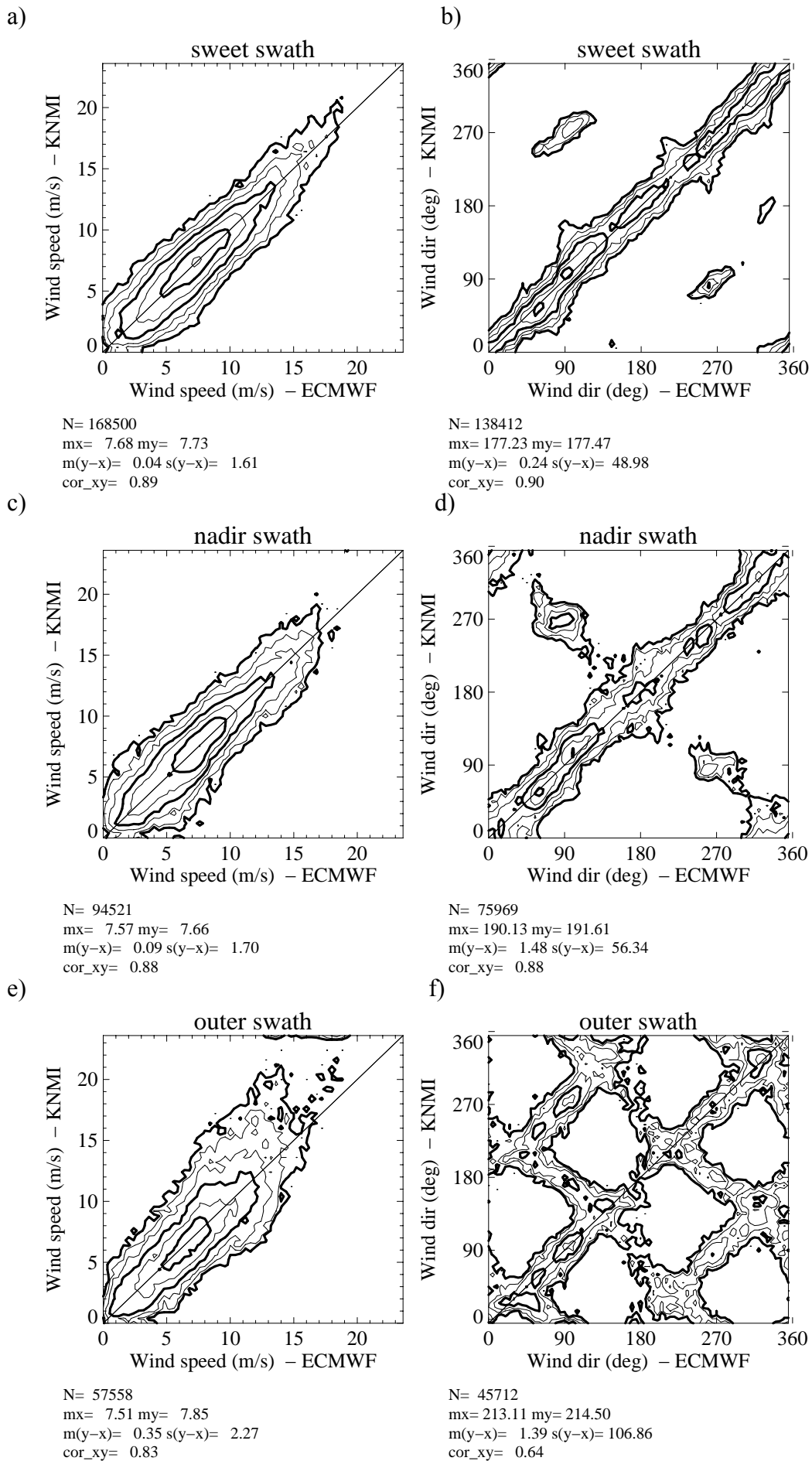
Figure 36 Two-dimensional histogram of the 1ˢᵗ rank KNMI-retrieved wind solution versus ECMWF wind in the different parts of the swath: the sweet (top plots), the nadir (mid plots) and the outer (bottom plots) regions. The left plots correspond to wind speed (bins of 0.4 m/s) and the right plots to wind direction (bins of 2.5°). The legend and the contour lines are the same as in Figure 21 (the lowest contour level is, in this case, N/8000 data).

a)

sweet swath

N= 168500
mx= 7.68 my= 7.78
m(y−x)= 0.09 s(y−x)= 1.56
cor_xy= 0.90

b)

sweet swath

N= 138791
mx= 171.24 my= 171.57
m(y−x)= 0.33 s(y−x)= 15.15
cor_xy= 0.99

c)

nadir swath

N= 94521
mx= 7.57 my= 7.68
m(y−x)= 0.11 s(y−x)= 1.67
cor_xy= 0.88

d)

nadir swath

N= 76072
mx= 176.67 my= 178.13
m(y−x)= 1.46 s(y−x)= 20.80
cor_xy= 0.98

e)

outer swath

N= 57558
mx= 7.51 my= 7.53
m(y−x)= 0.02 s(y−x)= 1.58
cor_xy= 0.90

f)

outer swath

N= 45797
mx= 174.87 my= 175.10
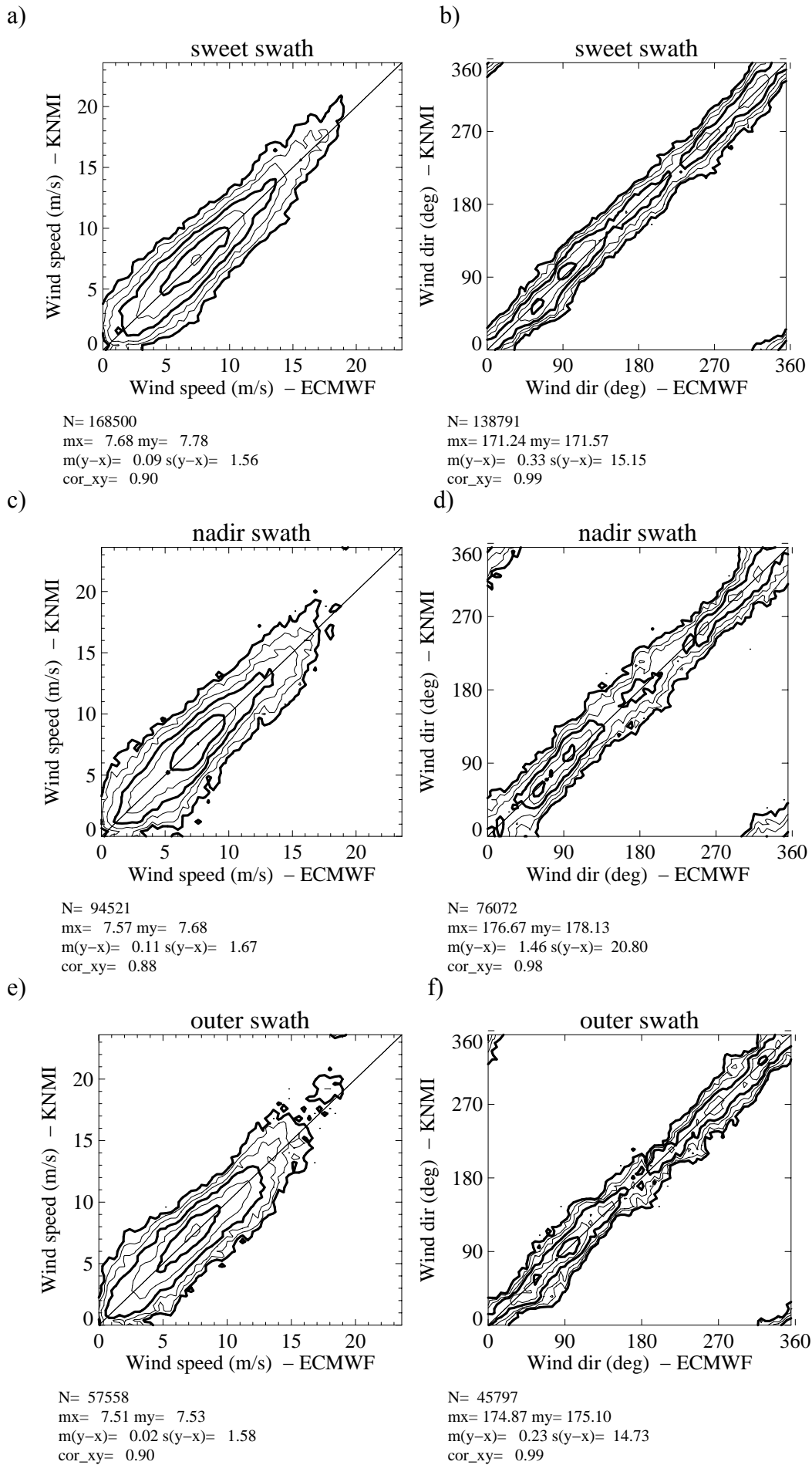m(y−x)= 0.23 s(y−x)= 14.73
cor_xy= 0.99

Figure 37 Same as Figure 36 but for the KNMI-retrieved wind solution closest to ECMWF wind.

4.1.3 Inversion tuning

Although the QuikSCAT inversion problem discussed in section 4.1.2 is inherent of the inversion process and therefore not solvable at this stage, a further examination of such process is desirable in order to optimize it for QuikSCAT.

NSCAT-2 versus QSCAT-1

As said in section 3.4.1, since May 2000, the JPL QuikSCAT winds are retrieved using the QSCAT-1 GMF, which was empirically derived GMF from QuikSCAT measurements. Before that date, JPL was using the NSCAT-2 GMF, derived from NSCAT measurements. Since we have had access to both NSCAT-2 and QSCAT-1 tables, it seems reasonable to compare them, using the KNMI inversion software, in order to choose the most appropriate for QuikSCAT wind retrieval. The same set of collocated ECMWF winds of the previous section is also used here for reference.

Figure 38 shows the wind direction distributions with respect to the satellite flight direction of ECMWF winds (solid lines) and QuikSCAT retrieved solutions closest to ECMWF (dotted lines). The QuikSCAT winds from the top plots are retrieved using NSCAT-2 GMF; the ones from the bottom plots are retrieved using QSCAT-1 GMF. The left plots show the wind direction distributions of WVC number 20. It is discernible from these plots (a and c) that the QSCAT-1 wind direction distribution fits better the ECMWF distribution than the NSCAT-2 distribution, where some unrealistic accumulations are discernible (see peaks around 60°, 120° and 230° in plot a). Looking at the direction distributions over the entire inner swath (right plots), we still see a better fit of QSCAT-1distributions, denoting that the QSCAT-1 wind directions are somewhat more realistic than NSCAT-2 directions.

This result is in line with the RMS difference values between QuikSCAT and ECMWF wind directions. As expected, the RMS difference in wind direction is lower for QSCAT-1 than for NSCAT-2 in both the sweet and the nadir swaths (see table 22).

TABLE 22

	RMS in Speed (m/s) NSCAT-2/QSCAT-1	RMS in Direction(°) NSCAT-2/QSCAT-1	NRMS NSCAT-2/QSCAT-1
Sweet swath	1.57 / 1.66	21.39 / 19.36	0.4953 / 0.5113
Nadir swath	1.67 / 1.73	29.14 / 27.56	0.5359 / 0.5619

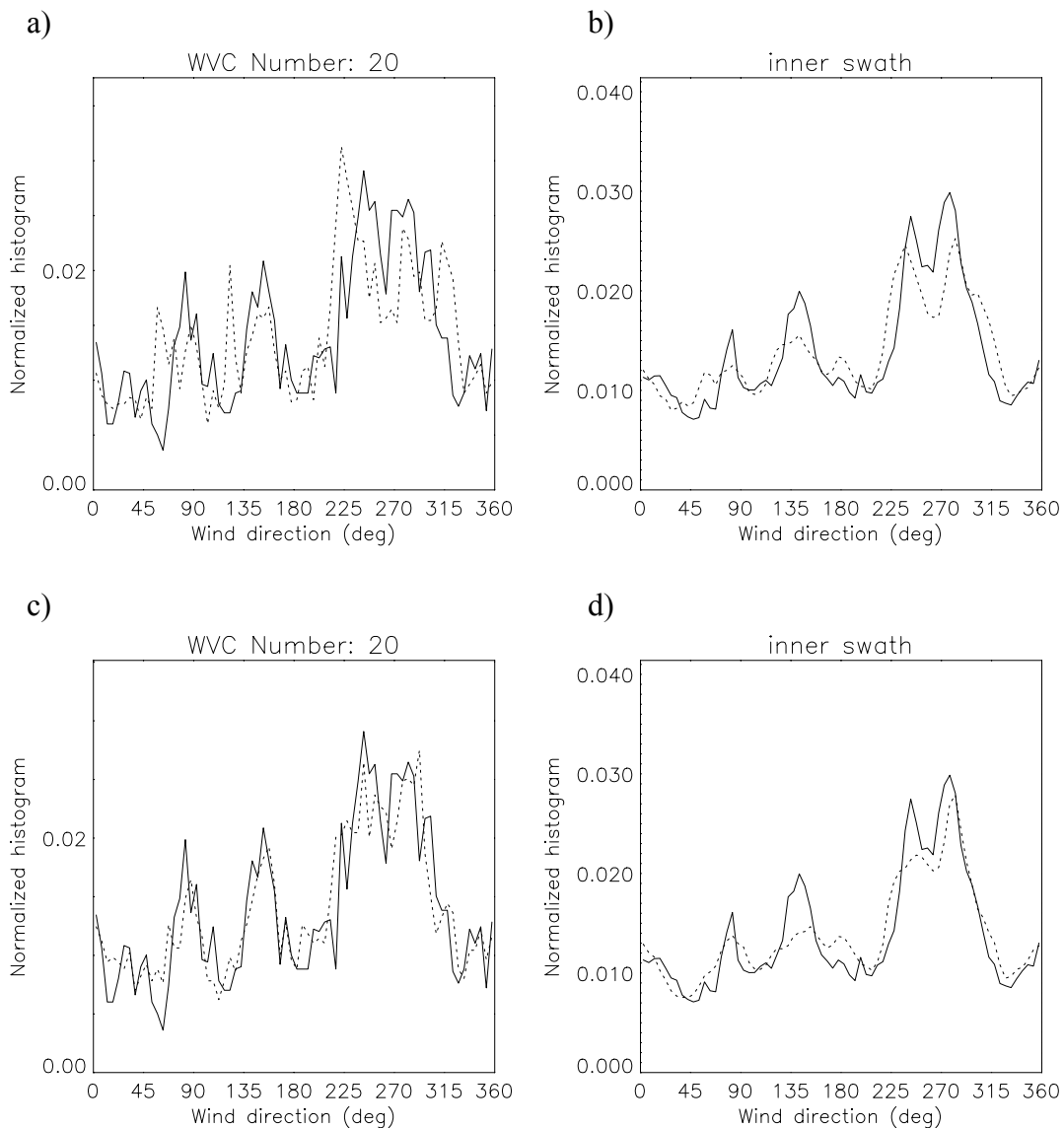Note: Non-smoothing and 2D interpolation have been used in the inversion.

Figure 38 Wind direction (with respect to the satellite flight direction) histograms of ECMWF winds (solid lines) and QuikSCAT-retrieved solutions closest to ECMWF (dotted lines) for WVC number 20 (left plots) and for the inner swath (right plots). The QuikSCAT winds have been retrieved using NSCAT-2 GMF (top plots) and QSCAT-1 GMF (bottom plots). Non-smoothing and 2D interpolation have been used in the inversion.

Tables 23 to 26 show the percentage of "selected" solutions (closest to ECMWF) stratified by number of solutions and rank. The number of solutions corresponds to the number of minima in the MLE cost function and the solution ranking goes from the deepest to the shallowest cost function minimum in ascending order. The first row corresponds to the number of data stratified by number of solutions. Tables 23 and 24 correspond to the NSCAT-2 GMF selected solution distributions of the sweet and nadir swaths, respectively. Tables 25 and 26 correspond to QSCAT-1 GMF selected solution distributions of the sweet and nadir swaths, respectively.

TABLE 23 NSCAT-2 GMF (Sweet swath)[1]

	1 Solution	2 Solutions	3 Solutions	4 Solutions	All Solutions
Number of Data	378	62856	44029	61172	168435
Rank 1	100	90	81	79	84
Rank 2	-	10	14	16	13
Rank 3	-	-	5	3	2
Rank 4	-	-	-	2	1

TABLE 24 NSCAT-2 GMF (Nadir swath)[1]

	1 Solution	2 Solutions	3 Solutions	4 Solutions	All Solutions
Number of Data	6877	48382	30943	8303	94505
Rank 1	100	81	79	64	80
Rank 2	-	19	16	19	17
Rank 3	-	-	5	9	2
Rank 4	-	-	-	8	1

TABLE 25 QSCAT-1 GMF (Sweet swath)[1]

	1 Solution	2 Solutions	3 Solutions	4 Solutions	All Solutions
Number of Data	29	45139	48795	74473	168436
Rank 1	100	94	81	74	81
Rank 2	-	6	14	18	14
Rank 3	-	-	5	5	4
Rank 4	-	-	-	3	1

TABLE 26 QSCAT-1 GMF (Nadir swath)[1]

	1 Solution	2 Solutions	3 Solutions	4 Solutions	All Solutions
Number of Data	4000	45806	36279	8413	94498
Rank 1	100	82	78	70	80
Rank 2	-	18	16	20	17
Rank 3	-	-	6	6	3
Rank 4	-	-	-	4	0

[1] Non-smoothing and 2D interpolation have been used in the inversion.

As discussed in section 4.1.2, the 1st rank skill shows the ambiguity or uncertainty of the inversion. In these tables, the 1st rank skill is shown by the percentage of selections of rank 1 solution. As we see in the tables, in general the 1st rank skill is higher for NSCAT-2 than for QSCAT-1 in the sweet swath and comparable in the nadir swath (see overall results in the last column of the tables). Moreover, the number of solutions given by the NSCAT-2 GMF is significantly smaller than the number given by QSCAT-1 in both the sweet and the nadir swaths (see the relative accumulation of data for 3 and 4 solutions of QSCAT-1 tables compared to NSCAT-2 tables). This shows that NSCAT-2 GMF produces a much less ambiguous wind product than QSCAT-1.

Figure 39 shows the two-dimensional histograms of the QuikSCAT retrieved wind solution closest to ECMWF versus the ECMWF winds for zonal (left plots) and meridional (right plots) components. The QuikSCAT winds from the top plots are retrieved using NSCAT-2 GMF; the ones from the bottom plots are retrieved using QSCAT-1 GMF. As discussed in section 4.1.2, the quality of the closest gives an idea of the acccuracy of the retrieved winds. No significant difference is discernible when comparing NSCAT-2 (top) and QSCAT-1 (bottom) plots. However, if we look at the legend we see slightly lower SD values for NSCAT-2 compared to QSCAT-1. [Note: these histograms correspond to the sweet parts of the swath; similar conclusions can be derived from the nadir swath histograms (not shown)]. Although the RMS difference in direction is lower for QSCAT-1 than for NSCAT-2 winds, the RMS difference in speed is lower for NSCAT-2 than for QSCAT-1 (see table 22), leading to an overall comparable accuracy, slightly higher for NSCAT-2 winds.

Stoffelen et al. (2000) computed a more realistic RMS difference in wind direction, called the normalized RMS (NRMS). Using the actual RMS definition, the more ambiguous solutions are provided by the inversion, the smaller the RMS will be, because the chance that one of the solutions will be close to the wind reference will increase. In the limit of an infinite amount of observations, the RMS will even be zero, while the information content of the set of solutions in reality decreases with an increasing number of solutions, because there is no a priori way to say which of the solutions is the correct one. In order to solve this problem, they normalize the RMS with an expected value, which is dependent on the angle separation of the neighboring solutions of the closest solution to reference (ECMWF in this case). For more details, see *Stoffelen et al.* (2000). If we compute the NRMS, we get lower values for the less ambiguous NSCAT-2 product than for QSCAT-1 (see table 22).

Both the RMS and the NRMS parameters are not the true and only way to look at the accuracy of the retrieved winds. Moreover, the ECMWF is just a reference. Therefore, it is difficult to say precisely from the results, which of the two GMFs produces more accurate winds. However, it is clear that both GMFs produce winds of comparable accuracy.

Therefore, the NSCAT-2 provides a less ambiguous product than QSCAT-1 without decreasing the quality of the wind retrieval. In other words, in comparison with QSCAT-1, NSCAT-2 is capable of removing a significant amount of unrealistic ambiguous wind solutions. Moreover, as discussed in section 3.4.1, the NSCAT-2 GMF better fits the backscatter measurements than the QSCAT-1 GMF. Consequently, the NSCAT-2 GMF will be used for inverting QuikSCAT winds.

a)

sweet swath

N= 168500
mx= −1.11 my= −1.03
m(y−x)= 0.08 s(y−x)= 1.83
cor_xy= 0.96

b)

sweet swath

N= 168500
mx= −0.21 my= −0.20
m(y−x)= 0.02 s(y−x)= 1.89
cor_xy= 0.94

c)

sweet swath

N= 168500
mx= −1.11 my= −1.10
m(y−x)= 0.01 s(y−x)= 1.84
cor_xy= 0.96

d)

sweet swath

N= 168500
mx= −0.21 my= −0.22
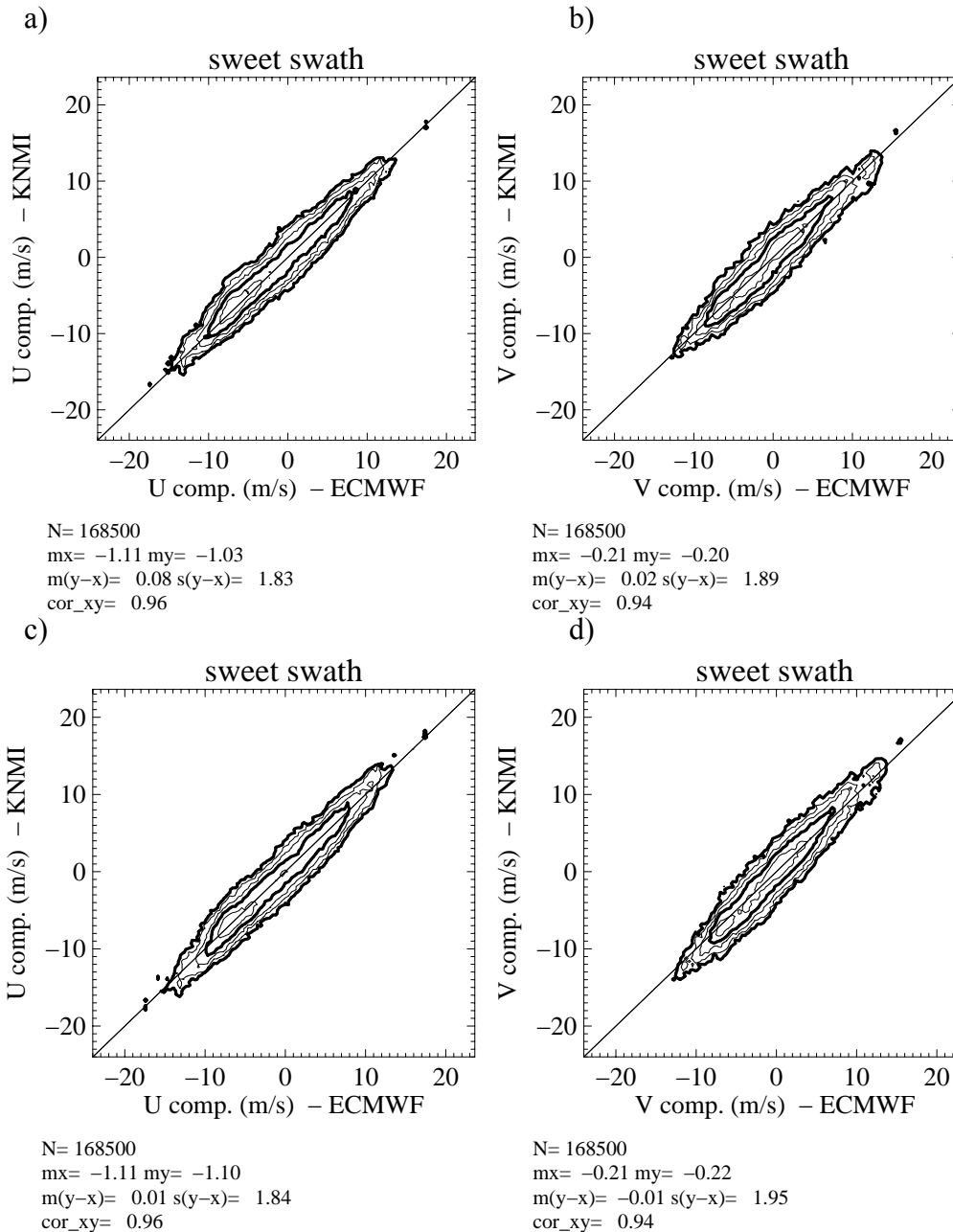m(y−x)= −0.01 s(y−x)= 1.95
cor_xy= 0.94

Figure 39 Two-dimensional histogram of the closest KNMI-retrieved wind solution to ECMWF wind versus ECMWF wind for QuikSCAT winds derived with the NSCAT-2 (top plots) and the QSCAT-1 (bottom plots) GMFs. The left plots correspond to the zonal wind component and the right plots to the meridional wind component (bins of 0.4 m/s for both components). The legend and the contour lines are the same as in Figure 21 (the lowest contour level is, in this case, N/8000 data). Non-smoothing and 2D interpolation have been used in the inversion.

Smoothing versus interpolation

The MLE cost function is often noisy (imagine very small peaks and troughs in Figure 35). This leads to the detection of excessive minima close to each other in the inversion process, especially in the nadir swath where the minima tend to be broad. A common way to solve the problem is to apply a smoothing technique over the cost function. The idea is to define a smoothing window whose size is determined by the

number of cost function points below a certain threshold. This threshold can be defined for example as a factor of the minimum MLE value, the minimum Rn value, or the difference between the maximum and the minimum MLE values in the cost function. Here we test a couple of smoothing techniques, whose main difference is the resulting window sizes, and compare them to a non-smoothing inversion (smoothing window size is zero). Figure 40 shows the smoothing window size distribution over the mentioned 12-hour period of QuikSCAT data and the entire inner swath for two different techniques. Since we use the same wind direction step size as the one defined in the table (2.5°) to compute the MLE cost function, the latter has a total of 144 points. The number of points used in the smoothing is = 2 x window size + 1. The difference between technique I (plot a) and technique II (plot b) lays in the window size distribution, whose mean value is around 1-2 in the former and 4-5 in the latter.
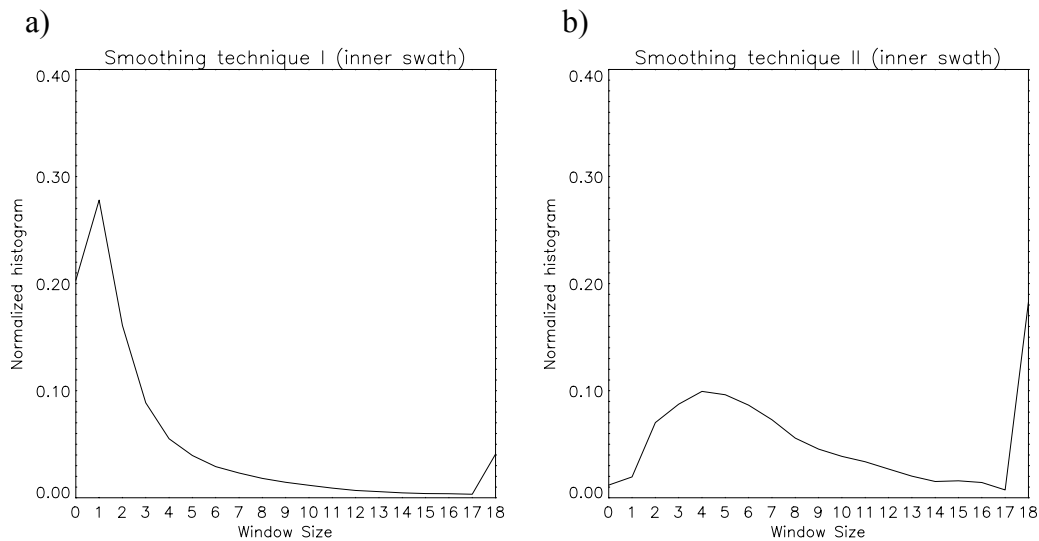
a)

b)

Figure 40 Normalized histograms of the smoothing window size for the smoothing techniques I (plot a) and II (plot b) over the entire inner swath.

Figure 41 shows the same wind direction distributions as Figure 38a but for no smoothing (plot a), smoothing technique I (plot b) and smoothing technique II (plot c). It is clearly discernible from the plots that there is an increase of unrealistic retrieved wind directions as we increase the window size (see evolution of peaks centered around 60°, 120° and 230° from plot a to plot c). This shows how sensitive can be the smoothing to the quality of the retrieval. As we increase the smoothing window, the MLE cost function changes shape and the minima are therefore shifted. Due to the non-linearity of the cost function, some wind directions are favoured in the smoothing process, leading to an increase of unrealistic accumulations at certain directions as shown in plots b and c.

An alternative to the smoothing is the interpolation of the table. As mentioned in section 4.1.1, to compute the MLE cost function, we search for a minimum in the speed domain and then we repeat this operation for the entire wind direction spectrum. This is usually performed at the table resolution level for speed (0.2 m/s) and direction (2.5°), and only the incidence angles are interpolated (the step size is 1° in the tables). However, the GMF is very sensitive to speed changes and this may lead

to inaccuracies in the selection of the minimum, which in turn can produce noise in the MLE cost function. Therefore, we perform a two-dimensional linear interpolation both in the incidence angle and the speed domains, and refine the minimum search in speed to a resolution of 0.02 m/s. [Note that tests at a higher resolution search in the speed domain, up to 0.001 m/s, have been performed with similar results].

Figures 41a and 38a show the retrieved wind direction distributions (compared to ECMWF) for interpolating in 1D (only incidence angle) and in 2D (incidence angle and speed). The QuikSCAT wind direction distributions look almost identical. In contrast with smoothing, the interpolation in the speed domain is not adding any unrealistic accumulation of retrieved directions. This is an expected result, since the interpolation is looking for a more precise minimum but not changing the shape of the MLE cost function.
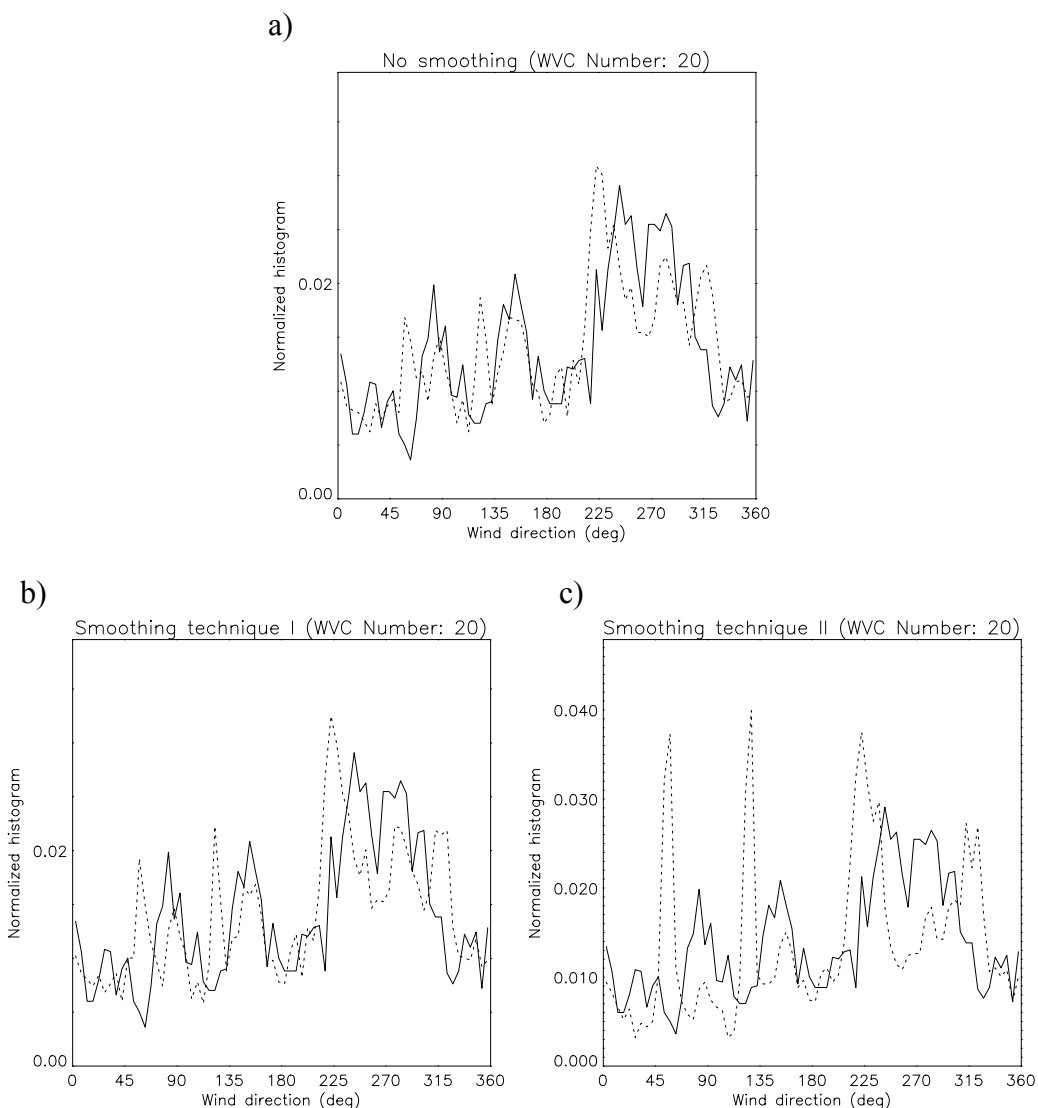
a)

b)

c)

Figure 41 Same as Figure 38a but for no smoothing (plot a), smoothing technique I (plot b) and smoothing technique II (plot c). The 1D interpolation scheme has been used in the inversion.

Tables 27 and 28 are similar to the tables 23 and 24 respectively. In the former, 1D interpolation has been used, while 2D interpolation is used in the latter. The 2D interpolation scheme has much less number of solutions (see the decrease in the number of data with 4 solutions in the 2D tables compared to the 1D tables) and a higher 1st rank skill (see higher percentages of rank-1 solutions for the 1D tables compared to the 2D tables), resulting in a less ambiguous product compared to the 1D product. In the nadir region, since the minima tend to be broad, the noise in the cost function is expected to produce more ambiguity than in the sweet swath where minima are steeper. Notice the significant reduction of ambiguity in the nadir of the 2D scheme with respect to the 1D scheme, denoting a clear reduction of the cost function noise.

TABLE 27 NSCAT-2 GMF (Sweet swath)[1]

	1 Solution	2 Solutions	3 Solutions	4 Solutions	All Solutions
Number of Data	132	50786	40677	76835	168430
Rank 1	100	92	77	73	80
Rank 2	-	8	18	18	15
Rank 3	-	-	5	6	4
Rank 4	-	-	-	3	1

TABLE 28 NSCAT-2 GMF (Nadir swath)[1]

	1 Solution	2 Solutions	3 Solutions	4 Solutions	All Solutions
Number of Data	571	18900	20599	54437	94507
Rank 1	100	81	71	42	56
Rank 2	-	19	24	23	22
Rank 3	-	-	5	18	12
Rank 4	-	-	-	17	10

[1] Non-smoothing and 1D interpolation have been used in the inversion.

Table 29 is similar to the left column (NSCAT-2 results) of table 22. Again, the former corresponds to the results of the 1D scheme, and the latter to the results of the 2D scheme. When comparing the two tables, we notice no significant differences, and therefore no significant difference in the quality of both interpolation schemes. The speed RMS values are almost identical and the direction RMS is somewhat higher in the 2D scheme compared to the 1D scheme. In contrast, the NRMS of the 2D scheme

is lower compared to that of the 1D scheme, especially in the nadir region, as expected from the lower ambiguity of the 2D scheme already mentioned.

TABLE 29

	RMS in Speed (m/s) NSCAT-2	RMS in Direction(°) NSCAT-2	NRMS NSCAT-2
Sweet swath	1.57	20.89	0.5095
Nadir swath	1.65	25.57	0.8422

Note: Non-smoothing and 1D interpolation have been used in the inversion.

If we go back to the discussion on the smoothing, the smoothing technique I produces similar ambiguity, speed RMS and NRMS values (not shown) than the 2D scheme. However, the RMS in direction for the smoothing technique I is 10% higher than for the 2D scheme due to the unrealistic direction accumulations already discussed. The smoothing technique II is producing the least ambiguous product of all. This is reflected in only a small decrease of the NRMS (drop of 2% in the sweet swath and 5% in the nadir region) in comparison with the 2D scheme. However, the direction RMS difference of the smoothing technique II is about 20% higher than that of the 2D scheme.

Therefore, we can say that the 2D scheme is the only examined scheme, which considerably reduces the ambiguity of the retrieved winds without affecting their quality in comparison to the flat scheme (1D interpolation). The smoothing techniques are meant to remove undesired wind solutions. However, this is not evident for QuikSCAT at low winds, where the solution pattern (we have examined many cases) is very noisy and does not show clearly undesirable solutions, which may be removed by smoothing with the consequent decrease in quality. [Note that the smoothing techniques have also been tested in combination with the 2D interpolation resulting in similar problems than when combined with the 1D interpolation]. Therefore, for QuikSCAT, it is better to keep all the information (no smoothing) and use the 2D scheme.

4.2 Solution probability

The problem of the noisy solution pattern at low winds discussed in the previous section becomes more acute in the nadir region. From the examined cases, it is clear that only providing the information of the minima to the AR is not enough. The way to solve this problem lays in the interface from inversion to AR. In other words, to improve the wind retrieval for QuikSCAT, the output from inversion or MLE cost function (and its associated wind solutions) has to be used in an appropriate way. A natural step on scatterometry is to use as interface the solution probability rather than the MLE. For a particular wind solution, there is a direct relationship between its

MLE value and its probability of being the "true" wind. In order to understand the importance of the solution probability for AR, a brief description of AR is followed.

As discussed in section 0, the AR is the process of selecting a unique wind vector out of a set of ambiguous wind vectors at each WVC. The AR is not computed in a WVC by WVC basis but globally. There are two AR techniques, which are commonly used nowadays on scatterometry: the median filter and the variational analysis.

Median filter

The median of a group of data values is that value for which there are equal numbers of data values of greater and lesser magnitude. This convencional definition of the median can only be applied to non-circular (i.e. linear and scalar) data in which the ordering of the values is obvious. For circular data or vector data such as scatterometer winds, an alternative definition of median is used. The median of a set of data x(1), x(2),…,x(N) is defined as the number x(M) which minimizes:

$$\sum_{i=1}^{N} \left| x(M) - x(i) \right| \tag{23}$$

where $1 \leq M \leq N$.

The medians of circular and vector data calculated using the alternative definition have similar characteristics to the median of non-circular data, i.e. extreme and isolated data are ignored.

The median filter is used by JPL for QuikSCAT AR (*JPL, 2001*) and works as follows:

- The wind field over an entire revolution of scatterometer data is initialised with the help of an NWP model. For each particular WVC, the 1st rank or the 2nd rank wind vector solution, whichever is closer to the NWP field, is selected as first guess wind. The number of ranked solutions used for initialisation does not necessarily need to be two (see section 4.2.3).

- The wind vectors in a 7 x 7 filter window determine a median vector for the center WVC. The median vector is compared with the ambiguities in that WVC, and the closest ambiguity to the median is selected for use in the next iteration. The entire revolution is filtered in that way. The process continues until it converges, i.e., when no new replacements of vectors have been made.

The MLE (or probability) information is implicitly used in the median filter. The probability can play an important roll in the selection of ambiguities used in the initialization and filtering processes (this is further discussed in section 4.2.3). However, it is never used explicitly in this AR technique.

Variational analysis

The variational analysis is a commonly used technique for data assimilation into NWP models. It consists of combining the background field (NWP) with the observations, assuming that both sources of information contain errors and these are well characterized, to get an analysis field, which is spatially consistent and meteorologically balanced. This analysis field can then be used for scatterometer AR, that is, to select the closest ambiguous wind solution to the analysis field at each WVC. At KNMI, a simple 2D (at surface level only) variational analysis scheme (2D-Var) has been specifically developed for QuikSCAT AR (*Stoffelen et al.*, 2000), which attempts to minimize the cost function

$$J(\delta x) = J_b + J_o^{scat} ,$$ (24)

where J_b is the background term and J_o^{scat} is the observation term. It uses an incremental formulation with the control variable of wind increments, $\delta x = x - x_b$, defined on a rectangular equidistant grid. The control variable x_b is the background field, which in 2DVAR is an NWP model. The forecast is also used as first guess making the control variable equal to the null-vector at the start of the minimization.

The J_b is a quadratic term that contains the inverse of the background error covariance matrix. It penalizes the deviation from the background field. The J_o^{scat} expresses the misfit between the ambiguous wind vector solutions and the control variable at each observation point. The contribution of the wind solutions in each observation point is weighted by the solution probability.

In order to solve the minimization problem, a conjugate gradients method is used, which also requires the gradient of the cost function. After convergence, the control variable vector of wind increments is added to the background field to obtain the wind analysis. The analyzed wind field is then used for AR, as already discussed.

The solution probability is indeed used explicitly in this AR technique. It plays a very important roll in the minimization and therefore must be characterized in a comprehensive way.

4.2.1 Methodology

Given the assumption of independent Gaussian measurement errors and the application of the Bayes theorem (ssee section 4.1.1), the probability of having the "true' wind given a set of scatterometer observations is related by definition to the MLE in the following way:

$$p(v \mid \sigma^o) = \frac{1}{k} e^{-MLE/2} ,$$ (25)

where v represents the "true" wind and σ^o the set of backscatter measurements, and k is a normalization factor. The theoretical relationship is therefore an exponential. In other words, as the MLE, which represents the misfit of the measurements with the solution lying on the GMF surface, increases, the probability of that particular solution being the "true" wind decreases exponentially. In reality, for several reasons such as the miscalculation of the measurement noise (see section 3.1.1), the shape of the exponential may differ from the theory. In order to perform a comprehensive characterization of the solution probability for QuikSCAT, we apply the procedure described by *Stoffelen et al.* (2000), which works as follows.

- We use the Rn instead of the MLE to avoid the already mentioned problem in the measurement error estimation, such that equation 25 is re-written as:

$$p(v \mid \sigma^o) = \frac{1}{k'} e^{-Rn/l} \tag{26}$$

where k' is again a normalization factor, and l is the parameter that we want to empirically derive. Since we are not using the JPL inversion but the KNMI "tuned" inversion (i.e. NSCAT-2 GMF, no smoothing and 2D interpolation), the <MLE>, used to calculate the Rn (see section 3.1.1), is re-computed (see Appendix C).

- In order to empirically derive equation 26, we can ignore the a priori knowledge on the exponential behavior of the probability, and make the following assumption: There exists a function $p_s(x)$ such that, if we have a set of inversion solutions v_i with normalized residual Rn_i, then the probability that rank j is the one closest to the true wind, denoted by $s=j$, is given by

$$P(s = j \mid Rn_i, i \in \{1, N\}) = \frac{p_s(Rn_j)}{\sum\limits_{i=1}^{N} p_s(Rn_i)} \tag{27}$$

- To determine $p_s(x)$, we concentrate first on only those cases which have exactly two solutions. We process about 2.5 days of QuikSCAT BUFR data and we collocate them with ECMWF winds. The closest solution to the ECMWF wind is used as the "selected" wind. Therefore, we can construct a two-dimensional histogram showing the relative probability of selecting the 1st rank (or the 2nd rank), as a function of Rn_1 and Rn_2. But according to our assumption, by applying equation 27 with $N=2$, we find that the probability of selecting the 1st rank is given by

$$P(s = 1 \mid Rn_1, Rn_2) = \frac{p_s(Rn_1)}{p_s(Rn_1) + p_s(Rn_2)} = \{1 + p_s(Rn_2)/p_s(Rn_1)\}^{-1} \tag{28}$$

- Therefore, by re-arranging equation 28, the two-dimensional histogram gives an estimate of $p_s(Rn_2)/p_s(Rn_1)$ for every combination of Rn_2 and Rn_1. Figure 42a shows such experimentally determined ratios as a function of $Rn_2 - Rn_1$, for several values of Rn_1. Although for $Rn_1 = 2.5$ the ratio is somewhat noisy, it is discernible that the ratio is a fairly constant function of $Rn_2 - Rn_1$. Since Rn_1 is

constant and therefore $p_s(Rn_1)$ is also a constant, this plot is actually showing the shape of $p_s(x)$.

- As we know from equation 26, the shape of $p_s(x)$ is exponential and therefore we just have to fit the exponential to the experimental function of Figure 42a by adjusting the l parameter. Figure 42b shows the best fit to Figure 42a, which is represented by the following function:

$$p_s(x) = e^{-x/1.4} \tag{29}$$

where x is representing the Rn.

- In order to check whether the assumption is correct and the $p_s(x)$ we found can be generalized for any number of solutions and not only for two, we use the probability function to predict how often a certain solution rank corresponds to the "true" solution for a varying number of solutions and varying distributions of Rn_i (remember that we have used only a few constant Rn_1 values to fit the distributions of Figure 42a). Tables 30 and 31 compare the predicted distributions over the different ranks with the "observed" distributions (using the closest to ECMWF) in the sweet and the nadir swaths respectively, for the set of about 2.5 days of collocated QuikSCAT-ECMWF data. As it can be seen, when comparing the left side to the right side of the columns, the correspondance is remarkable. [Note that the right side of the columns of tables 30 and 31 compare well as expected with the columns of tables 23 and 24 respectively, since the only
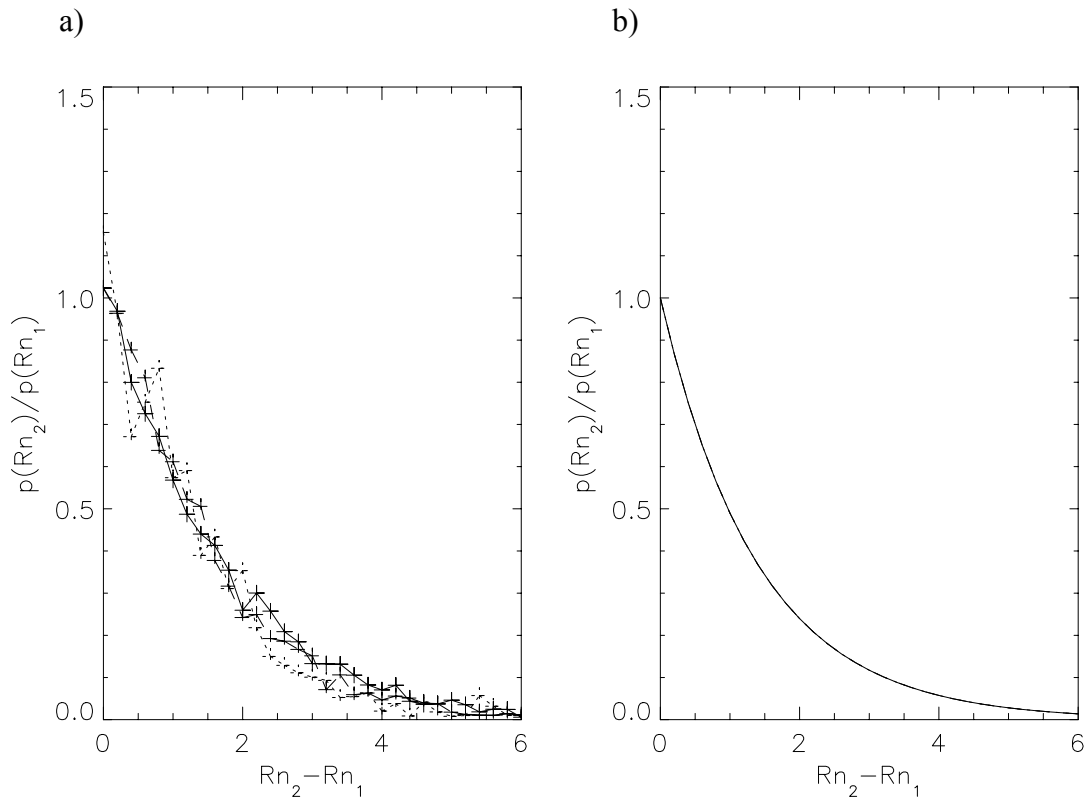
a)   b)

Figure 42 Plot a shows the ratio of the number of realizations of Rn_2 and the number of realizations of Rn1 as a function of $Rn_2 - Rn_1$, and for values of $Rn_1=0.1$ (solid), $Rn_1=1.1$ (dashed), and $Rn_1=2.5$ (dotted). Plot b shows the single exponential fit to the curves of plot a

difference is the data set used, i.e. much larger in the latter tables]. Therefore, we conclude that the assumption is correct and that equation 29 can be used to determine the solution probability.

TABLE 30 Predicted / observed distributions at 25-km (Sweet swath)[1]

	2 Solutions	3 Solutions	4 Solutions	All Solutions
Number of Data	331666	233477	317373	882516
Rank 1	91 / 90	82 / 82	77 / 79	84 / 84
Rank 2	9 / 10	15 / 15	18 / 17	14 / 14
Rank 3	-	3 / 3	4 / 3	2 / 2
Rank 4	-	-	1 / 1	0 / 0

TABLE 31 Predicted / observed distributions at 25-km (Nadir swath)[1]

	2 Solutions	3 Solutions	4 Solutions	All Solutions
Number of Data	262753	172506	45638	480897
Rank 1	82 / 80	79 / 79	65 / 66	79 / 79
Rank 2	18 / 20	17 / 17	20 / 19	18 / 18
Rank 3	-	4 / 4	8 / 8	2 / 2
Rank 4	-	-	7 / 7	1 / 1

[1] Non-smoothing and 2D interpolation have been used in the inversion.

4.2.2 Relevance of spatial resolution

As already mentioned, KNMI has a NRT 100-km resolution QuikSCAT wind product, which includes inversion, QC and ambiguity removal. *Stoffelen et al.* (2000) show that the 25-km QuikSCAT winds are often too noisy, especially at low winds and in the nadir region. They also show that the averaging of the radar backscatter information, and therefore the reduction of the spatial resolution, significantly reduces the noise of the inverted winds. For applications such as mesoscale NWP data assimilation, where the effective resolution of the models is never lower than 100-200 km, the use of reduced resolution QuikSCAT winds is very promising. In this respect, ECMWF is now testing a reduced resolution QuikSCAT wind processing for assimilation purposes. Therefore, a comparison between the 25-km and the 100-km

inversions seems appropriate at this stage, and can in turn help to better understand the QuikSCAT inversion problem.

Probability at 100-km

We can perform this comparison in terms of the probability, since it is a closer stage to AR (see beginning of section 4.2) than the MLE. Therefore, we first compute the probability for the 100-km product, following the same methodology as for the 25-km product (see section 4.2.1):

- The *Rn* at 100-km resolution is computed (see Appendix D).

- The shape of $p_s(x)$ is found by processing about 10 days of QuikSCAT data and shown in Figure 43 for the same values constant values of Rn_1 used for 25-km (see Figure 42a). The curves are noisier than in Figure 42a, since the number of data used in the 100-km two-dimensional histogram is about 4 times smaller than the one used in the 25-km histogram (one 100-km WVC corresponds to sixteen 25-km WVCs). Despite this noise, it is discernible that the curve of Figure 42b fit also fairly well the curves of Figure 43. Therefore, we also use equation 29 to compute the solution probability at 100-km, where *x* is in this case the *Rn* at 100-km resolution.
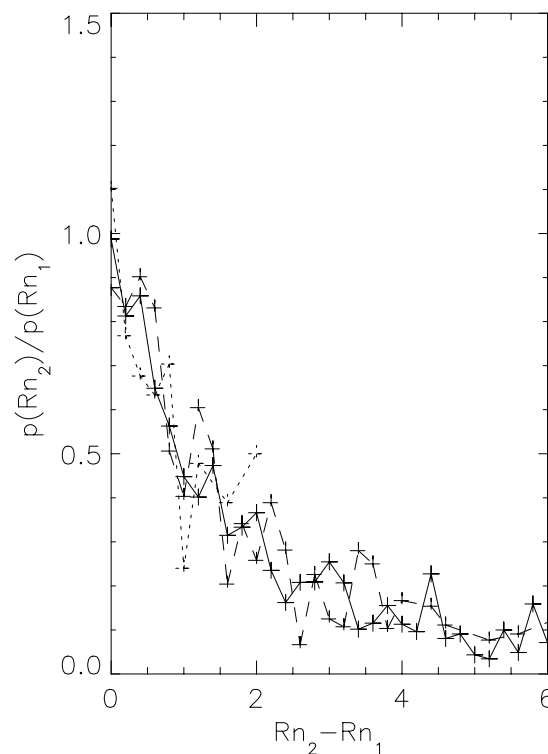

Figure 43 Same as Figure 42a but for the 100-km resolution Rn

- Similar to tables 30 and 31, the results for the verification of the 100-km probability are shown in tables 32 and 33 respectively. The correspondance between the predicted and the observed distributions is also remarkable, confirming the validity of equation 29 for computing 100-km probability.

TABLE 32 Predicted / observed distributions at 100-km (Sweet swath)[1]

	2 Solutions	3 Solutions	4 Solutions	All Solutions
Number of Data	53753	67947	73269	194969
Rank 1	97 / 96	94 / 93	92 / 92	94 / 93
Rank 2	3 / 4	5 / 5	7 / 7	5 / 6
Rank 3	-	1 / 2	1 / 1	1 / 1
Rank 4	-	-	0 / 0	0 / 0

TABLE 33 Predicted / observed distributions at 100-km (Nadir swath)[1]

	2 Solutions	3 Solutions	4 Solutions	All Solutions
Number of Data	66618	40478	9344	116440
Rank 1	83 / 83	93 / 93	78 / 74	86 / 86
Rank 2	17 / 17	6 / 6	16 / 19	13 / 13
Rank 3	-	1 / 1	3 / 4	1 / 1
Rank 4	-	-	3 / 3	0 / 0

[1] Non-smoothing and 2D interpolation have been used in the inversion.

Comparison

Already by comparing tables 30 and 31 to tables 32 and 33 respectively, one can clearly see the significantly higher 1st rank skill of the 100-km product compared to the 25-km product (note the higher percentages of the rank-1 row in the 100-km tables in comparison with the 25-km tables).

In order to compare both products, we have transformed the MLE cost function into a probability cost function by using equation 29. We invert the already mentioned sets of BUFR data (2.5 days for the 25-km and 10 days for the 100-km) and keep the probability cost function information. [Note that disccussing about peaks or maxima in the probability cost function is equivalent to the discussion about minima in the MLE cost function]. Figure 44 shows the statistical results of looking at several characteristics of the cost function.

The top plots of Figure 44 show the histograms of the difference between the maximum (Pmax) and the minimum (Pmin) probabilities for the 25-km (plot a) and the 100-km (plot b) products. The distributions of plot b are much broader and shifted towards higher probability difference values than the distributions of plot a, denoting a better probability modulation and therefore accuracy (see section 4.1.1) of the 100-km product. Comparing the sweet (solid ines) with the nadir (dotted lines), we see a better probability modulation for the former in both products.

The mid plots of Figure 44 show the histograms of the number of cost function points with probability larger than 10% for the 25-km (plot c) and the 100-km (plot d) products. As discussed in section 4.1.1, the cost function is computed at the direction step size of the GMF table (2.5°) and therefore contains 144 points. The fact of having at least one point above 10% probability is an indication of a good probability modulation since it shows how likely these points are with respect to the remaining cost function points with average likelihood of $\frac{1}{144} = 0.7\%$. In this sense, notice the larger amount of times that the 25-km product cost function does not have any probability value above 10% compared to the 100-km product, showing again a better probability modulation of the latter. In a similar way, if we compare the sweet with the nadir swaths, we notice a larger number of times (the double or more) where no cost function points were above 10% probability in the latter. However, the fact of having more or less points above 10% does not necessarily show a better modulation. For example, if we look at the shape of the distributions in plot d, we see that the nadir swath distribution is shifted towards a larger number of points compared to the sweet swath. Since the nadir swath does not usually have more than 3 solutions (look at the number of data with 4 solutions in comparison with the number of data with 2 or 3 solutions in table 33), the relatively large number of points above 10% probability could be an indication of a flat peak, as expected from this region of the swath (see section 4.1.2).

The bottom plots of Figure 44 show the histograms of the difference between Pmax and the mean probability (Pmean) over an interval of ±12.5° around Pmax for the 25-km (plot e) and the 100-km (plot f) products. This difference gives an indication of the peak modulation. The larger the difference, the steeper the maximum (or main peak) of the cost function and therefore the better the acccuracy of retrieved winds is (see sections 4.1.1 and 4.1.2). The larger accumulations of data at low difference values in the nadir swath (dotted) with respect to the sweet (solid) swath confirms the existence of flatter peaks in the former as discussed above. Moreover, this is not only valid for the 100-km product but also for the 25-km product. The reason why we could not infer flat peaks in the 25-km product from the mid plot distributions is that the flat peaks are below the 10% probability level imposed in such plots. However, as we see from the larger accumulation of data at low Pmax-Pmean values in plot e with respect to plot f, the peaks are much flatter (lower peak modulation) at 25-km than at 100-km resolution.

Therefore, we conclude that the 100-km product is less ambiguous and more accurate than the 25-km product and therefore more suitable for wind retrieval purposes than the 25-km product.
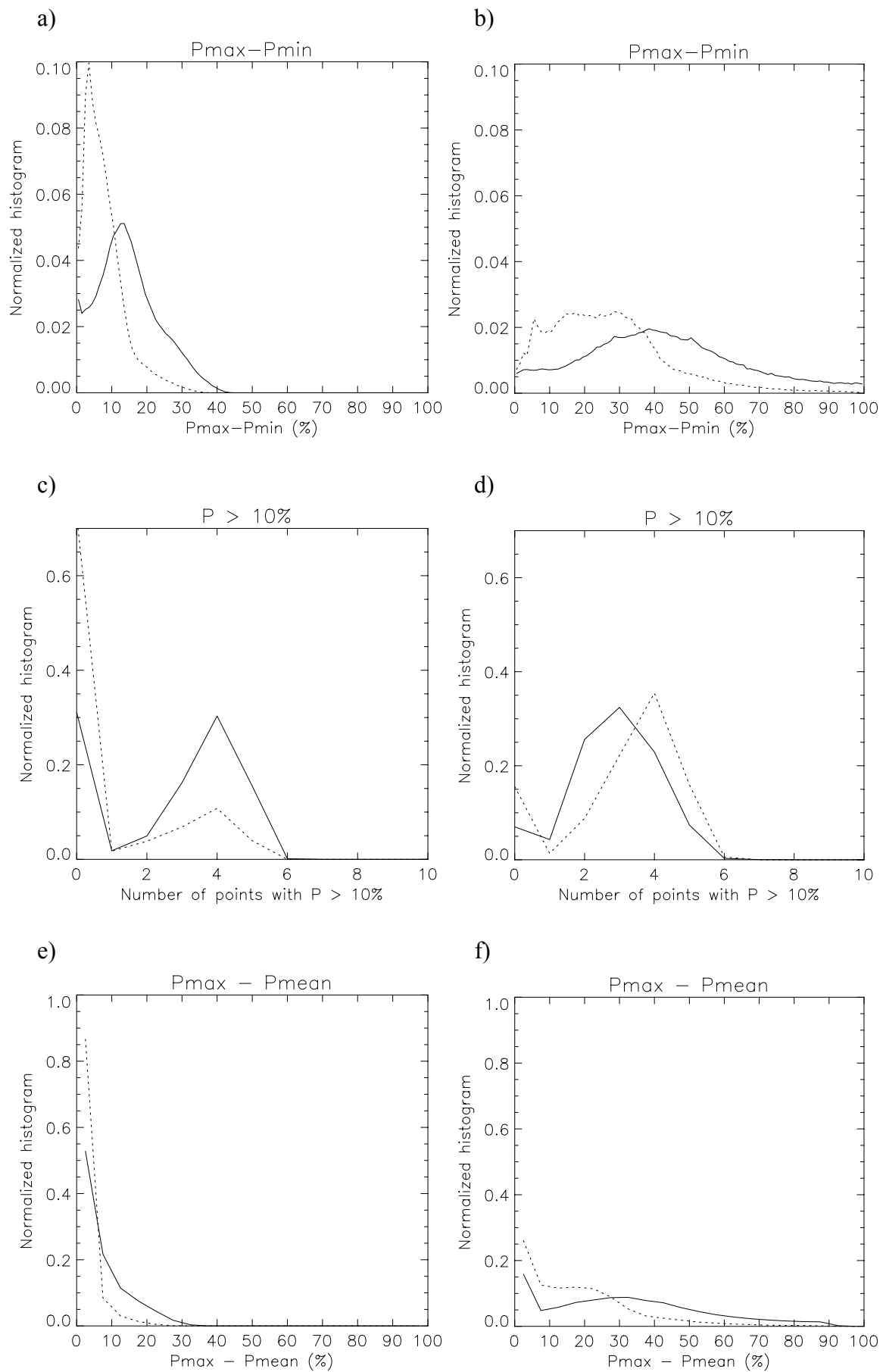
Figure 44 Histograms of the difference between the maximum (Pmax) and the minimum (Pmin) probabilities (top plots), the number of cost function points with probability larger than 10% (mid plots), and the difference between Pmax and the mean probability (Pmean) over an interval of ±12.5° around Pmax (bottom plots), for the sweet (solid lines) and the nadir (dotted lines) regions and for the 25-km (left plots) and the 100-km (right plots) products.

4.2.3 Multiple solution scheme

Up to know, we have extensively examined the inversion problem for QuikSCAT, tuned the inversion in order to reduce its ambiguity and improve its accuracy, and determined the relation between the relative probability of a solution and the MLE in order to prepare QuikSCAT ambiguous solutions for AR. We have learned that in the nadir swath, the accuracy of the inverted winds is low compared to the sweet swath, due to low peak modulation in the probability cost function. For low winds, the accuracy is also low due to the low cost function modulation. The worse scenario is therefore for low winds in the nadir swath, where we get both low peak and cost function modulation.

The number of solutions in the nadir swath is smaller than in the sweet swath (see the relatively small amount of data with 3 and 4 solutions compared with 2 solutions in table 33, in contrast with table 32). This is caused by the shape of the cost function, i.e., a cost function which has well defined and steep probability peaks (or MLE minima), will more likely have a larger number of peaks than a cost function which has broad peaks. However, it seems contradictory to provide less wind solutions to AR when the cost function peaks are less well defined, since for such cases the information content of the wind solutions is poor. Along a broad peak, there are several wind solutions with almost the same relative probability as the peak solution of being the "true" wind by definition (see section 4.1.1). However, by selecting only one (as the inversion is doing), we assign zero probability to the rest of the points which belong to the broad peak. On the other hand, by selecting all of the points of the broad peak, we are transferring to AR a realistic information of the inversion performance; that is, the inversion could not find a clear candidate for that particular region of the cost function, but rather a few candidates with comparable probability.

Precedent

At JPL a multiple solution (not constrained to four solutions) AR called DIRTH (*Stiles et al., 2000*) was developed. It includes an initialization technique for the median filter, called the Thresholded Nudging (TN), and a multiple solution selection scheme as input to the median filter, called the Direction Interval Retrieval (DIR).

The TN allows for more than two ambiguities in the initialization (see beginning of section 4.2) and works as follows. The probability of the cost function is normalized with the probability of rank 1, and the number of ambiguities (up to four) with normalized probability above 0.2 is used in the initialization.

The DIR performs AR in the following way. Given a threshold T (0.8), a set of cost function points around each of the local maxima (resulting in as many segments as local maxima) is selected such that the number of points is minimized and the integral of the cost function over the interval of such points is T. Then AR is performed in the usual manner (except for using the TN for initialization), and only the segment of

points around the selected ambiguity is further used by the median filter (see beginning of section 4.2).

By examining many wind field cases, we conclude that the DIRTH winds are often very smooth and unrealistic in the nadir swath. Here we identify some possible reasons for this result:

- By applying the median filter only on the segment which was selected in the first place by the "traditional" AR, the scheme is subject to the accuracy of the latter. That is, if the traditional AR fails in an area and produces the wrong solutions, all the segments used in that area will in turn produce a more or less smooth field (depending on the width of such segments) but wrong.

- When using a threshold T of 0.8 to define the segments, it may well happen that the remaining cost function points that sum a probability of 0.2 (1-T) contain valuable information indeed. Moreover, if we look at the Pmax - Pmin distributions in the nadir swath for 25-km resolution (Figure 44a), we see a relatively poor probability modulation. In such region, many cost function points with substantial probability may be left out of the segment selection. This will in turn decrease the quality of the wind retrieval.

The reason for setting such threshold T is to prevent oversmoothing. That is, if we use T=1, all data in the cost function will be used by the median filter, which in turn will result in a wind field almost identical to the NWP reference. This is due to a very important limitation of the median filter AR, which is not explicitly using the relative probability of each solution, but rather considering all the solutions with identical probability. However, as already discussed, the resulting wind field is still significantly smooth.

Alternative

The 2D-Var AR (see beginning of section 4.2) explicitly uses the probability of any ambiguous solution. This AR therefore allows the possibility of using as many ambiguous solutions as we desire without the risk of oversmoothing. Moreover, since the variational analysis is always constrained to spatial consistency and meteorological balance, we can ensure realistic retrieved winds by using a multiple solution scheme in combination with such AR.

Figure 45 shows a QuikSCAT retrieved wind field, using the standard inversion output (up to four ambiguous wind solutions) and the 2D-Var AR. In the nadir region, it is clearly discernible that the retrieved wind field is spatially inconsistent. Since the 2D-Var analysis field (not shown) has to be spatially consistent, the problem should lay in the ambiguous solution distribution.

Figure 46a shows the standard ambiguous solution distribution (MLE cost function minima) for the same case of Figure 45. As we can clearly see in the nadir region, the wind solution pattern shows almost no solutions in the direction of the mean flow. Therefore, even if the 2D-Var analysis field is of acceptable quality, there is no way to select a consistent wind field from such solution pattern.

Figure 46b shows the multiple ambiguous solution distribution (not constrained to four) again for the same meteorological case as Figures 45 and 46a. We show all the cost function solutions with probability above 10^{-5}. Notice how often the ambiguous solutions in the sweet swath are around the cost function minimum, which is in the direction of the mean flow, denoting little ambiguity (main cost function minimum much deeper than the remaining minima) in comparison to the nadir swath. It is also clearly discernible that the number of solutions in the nadir region is large, denoting lower accuracy (broader minima), compared to the sweet swath (see ambiguity and accuracy discussion in section 4.1.2). In comparison with Figure 46a, we are providing much more information content to the AR using the multiple solution scheme. As already discussed, the 2D-Var will use the information in an appropriate way (the ambiguous solutions are weighted by their computed probability) and therefore, from a theoretical point of view, the multiple solution scheme should considerably improve the resulting analysis field. Moreover, the AR will now result in a spatially consistent wind field since the multiple solution scheme does provide solutions aligned with the mean flow (see solution distribution in the nadir swath of Figure 46b).
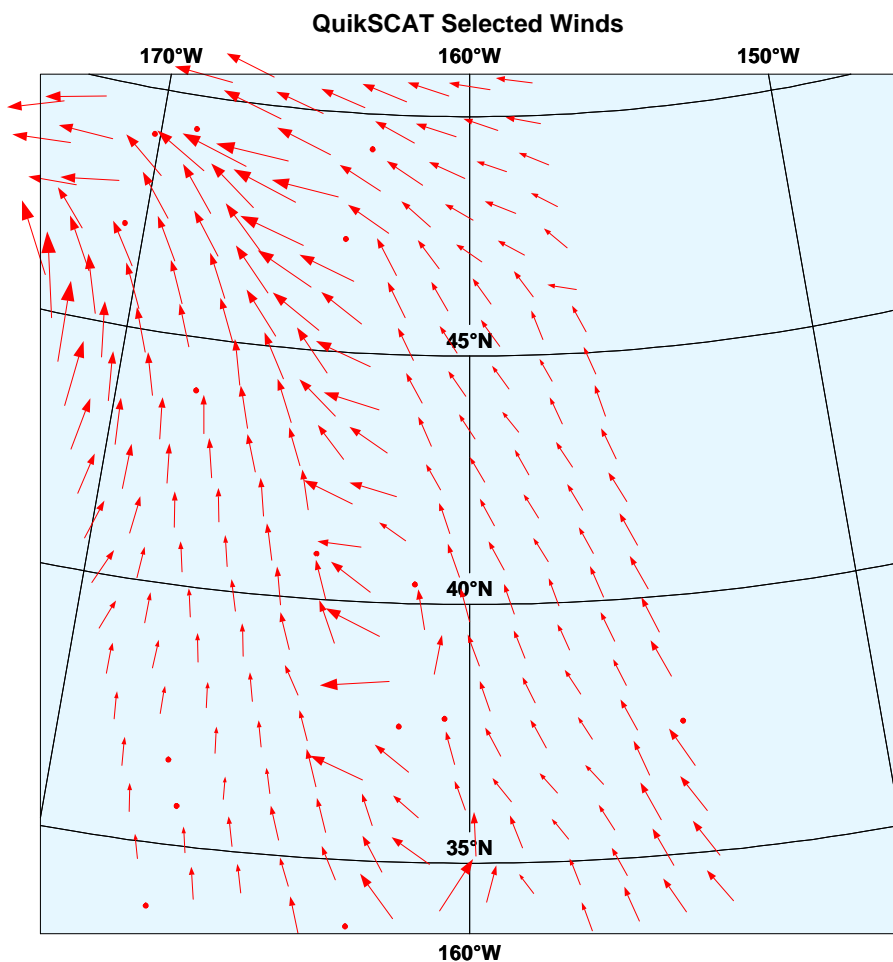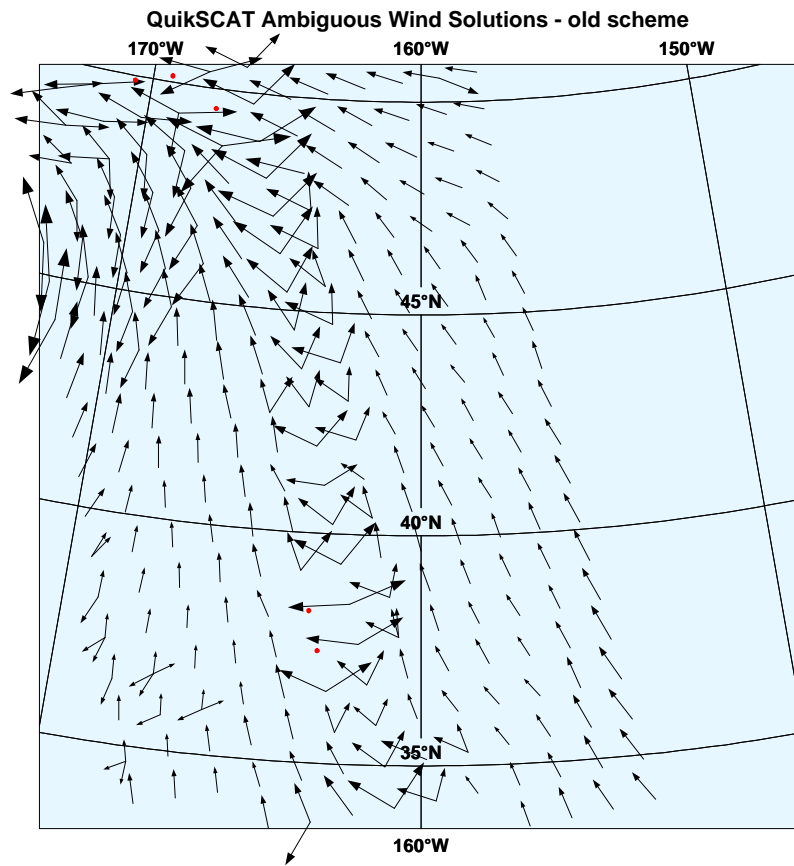

Figure 45 QuikSCAT retrieved wind field using the standard inversion output (cost function minima) and the 2D-Var AR. The acquisition date is January 15 2001 at 16 hours UTC.
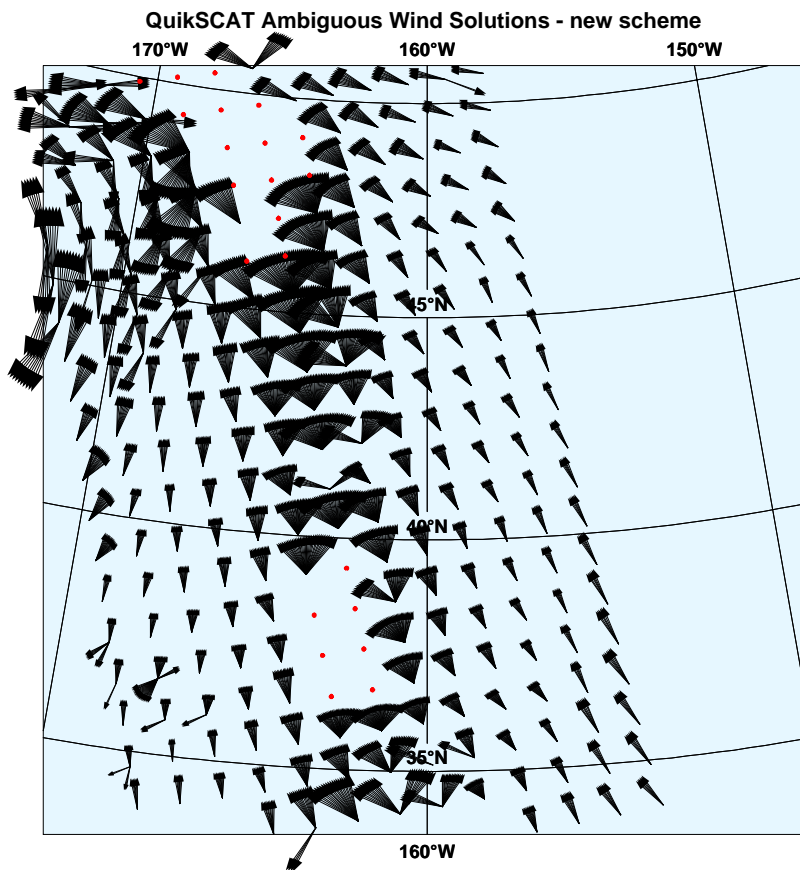
a)

b)

Figure 46 QuikSCAT ambiguous wind field. Plot a shows the standard inversion output (cost function minima); and plot b shows the multiple solution scheme (only solutions with probability above 10⁻⁵).

Therefore, we propose to first test the multiple solution scheme by using all the points of the cost function with non-zero probability (up to 144) as solution ambiguities for the 2D-Var AR. Since this is obviously computationally very expensive, more research needs to be done in order to set a probability threshold that reduces the number of ambiguous without significantly decreasing the quality of the wind retrieval in comparison with the non-zero-probability solution scheme.

Another important aspect of the 100-km product, which needs to be examined, is the QC. Up to now, the 100-km product is using the QC at 25-km resolution, and only if there is sufficient information on the 100-km WVC after QC (at least half of the 25-km WVCs within the 100-km WVC), the wind retrieval is performed. Figure 46b shows the effects of incorporating the JPL rain flag in the 25-km QC (see section 3.4), in comparison with Figure 46a, where only the KNMI QC has been applied. On the one hand, as discussed in section 3.4.4, the JPL rain flag is rejecting a considerable amount of consistent winds, as seen in the Northern part (nadir region) of the wind flow (see WVCs with consistent wind solutions in Figure 46a removed in Figure 46b). On the other hand, the 25-km QC (using JPL rain flag) is able to reject several WVCs, which are of low quality, probably rain contaminated (see the nadir region WVCs with inconsistent solution pattern, both in speed and direction, in the lower half of Figure 46a removed in Figure 46b). These low quality WVCs show zero probability in the direction of the flow (not shown) and therefore it is of great importance to identify these cases and reject them, regardless of the solution scheme we use. However, even if the 25-km QC is able to remove most of the low quality WVCs, a few of them still remain in Figure 46b (notice the absence of solutions aligned with the mean flow in a few nadir WVCs). A way to solve this remaining problem would be to use variational QC, that is, the WVC is rejected if there is no solution close enough (threshold) to the analysis. Another solution would be to set up a QC procedure for 100-km resolution in a similar way as it was done for 25 km (see section 3.1). The 100-km QC would be able to reject the 100-km WVCs that despite they contain good quality 25-km information (after 25-km QC), they result in low-quality 100-km winds, e.g., a 100-km WVC crossed by a front line, which still contains enough quality controlled 25-km WVCs for wind retrieval.

Therefore, more work needs to be done in order to define the best strategy to quality control the 100-km product.

5   Summary and Recommendations

5.1   *Summary*

The KNMI inversion scheme for QuikSCAT, adopted from ERS and NSCAT processing software with help from ECMWF, has been extensively validated and is now being used to produce NRT 100-km QuikSCAT winds. The inversion software turned out to be a very useful tool throughout the fellowship work. It was first used to validate the simulated sample HDF and BUFR products and the real HDF and BUFR QuikSCAT data. Some unwanted features in the data were reported to JPL and corrected by them.

A MLE-based QC procedure, which follows the QC procedure investigated for NSCAT (*Figa and Stoffelen*, 2000) and the QC applied in case of the ERS scatterometer (*Stoffelen*, 1998), was set. In contrast with ERS scatterometer, NSCAT and SeaWinds are sensitive to volumetric rain absorption. As such, QC rejection for ERS is only activated in case of confused sea state, ice occurrence, etc, whereas in the case of QuikSCAT and NSCAT also rain is eliminated.

Collocations of QuikSCAT data with ECMWF winds and SSM/I rain were used to characterize and validate the QC by (Rn) both for HDF and BUFR formats.

The results show a good correlation between the RMS-ECMWF (vector RMS difference between ECMWF and QuikSCAT winds) and the Rn. The data quality, as measured by the inverse of RMS-ECMWF, decreases with increasing Rn, and the decrease rate becomes sharper for increasing retrieved wind speed (data quality becomes poor at medium Rn values when retrieved speeds are higher).

The presence of rain artificially increases the retrieved winds, proportionally to the rain rate. For rain rates over 6 mm/hr, the backscatter measurements contain insufficient wind information but rather rain information, leading to poor quality retrieved winds of typically 15-20 m/s.

We defined a Rn threshold dependent on wind speed, which is optimized to separate the good quality cases from the poor quality ones (including rain) in the inner swath (WVC number 12 to 65). For HDF, the results show a RMS-ECMWF difference between accepted and rejected data of 4 m/s, most of the SSM/I "rainy" cells rejected, and more than 97% of good quality data (low RMS-ECMWF) accepted.

The QC procedure works well in the entire inner swath although the skill in the sweet regions is slightly better than in the nadir region.

The effectiveness of this QC procedure is illustrated with a few typical examples. Cases with meteorologically inconsistent spatial wind patterns are generally removed,

while important information on the dynamical structures is kept. Patterns that are meteorologically consistent are kept in general.

A comparison between HDF and BUFR MLE data shows that both MLE distributions are poorly correlated. However, the consequent different behaviour of the BUFR Rn compared to the HDF Rn is not significantly affecting the skill of the QC procedure, nor the quality of the retrieved winds. Nevertheless, a comprehensive characterization of the MLE is performed in order to fully understand the poor correlation between HDF and BUFR MLE. A very simple example is solved theoretically to show that the different level of averaging of the data in HDF and BUFR can be the main cause. From realistically simulated MLE distributions with different number of measurements (BUFR and HDF), we conclude that the low correlation of the MLE distributions of both formats is due to the σ^o averaging. The simulation results validate the assumptions used to simplify the theoretical case.

Further simulations show how the MLE distributions change as a function of the number of observations taken. The higher the difference in the number of HDF and BUFR observations, the lower the correlation and higher the mean MLE value difference between the two products. The remaining differences between the realistic simulation and the reality are also analysed in detail. Miscalculations of the real measurement noise and simplification in the computation of the number of measurements for both formats in the simulation are pointed out as the main cause for these differences.

A comprehensive comparison of our (KNMI) QC and the JPL rain flag was performed in order to determine an improved QC procedure for QuikSCAT.

Since the JPL rain flag was set at the same time as a new GMF (QSCAT-1) for QuikSCAT wind retrieval, the QC procedure derived for the NSCAT-2 GMF is tested with QSCAT-1. For this purpose, a new set of two weeks of QuikSCAT HDF data is collocated with ECMWF winds and SSM/I rain data. The results show a slight increase of Rn at all speeds, indicating that the NSCAT-2 GMF better fits the observed QuikSCAT backscatter measurements. The larger Rn leads to more rejections in general compared to the NSCAT-2 GMF. This excess in rejections however produces a positive impact in rain detection, especially at rain rates below 6 mm/hr. The same QC procedure (i.e. same <MLE> surface and Rn threshold) can therefore be used with the new QuikSCAT data (produced with the QSCAT-1 GMF).

The JPL rain flag is tested against the KNMI QC. Again, the set of collocations with ECMWF winds and SSM/I rain data is used for this comparison. The KNMI QC detects 4% of low-quality and almost rain-free data, which are not detected by the JPL rain flag. On the other hand, the JPL rain flag detects 2% of low-quality and partially rain-contaminated data, which are not detected by the KNMI QC. The KNMI QC is more effective as QC indicator and the JPL rain flag is more effective as a rain detector.

The KNMI QC is based on the MLE parameter, which turns out to be a very good quality control parameter. The JPL rain flag is based not only on the MLE but also on other parameters, which are identified to be sensitive to rain, such as the brightness temperature, the inter-beam difference, the wind direction and others. However, these

parameters are not related to the quality of the data, which explains why the KNMI QC works better as quality indicator.

The results also show that the JPL rain flag tends to reject many data in rain-free dynamically active areas. We have illustrated this by two different meteorological cases. In both cases, there is an excess of consistent wind rejections by the JPL rain flag, especially in the sweet parts of the swath. In the nadir region, the wind retrieval and consequently the KNMI QC skill is worse than in the sweet regions due to the poor beam azimuth diversity. In this area the JPL rain flag is able to detect some flow-inconsistent and rain-contaminated winds which are not detected by KNMI QC.

For the QC of QuikSCAT data, we recommend the use of the KNMI QC. In the sweet swath, the KNMI QC suffices. However, the combination of the JPL rain flag and the KNMI QC is recommended in the nadir region.

The QuikSCAT inversion problem was extensively examined. It turns out that the wind retrieval skill is much dependent on the region of the swath. In the regions with poor azimuth diversity such as the nadir region or the edges of the outer swath, the accuracy of the retrieved winds is significantly lower compared to the rest of the swath. Since the QC is only reliable in the inner swath (sweet + nadir), we concentrate our efforts in solving the retrieval problems of this region, especially the nadir swath.

The inversion was tuned in order to achieve the least ambiguous and most accurate wind product prior to ambiguity removal. The two available QuikSCAT GMFs, NSCAT-2 and QSCAT-1, are inter-compared, and it turns out that the NSCAT-2 GMF, which was empirically derived from NSCAT measurements, is of similar accuracy but of significantly lower ambiguity. Smoothing of the MLE cost function reduces the ambiguity albeit in an inconsistent way, that is, it significantly decreases the quality of the wind product. However, the interpolation of the GMF table in the speed domain results in a good alternative to smoothing, since it decreases the ambiguity by keeping the accuracy of the wind retrieval.

The MLE cost function is transformed into a probability cost function, by experimentally finding the relation between the MLE and its probability of being the "true" wind. We use the determined probability function to predict how often a certain solution rank corresponds to the "true" solution, using ECMWF winds as reference. The correspondence is remarkable, indicating that the solution probability function we found is correct.

The QuikSCAT 25-km inverted winds are compared to the 100-km winds, using the derived probability cost function. The 100-km product, which is less noisy by definition, turns out to be both less ambiguous and more accurate than the 25-km product.

The results of the extensive study on the QuikSCAT wind retrieval problem show that in order to improve the wind retrieval in areas of the swath such as the nadir region, more ambiguous wind solutions need to be provided to the AR. In order to be successful with the multiple solution scheme, it is very important to characterize each of the ambiguous wind solutions with its corresponding probability of being the "true" wind. Therefore, a median filter AR, in which the probability of each solution is not explicitly used, is not appropriate.

We propose to use a multiple solution scheme in combination with a variational analysis AR such as 2D-Var. The latter is not only capable of correctly assuming multiple solutions (it explicitly uses the probability) but also ensures spatial consistency and meteorological balance of the retrieved winds.

5.2 Recommendations

The MLE-based concept has been successfully used to quality control ERS, NSCAT and QuikSCAT data. Therefore, we recommend the use of this concept for QC purposes in future scatterometer missions, such as SeaWinds on ADEOS-II or ASCAT on METOP.

Further optimisation of the inversion is recommended. In particular, other MLE norms (denominator of equation 1), such as the unity or a Kp dependent on the measured backscatter σ_m^o, could be tested.

The use of the solution probability is essential for QuikSCAT wind retrieval. We recommend the use of the computed solution probability, notably for variational analysis AR, such as the 2D-Var developed at KNMI or 3D-Var/4D-Var used by many Meteorological Services for data assimilation.

The multiple solution scheme in combination with a variational analysis AR that we propose to improve QuikSCAT wind retrieval needs to be validated. Moreover, a scheme, which is able to keep most of the information content coming out of the inversion, and allows the process to be computationally efficient, needs to be defined.

The idea of using variational QC, especially in the outer and nadir regions, needs to be examined. A MLE-based QC procedure at 100-km resolution could also be tested.

Finally, in order to satisfy the needs of meteorologists, the development of a 50-km product is recommended for nowcasting and data assimilation purposes

Acknowledgements

Quality Control and Wind Retrieval for SeaWinds

Acronyms

2D-Var	Two-dimensional Variational Analysis
3D-Var	Three-dimensional Variational Analysis
4D-Var	Four-dimensional Variational Analysis
ADEOS	Advanced Earth Observation Satellite
AER	Atmospheric Environmental Research Inc.
AR	Ambiguity Removal
ASCAT	Advanced Scatterometer
BCRS	Beleidscommissie Remote Sensing
BUFR	Binary Universal Format Representation
DIR	Direction Interval Retrieval
DIRTH	DIR + TN
DMSP	Defense Meteorological Satellite Program
DNMI	Norwegian Meteorological Institute
ECMWF	European Centre for Medium-range Weather Forecasts
ERS	European Remote Sensing Satellite
ESA	European Space Agency
EUMETSAT	European Meteorological Satellite Organization
GMF	Geophysical Model Function
HDF	Hierarchical Data Format
HIRLAM	High Resolution Limited Area Model
H-pol	Horizontal Polarization
JPL	Jet Propulsion Laboratory
KNMI	Royal Netherlands Meteorological Institute
METOP	Meteorological Operational Polar Satellites
MLE	Maximum Likelihood Estimator
<MLE>	Expected MLE
MUDH	Multidimensional Histogram
NASA	National Air and Space Administration (USA)
NCEP	National Centre for Atmospheric Prediction (USA)
NOAA	National Oceanographic and Atmospheric Administration (USA)
NRMS	Normalized RMS in wind direction
NRT	Near Real Time
NSCAT	NASA Scatterometer
NWP	Numerical Weather Prediction
OVWST	Ocean Vector Wind Science Team
QC	Quality Control
RFSCAT	Rotating Fan-beam Scatterometer
RMS	Root-Mean-Squared
RMS-ECMWF	Vector RMS difference between JPL-selected and ECMWF winds
Rn	Normalized Residual
RR	Rain Rate
SAF	Satellite Application Facility
SAG	Science Advisory Group
SSM/I	Special Sensor Microwave Imager

SD	Standard Deviation
SWT	Science Working Team
TN	Thresholded Nudging
UKMO	United Kingdom Meteorological Office
UTC	Universal Time Coordinated
V-pol	Vertical Polarization
WVC	Wind Vector Cell

References

Boukabara, S.A., Hoffman, R.N., and Grassotti, C., "*Atmospheric Compensation and Heavy Rain Detection for SeaWinds Using AMSR*", Atmospheric Environmental Research Inc., 1999.

Figa, J., and Stoffelen, A., "*On the Assimilation of Ku-band Scatterometer Winds for Weather Analysis and Forecasting*", IEEE Trans. on Geoscience and Rem. Sens. 38 (4) pp. 1893-1902, July 2000.

Freilich, M.H., Vanhoff, B.A., Dunbar, R.S., "*Empirical Determination of a Ku-band Wind Model Function from SeaWinds Scanning Scatterometer*," J. Geophys. Res. (in prep.), 2002.

Huddleston, J.N., and Stiles, B.W., "*Multidimensional Histogram (MUDH) Rain Flag*", Product Description Version 2.1, available at http://podaac-www.jpl.nasa.gov/quikscat/, September 2000.

Isaksen, L., and Stoffelen, A., "*ERS Scatterometer Wind Data Impact on ECMWF's Tropical Cyclone Forecasts*" IEEE Trans. on Geoscience and Rem. Sens. 38 (4) pp. 1885-1892, July 2000.

Jones, L., Mladen, S., Park, J., and Mehershadi, R., "*A Quality Control Rain Flag using QuikSCAT Radiometric Observations*", in Proc. of QuikSCAT Cal/Val Workshop, Pasadena/Arcadia (USA), November 1999.

JPL, "*QuikSCAT Science Data Product User's Manual*", version 2.2, JPL D-18053, pp. 89, December 2001.

Leidner, M., Hoffman, R., and Augenbaum, J., "*SeaWinds Scatterometer Real-Time BUFR Geophysical Data Product*", version 2.2.0, NOAA/NESDIS, February 2000.

Mears, C., Wentz, F., and Smith, D., "*SeaWinds on QuikSCAT Normalized Objective Function Rain Flag*", Product Description Version 1.2, available at http://podaac-www.jpl.nasa.gov/quikscat/, September 2000.

Pierson, W.J., "*Probabilities and Statistics for Backscatter Estimates Obtained by a Scatterometer*," J. Geophys. Res., 95, 809, 1990.

Rodgers, C. D., "*Inverse Methods for Atmospheric Sounding: Theory and Practice*," World Scientific Publishing Co., 2000.

Rohn, M., Kelly, G., and Saunders, R., "*Experiments with Atmospheric Motion Vectors at ECMWF*", in Proc. of Fourth International Winds Workshop, EUM P24, ISSN 1023-0416, pp. 139-146, October 1998.

Spencer, M.W., Wu, C., and Long, D.G., *"Tradeoffs in the Design of a Spaceborn Scanning Pencil Beam Scatterometer: Apllication to SeaWinds"* IEEE Trans. Geosci. Remote Sensing, Vol. 35, No. 1, pp. 115-126, January 1997.

Stoffelen, A., *"Scatterometry"*, PhD thesis ISBN 90-393-1708-9, October 1998.

Stoffelen, A., and Anderson D., *"Scatterometer Data Interpretation: Measurement Space and Inversion"*, J. Atm. and Ocean. Techn., 14(6), pp. 1298-1313, 1997.

Stoffelen, A., Van Beukering, P., *"Implementation of Improved ERS Scatterometer Data Processing and its Impact on HIRLAM Short Range Weather Forecasts"*, Report for the Beleidscomissie Remote Sensing, contract NRSP-2/97-06, 1997.

Stoffelen, A., de Vries, J., and Voorrips, A., *"Towards the Real-Time Use of QuikSCAT Winds"*, BCRS Final Report, September 2000.

Van De Hulst, H.C., *"Light Scattering by small particles"*, John Wiley and Sons, New York, pp. 428, 1957.

Wentz, F.J., and Smith, D.K., *"A Model Function for the Ocean Normalized Radar Cross Section at 14 GHz Derived from NSCAT Observations,"* J. Geophys. Res., 104, C5, 11499-11514, 1999.

Wentz, F.J., Smith, D.K., and Mears, C., *"Rain and the QuikSCAT Winds"*, in Proc. of QuikSCAT Cal/Val Workshop, Pasadena/Arcadia (USA), November 1999.

Appendix A: <MLE> surface fit for JPL-retrieved winds in HDF format

In order to fit a 2D function to the filtered mean MLE surface, we first fit a function for the MLE dependence on wind speed at a certain node. Then we assume that the shape of this function is nearly constant over all nodes of the inner swath and we compute the variation of its mean value over the node number domain.

Figure Aa shows the fit of the filtered mean MLE versus wind speed for node number 25 with a Gaussian + 2nd order polynomial function. The dotted line represents the extrapolated values for wind speeds higher than 20 m/s. It is clearly discernible that the fit is very accurate for that particular node.

Figure Ab shows the averaged MLE over all wind speeds and normalized with the speed dependent function (fit on Figure Aa) versus the node number in the inner swath. The fit is a 2nd order polynomial function (node dependent function). The dotted line shows the extrapolation over the outer swath.

The fact that we have found a 2D function which fits reasonably well to the computed mean MLE makes our assumption of considering the shape of the speed dependent function constant over the node domain valid.
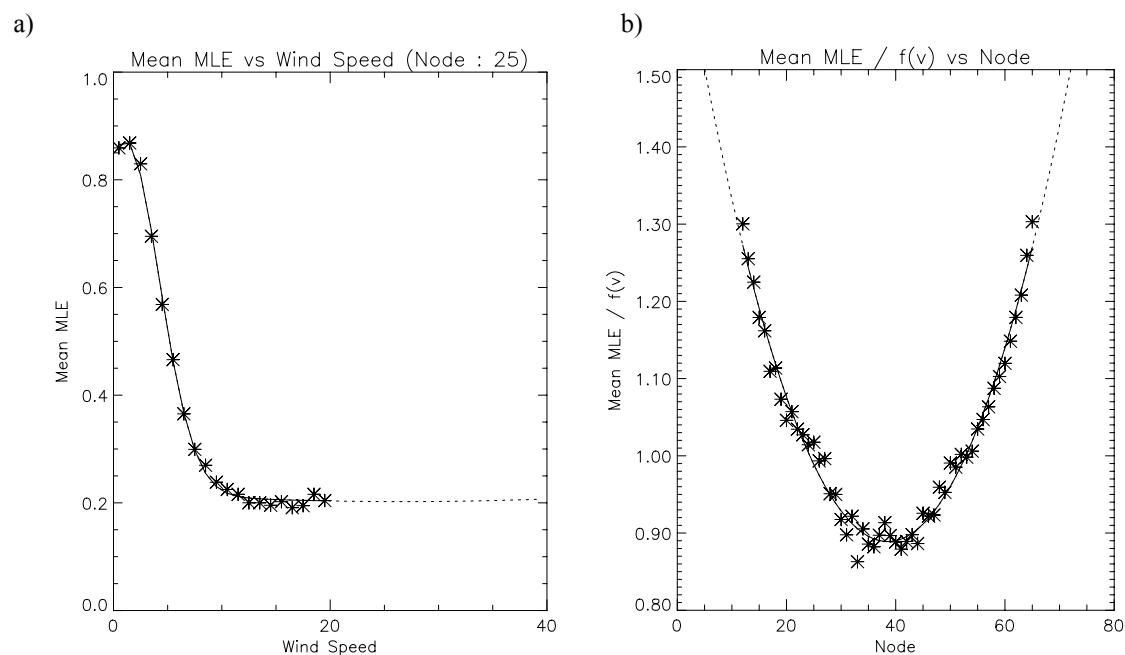
a)

b)

Figure A Filtered mean MLE versus wind speed (plot a) for node number 25 (stars), where the solid line shows the function fit and the dotted line the extrapolation for wind speeds higher than 20 m/s; and averaged MLE over all wind speeds and normalized with the speed dependent function (fit on Figure 18a) versus the node number (plot b) in the inner swath (stars), where the solid line represents the function fit and the dashed line the extrapolation for the outer swath.

The 2D function which fits the filtered mean MLE surface is simply the product of the speed and the node dependent functions. The expression is the following:

$$< MLE >_{fit} = f(v) \cdot f'(n) \tag{A1}$$

$$f(v) = A_0 \cdot e^{-\frac{1}{2} \cdot (\frac{v - A_1}{A_2})^2} + A_3 + A_4 \cdot v + A_5 \cdot v^2 \tag{A2}$$

$$f'(n) = B_0 + B_1 \cdot n + B_2 \cdot n^2 \quad ; \forall n \in [1,76] \tag{A3}$$

where f is the wind speed dependent function, f' is the node dependent function, v is the wind speed and n the node number.

The coefficient values are the following :

$A_0 = 0.78519$; $A_1 = 1.47396$; $A_2 = 2.91577$

$A_3 = 0.31881$; $A_4 = -4.2426\text{E-}3$; $A_5 = 6.9633\text{E-}5$

$B_0 = 1.37840$; $B_1 = -0.02713$; $B_2 = 3.4853\text{E-}4$

Appendix B: <MLE> surface fit for JPL-retrieved winds in BUFR format

Looking at the filtered mean MLE surface (see Figure 19a), it is clearly discernible that assuming a constant shape of the MLE dependence on wind speed over all nodes of the inner swath (as in Appendix A) is not valid anymore.

In this case, we fit a Gaussian + 2nd order polynomial function to the filtered mean MLE for each node of the inner swath separately. Then, we fit a 2nd order polynomial function to the evolution of each coefficient of the previous function with respect to the node number. Therefore, the 2D function which fits the filtered mean MLE surface is the following:

$$< MLE >_{fit} = A_0 \cdot e^{-\frac{1}{2} \cdot (\frac{v - A_1}{A_2})^2} + A_3 + A_4 \cdot v + A_5 \cdot v^2 \tag{B1}$$

$$A_i = A_{i0} + A_{i1} \cdot n + A_{i2} \cdot n^2 \quad ; \; \forall i \in [0,5], \forall n \in [1,76] \tag{B2}$$

where <MLE> is the expected MLE, v is the wind speed and n the node number.

The coefficient values are the following:

$A_{00} = 0.55000; A_{01} = 0.00000; A_{02} = 0.00000$

$A_{10} = 1.50000; A_{11} = 0.00000; A_{12} = 0.00000$

$A_{20} = 2.75000; A_{21} = 0.00000; A_{22} = 0.00000$

$A_{30} = 0.21210; A_{31} = -2.49\text{E-}3; A_{32} = 3.02\text{E-}5$

$A_{40} = -7.41\text{E-}3; A_{41} = 3.13\text{E-}4; A_{42} = -4.08\text{E-}6$

$A_{50} = 1.18\text{E-}4; A_{51} = -4.76\text{E-}6; A_{52} = 6.24\text{E-}8$

Quality Control and Wind Retrieval for SeaWinds

Appendix C: Rn calculation for 25-km KNMI-retrieved winds in BUFR format

Following the methodology described in section 3.1.1, we compute the Rn for our KNMI-inverted winds. In contrast with the Rn computed in chapter 3, we use the 1st rank MLE and wind speed information to compute Rn since we do not have information on the "selected" solution (no KNMI 25-km AR at this stage). However, as discussed in section 3.1.4, the Rn based on the 1st rank solution is comparable to the Rn based on the selected solution in terms of QC skill. Therefore, it is irrelevant whether we use an Rn based on the selected or the 1st rank solution for computing the solution probability.

Figure Ca shows the "filtered" mean KNMI 1st rank MLE as a function of node number and KNMI 1st rank wind speed for QuikSCAT BUFR data, at the inner swath. In contrast with Figures 8b and 19a, there is no straightforward way to fit a two-dimensional function (see Appendices A and B) to this surface. We could directly use this surface as <MLE> by creating a table. However, there is some remaining noise in the surface, especially at low and high winds that we would like to remove. It is also important to remove this noise if we want to consistently extrapolate the <MLE> for winds higher than 20 m/s. Therefore, we have fit a Gaussian + 2nd order polynomial function in the speed domain for every node of the inner swath. Since it is not practical to use 54 different functions (one for every inner swath node) and the mean MLE is rather constant for high winds, we have created a two-dimensional array (table) with speed bins of 1 m/s and node bins of 1, which ranges from nodes 1 to 76 and from speeds 0 m/s to 20 m/s. For any wind speed higher than 20 m/s, the <MLE> value used is the one at 20 m/s for that particular node number. There are not yet plans to use the Rn in the outer swath and therefore no attempt to extrapolate the <MLE> in the outer swath has been made. However, as a first guess, we have copied the <MLE> values at the edges of the inner swath to the outer swath nodes. Figure Cb shows the <MLE> surface derived from the <MLE> array, over the inner swath. The surface compares well with the mean MLE surface (Figure Ca).

For every WVC, the Rn of any solution provided by the inversion is computed (equation 2) by using the corresponding MLE value and the <MLE> value derived from the 1st rank wind speed and the node number information.
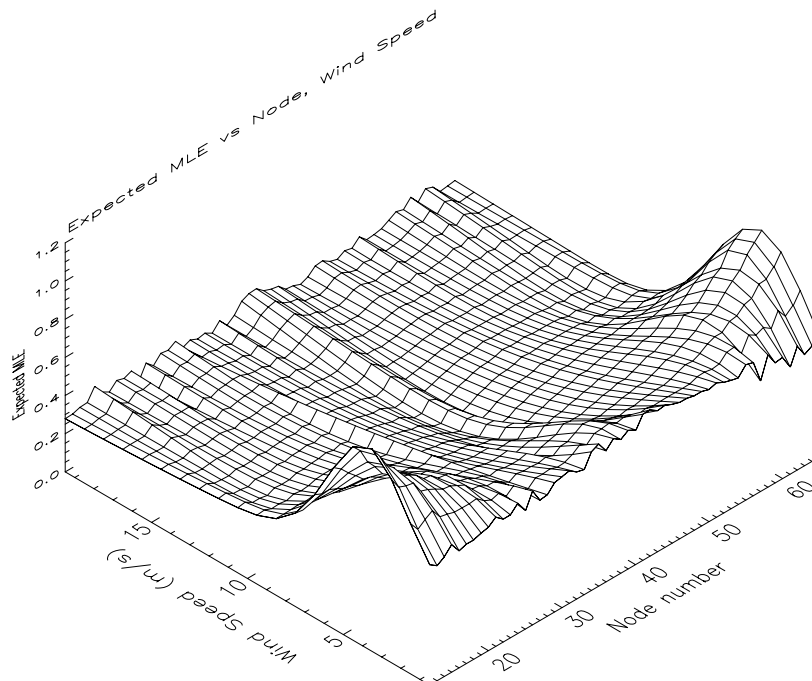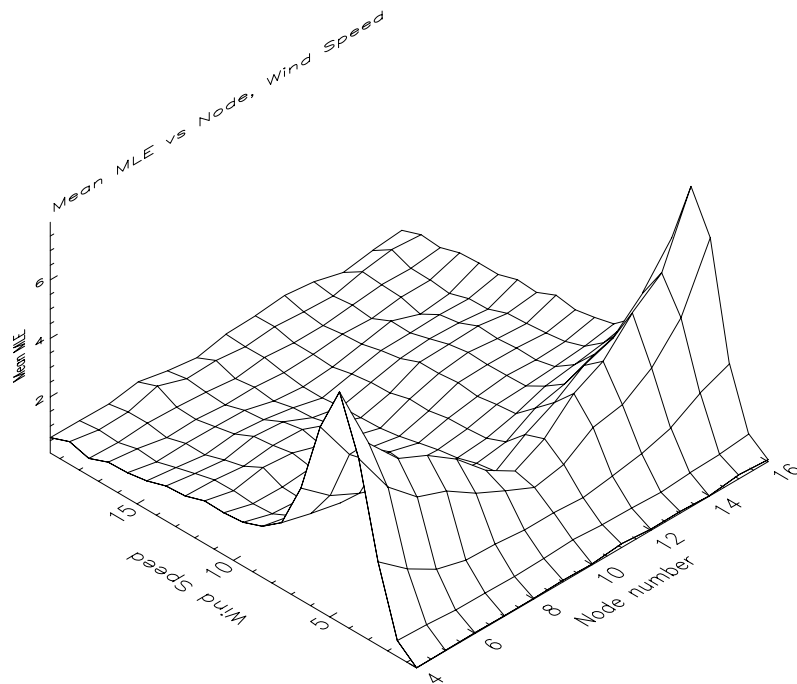
a)
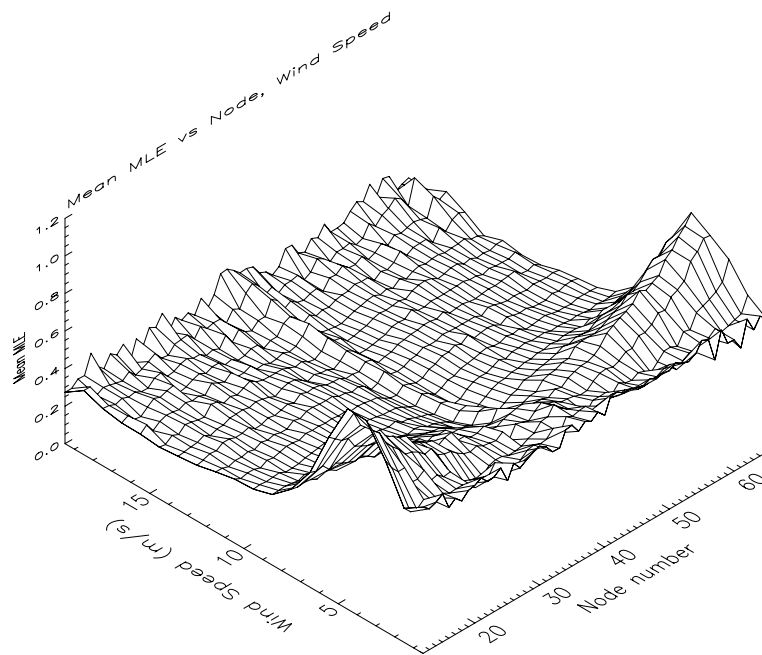
b)

Figure C "Filtered" mean KNMI 1st rank MLE (plot a) and Expected MLE (plot b) as a function of node number and KNMI 1st rank wind speed for BUFR data (inner swath), at 25-km resolution. The speed binning is 1 m/s and the node binning is 1.

Appendix D: Rn calculation for 100-km KNMI-retrieved winds in BUFR format

The Rn for 100-km is computed in a similar way to the Rn for 25-km (see Appendix C).

Figure Da shows the "filtered" mean KNMI 1st rank MLE surface as a function of the KNMI 1st rank wind speed and the node number for 100-km resolution inverted winds. [Note that the 100-km WVC numbers 4 to 16 correspond to the entire QuikSCAT inner swath]. As in Figure Ca, there is no straightforward way to fit a two-dimensional function to the surface. Therefore, we compute a table in a similar way as for the 25-km product <MLE> (see Appendix C). However, as we can see in Figure Da, no significant noise is present in the surface. Therefore, we do not even perform a function fit in the speed domain, as it is done for the 25-km surface (see Appendix C), but rather leave the surface as it is. We only perform an average over the last three speed bins (wind speeds from 17 m/s to 20 m/s) to filter the remaining noise at high winds and therefore be able to consistently extrapolate for winds higher than 20 m/s. Therefore, the <MLE> table (shown in Figure Db) is almost a copy of the mean MLE surface (Figure Da).
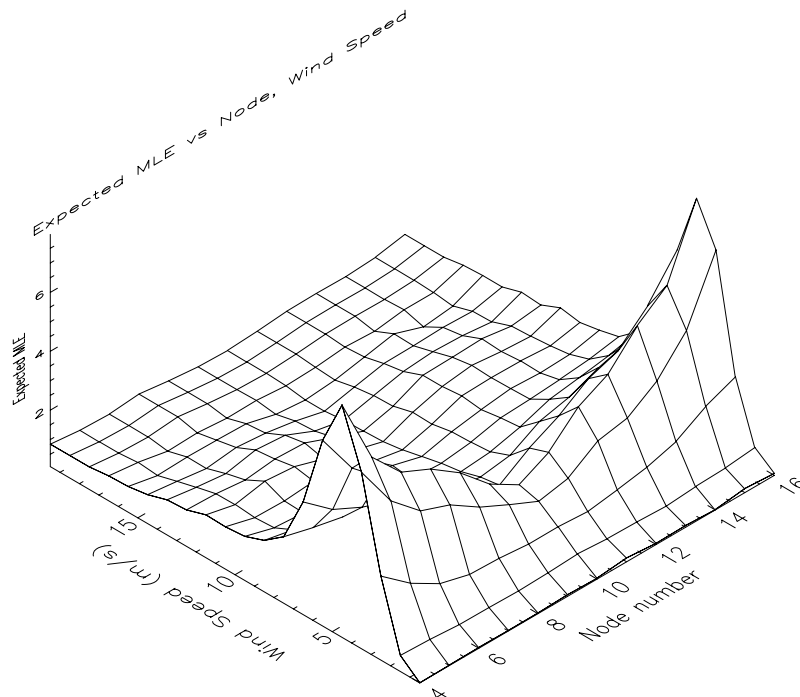
a)

b)

Figure D "Filtered" mean KNMI 1ˢᵗ rank MLE (plot a) and Expected MLE (plot b) as a function of node number and KNMI 1ˢᵗ rank wind speed for BUFR data (inner swath), at 100-km resolution. The speed binning is 1 m/s and the node binning is 1.

Appendix E: Software development

During the fellowship work, several software capabilities have been developed using the KNMI and the ECMWF facilities, including:

- Readers in Fortran 90 for QuikSCAT HDF (Levels 2A and 2B) [bgowm1: ~portabel/marc/hdf/qretrieve25/retrievals_hdf25.f] and BUFR [bgowm1: ~portabel/marc/bufr/qretrieve25/retrievals_bufr25.f] data products, based on the readers originally developed by Kelly Perry (JPL) and Mark Leidner (AER) respectively.

- QuikSCAT inversion in Fortran 77 [bgowm1: ~portabel/marc/common_lib/julia_software/inversion_julia_1.2.f], adapted from the NSCAT inversion software developed by Julia Figa (EUMETSAT). A new inversion software has been developed at KNMI by Jos de Kloe in Fortran 90 [bgowm1: ~portabel/marc/common_lib/jos_software/inversion_1.4.5.f90], which adds the capability of using it for any scatterometer instrument. The new inversion software has been fully validated for QuikSCAT use, and it will be soon incorporated in the NRT 100-km KNMI wind processing.

- QuikSCAT collocations with ECMWF winds and SSM/I rain data in Fortran 77 [scripts: qscat_ecmwf_col_2000, ecmwf_ssmi_col; located at ecgate1: ~nkw/collocations/], adapted from the NSCAT collocation software developed by Julia Figa (EUMETSAT).

- Rn calculation algorithms for JPL HDF [bgowm1: ~portabel/marc/collocations/colloc_qscat_hdf.f] and BUFR winds [bgowm1: ~portabel/marc/collocations/colloc_qscat_bufr.f] in Fortran 90, used for QC in chapter 3.

- Rn and probability calculation routines for KNMI BUFR 25-km and 100-km resolution winds in Fortran 90 [bgowm1: ~portabel/marc/common_lib/inversion_1.4.5_mult_sol_144.f90], used by the multiple solution scheme in chapter 4.

The KNMI NRT 100-km QuikSCAT wind processing, which includes inversion and ambiguity removal, is being adapted in collaboration with John de Vries, to accommodate the multiple solution scheme. The inversion part is already adapted and fully validated. However, additional work needs to be done in the ambiguity removal software. The software will be put available through the NWP SAF in due time.

Appendix F: Related activities

Meetings and Conferences

- SAR Workshop, ESTEC (The Netherlands, April 1999)Presentation: "*SAR Wind Retrievals versus HIRLAM Output : A two way Validation-by-Comparison*"

- QuikSCAT Launch Science Meeting (USA, June 1999)including a meeting at JPL (Pasadena)

- QuikSCAT Cal/Val and Science Meeting (USA, November 1999)
  Presentation: "*Preliminary Results in QuikSCAT Quality Control : Rain Detection*"Ocean Winds Workshop, IFREMER (France, June 2000)
  Presentation and paper in proceedings: "*QuikSCAT Quality Control : Rain Flag*"
  Poster: "*SAR Wind Retrievals versus HIRLAM Output : A two way Validation-by-Comparison*"

- EOS/SPIE Symposium (Spain, September 2000)
  Presentation and paper in proceedings: "*Towards a QuikSCAT Quality Control Indicator : Rain Detection*"
  Presentation: "*Towards high-resolution and time-continuous ocean-surface stress fields*"

- QuikSCAT Fellowship Progress Meeting, EUMETSAT (Germany, September 2000)
  Presentation: "*How to Differentiate SeaWinds from Sea Rain*"

- NASA Oceanography Scientific Conference. Ocean Vector Wind Science Team meeting (USA, April 2001)
  Presentation: "*KNMI Quality Control versus JPL Rain Flag*"
  Poster: "*Characterization of Residual Information for Quality Control*"

- IGARSS Symposium (Australia, July 2001)
  Presentation and paper in proceedings: "*Development of a SeaWinds Wind Product for Weather Forecasting*"

- QuikSCAT Fellowship Final Meeting, EUMETSAT (Germany, Feb. 2002)
  Presentation: "*Winds from SeaWinds*"

Peer reviewed papers

- Portabella, M., and Stoffelen, A., "Rain Detection and Quality Control of SeaWinds," *J. Atm. and Ocean Techn.*, Vol. 18, No. 7, pp. 1171-1183, 2001.

- Portabella, M., and Stoffelen, A., "A Comparison of KNMI Quality Control and JPL Rain Flag for SeaWinds," *Can. Jour. of Rem. Sens.* (special issue on Remote Sensing of Marine Winds), Vol. 28, No. 3, 2002.

- Portabella, M., and Stoffelen, A., "Characterization of Residual Information for SeaWinds Quality Control," submitted to *IEEE TGARSS*, July 2001.

Courses

- Oxford/RAL Spring School in Quantitative Earth Observation (UK, April 2000).

- ECMWF training course in Data Assimilation and use of Satellite Data (UK, May 2001).

Appendix G: Contacts and collaborations with other research groups

In the course of the fellowship, several contacts and collaboration have taken place inside and outside KNMI. The most relevant of them are the following:

- As part of the QuikSCAT Science Working Team (SWT), we have attended the QuikSCAT meetings. In the course of these meetings, KNMI has been invited to join the Ocean Vector Wind Science Team (OVWST). The activities of the OVWST include the SeaWinds on ADEOS-II, planned to be launched in late 2002.

- A close collaboration with ECMWF was set up in order to assimilate QuikSCAT data in the operational suite (since January 22, 2002). In particular, the QuikSCAT QC procedure developed at KNMI is considered for implemention at ECMWF.

- There is an ongoing collaboration with other meteorological centres on QuikSCAT data assimilation matters. In particular, DNMI, UKMO, and NCEP are considering the use of our QC in their QuikSCAT assimilation process and for nowcasting purposes.

- There has been a fruitful collaboration within the KNMI scatterometer group. In particular, we have benefit from the QuikSCAT developments, such as the inversion or the NRT 100-km wind processing, of the following projects: BCRS, NWP-SAF and RFSCAT.

- The fellowship work has been presented by Ad Stoffelen to the ESA/EUMETSAT ASCAT SAG for consideration by experts in the field.